UNIVERSITAT DE BARCELONA

Study of radiative decays at LHCb and search for the Λ0b->pπ-γ decay

Alejandro Alfonso Albero

Tesis doctoral

Study of radiative decays at LHCb and search for the $\Lambda_b^0 \to p\pi^-\gamma$ decay

Autor:

Alejandro Alfonso Albero

Directores:

Dr. Lluís Garrido Beltrán

Dr. Eugeni Graugés Pous

UNIVERSITAT DE BARCELONA

Study of radiative decays at LHCb and search for the $\Lambda_b^0 \to p\pi^-\gamma$ decay

Memoria presentada para optar al grado de doctor por la

Universitat de Barcelona

Programa de doctorado en Física

Autor:
Alejandro Alfonso Albero

Directores:
Dr. Lluís Garrido Beltrán
Dr. Eugeni Graugés Pous

UNIVERSITAT DE BARCELONA

Acknowledgements

I would like to thank Lluís and Eugeni for providing me with the opportunity of working in one of the big experiments of the LHC and being able to travel to CERN. It has been a pleasure and a big accomplishment for me.

To Sandra, who has always been there in the ups and the lows. Our lives have changed a lot during these five years but she has been my biggest support when the thesis seemed insurmountable. I love you.

A mi familia, por su apoyo incondicional a pesar de la distancia y sin olvidarme del duro golpe que ha sido la Covid-19, espero que puedan volver a mirar al futuro con optimismo.

A mis amigos, que sin importar por los diferentes caminos que tomamos siempre que nos vemos es como si el tiempo no pasara.

To all the people I've met in the university, with our rants, our overcrowded lunches and big laughter. What a shame to be separated in the past year, I have greatly missed those times when working from home. To my colleagues to whom I wish their best in their careers. Also, to the board games club, always enlightening my Sunday afternoons while at CERN and making me discovery a new hobby.

And finally, to University of Barcelona, CERN, and the LHCb collaboration for their hard work, guidance and advice. I wish them all well and to keep pushing the limits of our knowledge.

Contents

Resumen

Esta tesis tiene como objetivo el estudio de las desintegraciones radiativas recogidas por el detector LHCb, en concreto del proceso $\Lambda_b^0 \to p\pi^-\gamma$, empleando los datos tomados durante el Run 1 del acelerador LHC, correspondientes a 2011 y 2012. A su vez, también se ha desarrollado la selección de trigger inclusiva que comenzará a emplearse en el Run 3, a partir de 2022. Este tipo de procesos es especialmente sensible a efectos producidos por interacciones o partículas no contempladas en el Modelo Estándar (ME) de la física de partículas, por lo que sirven como comprobación del mismo. Hasta la fecha, los resultados experimentales de la física de partículas han corroborado las predicciones del ME, a pesar de que existen ciertos fenómenos que todavía no es capaz de incorporar, como la asimetría entre materia y antimateria observada en el universo o la materia y energía oscuras. En el plano teórico, el ME no incluye una descripción de la relatividad general como teoría cuántica de campos, mientras sí lo hace para la interacción electromagnética, nuclear fuerte y débil. Es por ello que la medida de este tipo de desintegraciones también sirve como prueba de la validez de los diferentes modelos teóricos desarrollados para explicar varios de estos fenómenos.

Desintegraciones radiativas de hadrones B

En el ME, las desintegraciones radiativas son un tipo de Corrientes Neutras de Cambio de Sabor (CNCS), en las cuales un quark pesado, en este caso un quark b, se desintegra resultando en un quark más ligero y un fotón. Las CNCS son interesantes para su estudio porque el ME no permite que ocurran de manera directa (a nivel árbol), sino a partir de procesos más complejos como son aquellos representados por diagramas con bucles, como por ejemplo el representado en la Figura 1. Esto provoca que la probabilidad con la que ocurren este tipo de procesos sea sensible a nuevas partículas que puedan entrar en el bucle o a interacciones desconocidas que permitan el proceso a nivel árbol. Además de la supresión de las CNCS del ME, el proceso $b \to d\gamma$ estudiado está también más suprimido que el $b \to s\gamma$ en el ME, ya que la probabilidad de saltar una familia de quarks es más probable que saltar dos, debido a la jerarquía presente en los ángulos de mezcla de la matriz de Cabibbo-Kobayashi-Maskawa (CKM), pues el ratio de probabilidades puede aproximarse como el ratio de elementos de la matriz de CKM $\left|\frac{V_{td}}{V_{ts}}\right|^2 = 0.047 \pm 0.003$.

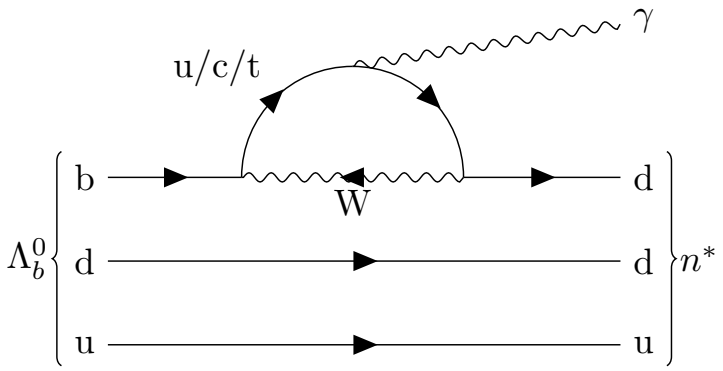

Figura 1: Diagrama de Feynman del proceso $\Lambda_b^0 \to n^*\gamma$.

El LHC y el experimento LHCb

El LHC

El *Large Hadron Collider* (LHC) es el acelerador de partículas circular más grande del mundo, localizado en el Consejo Europeo para la Investigación Nuclear (CERN), en la frontera entre Suiza y Francia. El acelerador ha tenido dos periodos de funcionamiento conocidos como Run 1 y Run 2. El Run 1 corresponde a los años 2011 y 2012, donde se produjeron colisiones protón-protón (pp) con una energía del centro de masas de 7 y 8 TeV, respectivamente. El Run 2 corresponde al periodo entre 2015 y 2018, donde la energía del centro de masas aumentó a los 13 TeV. Además, el acelerador retomará su actividad en 2022 para dar inicio al Run 3, que durará hasta 2024. A lo largo del anillo del acelerador existen 4 puntos de colisión pp, alrededor de los cuales están situados los 4 grandes detectores del LHC:

- ALICE, dedicado a la física de iones pesados. Está diseñado para el estudio de la interacción fuerte de la materia a densidades extremas de energía, en la cual aparece el plasma de quark y gluones.
- ATLAS, un detector de propósito general que investiga desde el bosón de Higgs hasta posibles candidatos de la materia oscura.
- CMS, también un detector de propósito general que investiga desde el bosón de Higgs hasta posibles candidatos de la materia oscura. Aunque tiene el mismo propósito que ATLAS, las técnicas utilizadas y el diseño del sistema de imanes son diferentes.
- LHCb, especializado en la investigación de las pequeñas diferencias entre materia y antimateria a través del estudio de los quarks b y c.

El experimento LHCb

Tanto los datos utilizados como el desarrollo de la selección de trigger pertenecen a las actividades del experimento LHCb. El LHCb está especializado en la investigación de los canales de desintegración del pesado quark b, siendo el estudio de las diferencias entre materia y antimateria la principal motivación. Al contrario que

ATLAS y CMS, el LHCb no rodea el punto de colisión de manera completa, sino que usa una serie de subdetectores colocados unos detrás de otros para detectar las partículas producidas *hacia delante*, en torno al tubo del LHC. Las partículas producidas *hacia atrás* escapan a la detección. El detector LHCb es por tanto un espectrómetro de un solo brazo que permite explotar el hecho de que las parejas $b\bar{b}$ se producen en la misma dirección y muy paralelas a los haces incidentes, cubriendo un ángulo de 15 a 300 mrad en el plano horizontal, y de 15 a 250 mrad en el vertical. La geometría descrita y la localización de los subdetectores se muestra en la Figura 2.

El detector incluye un sistema de detección de trazas de alta precisión que envuelve la región de la colisión pp, un gran detector de tiras de silicio situado delante de un imán dipolar y tres estaciones compuestas de detectores de tiras de silicio y cámaras de hilos, situadas tras el imán. El sistema de detección de trazas consigue una medida del momento de las partículas cargadas con una precisión que varía desde el 0.5% a momento bajo hasta el 1.0% a 200 GeV/c. La distancia mínima de una traza a un vértice primario (VP) y el parámetro de impacto (PI), se miden con una resolución de $(15+29/p_{\mathrm{T}})$ µm, siendo p_{T} la componente del momento perpendicular al haz de protones, en GeV/c. Los información sobre a qué tipo de hadrón cargado pertenece una traza se extrae a partir de dos detectores de luz de Cherenkov. Los fotones, electrones y hadrones se identifican por medio de un sistema de calorímetros, formado por un detector con bloques centelleadores y un detector de pre-cascada, un calorímetro electromagnético y otro hadrónico. Los muones se identifican mediante un sistema compuesto por capas de hierro y cámaras proporcionales de multihilos, colocados de manera alterna. La selección *online* del evento se realiza mediante un trigger, que consiste en una fase de hardware, basada en información de la cámara de muones y los calorímetros, seguida de una fase de software, en la que se reconstruye totalmente el suceso. Esta selección permite reducir los 40 MHz de colisiones proporcionadas por el LHC a menos de 1 MHz.

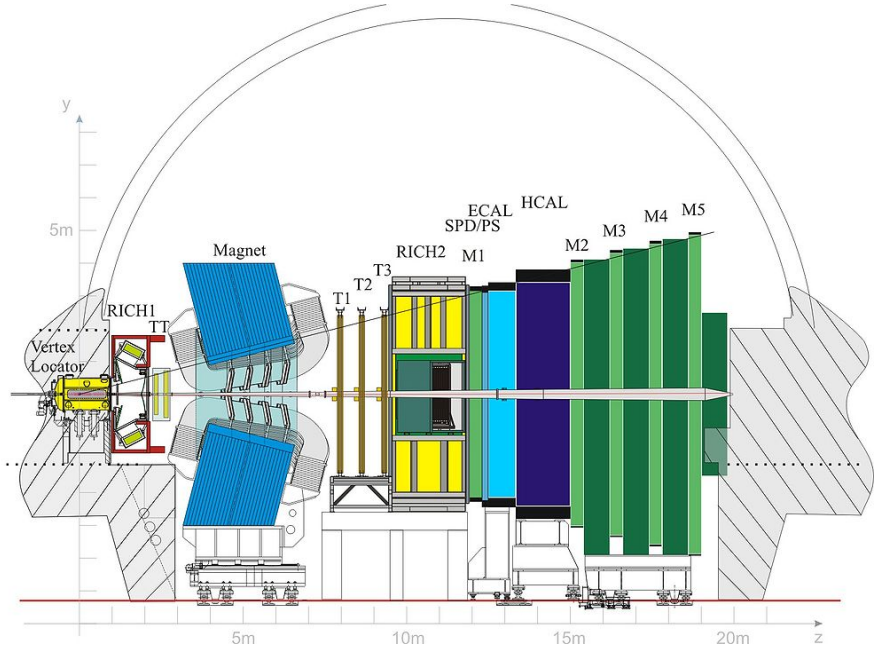

Figura 2: Vista lateral del detector LHCb.

El trigger radiativo inclusivo para el Run 3

Dada la importancia de las desintegraciones radiativas para poner a prueba el ME, para el Run 2 fue desarrollada una selección dedicada a las mismas en LHCb. Esta selección tiene como objetivo mejorar la eficiencia a la cual se buscan eventos que contienen un fotón de alta energía, que es una de las características principales de este tipo de procesos.

Durante el Run 1, para seleccionar desintegraciones radiativas se tenía que emplear el denominado trigger topológico, encargado de buscar eventos con una desintegración a dos o tres hadrones cargados, pero que no aprovecha la información procedente del fotón. Con la implementación de estas líneas de trigger se pudo relajar la selección de dos o tres hadrones, pues se añadió la condición adicional de que debía haber un fotón de alta energía en el evento. El objetivo para el Run 3 es mantener la selección radiativa inclusiva utilizada en el Run 2, adaptándose a las nuevas condiciones experimentales.

Selección

La selección de trigger radiativa inclusiva incluye cuatro líneas (Tabla 1), que se dividen en la búsqueda de desintegraciones con dos o tres hadrones cargados más un fotón y en si el fotón es directo o ha sufrido una conversión en una pareja electrón-positrón al interactuar con el material del detector. En cualquier caso, todas las líneas siguen los mismos pasos de reconstrucción. Primero, dos o tres hadrones se reconstruyen con una selección poco estricta. Este sistema se combina entonces con un fotón de alta energía para formar el hadrón-b preliminar. Finalmente, se aplica una selección multivariable a estos candidatos mediante un *Boosted Decision Tree*

Tabla 1: Lista de líneas de trigger inclusivas radiativas en el Run 3.

Nombre	Esquema de desintegración
`Hlt2BToHHGamma_Inclusive_Line`	$B^0 \to (h^+h^-)\gamma$
`Hlt2BToHHGammaEE_Inclusive_Line`	$B^0 \to (h^+h^-)\gamma$
`Hlt2BToHHHGamma_Inclusive_Line`	$B^+ \to (h^+h^-h^+)(\gamma \to e^+e^-)$
`Hlt2BToHHHGammaEE_Inclusive_Line`	$B^+ \to (h^+h^-h^+)(\gamma \to e^+e^-)$

(BDT).

En concreto, se han empleado cuatro BDTs, uno por cada línea de trigger, con el fin de extraer el mayor número de desintegraciones radiativas como sea posible. Estos BDTs han sido entrenados usando unas muestras simuladas de señal y de sesgo mínimo, que reproducen ciertas desintegraciones radiativas y los eventos típicos que se producen en LHCb, respectivamente. El desglose de las muestras de señal utilizadas en el entrenamiento del BDT se muestra en la Tabla 2.

Sin embargo, el objetivo de este trigger no es únicamente seleccionar desintegraciones radiativas con dos o tres cuerpos, sino también incluir eventos con un mayor número de partículas. Para ello, en la selección se evita utilizar la masa invariante del sistema, mientras que sí se usa la masa corregida, definida como:

$$m_{corr} = \sqrt{m^2 + |p_{\mathrm{T}miss}|^2} + |p_{\mathrm{T}miss}| \tag{1}$$

Donde m es la masa invariante reconstruida del candidato y $|p_{\mathrm{T}miss}|$ es el componente del momento reconstruido perpendicular a la dirección de vuelo de la partícula madre, en este caso, el candidato a hadrón-b. Esta variable está diseñada para recuperar tanto como sea posible el momento de las partículas perdidas en desintegraciones parcialmente reconstruidas.

Finalmente, hay que tener en cuenta que en el futuro funcionamiento del trigger en el Run 3, sólo las partículas incluidas en el esquema de desintegración son guardadas, mientras que el resto del evento no. Esto supone un problema ya que por defecto, usando un esquema de desintegración de tres cuerpos y un fotón, sería imposible guardar toda la información relacionada con una desintegraciones que incluya cuatro o más cuerpos. Para poder hacerlo, estas líneas de trigger guardan una serie de partículas extra ($h^\pm$, Λ, π^0, γ) que puedan ser buenas candidatas para formar parte de una desintegración radiativa, pero evitando guardar el evento completo para optimizar recursos como el ancho de banda, la información guardada en disco, etc.

Rendimiento esperado

Aquí damos a conocer el rendimiento esperado de las líneas de trigger radiativas inclusivas, que todavía puede estar sujeto a cambios hasta que comience el periodo de toma de datos en 2022.

Tabla 2: Muestras de señal simulada utilizadas para optimizar el trigger radiativo inclusivo en el Run 3.

Selección de 2 cuerpos	Selección de 3 cuerpos
$B^+ \to (K^{*+} \to K^+\pi^+\pi^-)\gamma$	$B^+ \to (K^{*+} \to K^+\pi^+\pi^-)\gamma$
$B_s^0 \to (\phi \to K^+K^-)\gamma$	
$B^0 \to (K^{*0} \to K^+\pi^-)\gamma$	

Primero, se tomaron los clasificadores usados en el Run 2 y se aplicaron a las muestras simuladas de Run 3, para comparar su rendimiento frente a los nuevos clasificadores, entrenados y optimizados con las muestras de Run 3. En la Figura 3 puede verse la frecuencia a la cual cada línea de trigger acepta un evento frente a la eficiencia de señal, que está compuesta de la mezcla presentada en Tabla 2. Para todas las líneas puede apreciarse en la Figura 3 un mejor rendimiento de los nuevos BDTs, que aportan una mejor eficiencia de señal dada una misma frecuencia de aceptación. El valor de corte de los BDTs viene dado por límite de frecuencia de aceptación, que se estima en torno a 0.1 kHz para cada línea.

Por otro lado, es necesario estudiar el tamaño medio de un evento, en kbytes, para determinar el ancho de banda necesario para cada línea. Este ancho de banda es de unos 5 kbytes cuando únicamente se guardan las partículas del esquema de desintegración. Sin embargo, hay que tener en cuenta el espacio necesario para guardar las partículas extra para mantener el ancho de banda a un nivel estable. Para ello, hemos aplicado unos cortes suaves en el p_{T} y $\chi^2_{\mathrm{IP_{PV}}}$ de las mismas, usando la muestra de $B^0 \to K^{*0}\gamma$ como referencia, la cual tiene una frecuencia de aceptación mucho mayor y por tanto es mucho más rápida de estudiar.

El resultado de estos cortes puede verse en la Tabla 3, lo cual provoca que el tamaño medio del evento llegue hasta los 15 kbytes. Estas partículas extra, sin embargo, pertenecen a partículas de fondo que han sido generadas en la muestra de señal, es decir, que no pertenecen a ninguna desintegración radiativa. Por tanto, es necesario realizar una selección más precisa mediante el estudio de otras desintegraciones radiativas que sí contengan un K^0_{S}, Λ ó π^0, de manera que pueda reducirse el tamaño medio del evento al tiempo que no se desechan eventos interesantes. Este estudio requiere de la producción de nuevas muestras de señal, y por tanto queda fuera del marco de esta tesis.

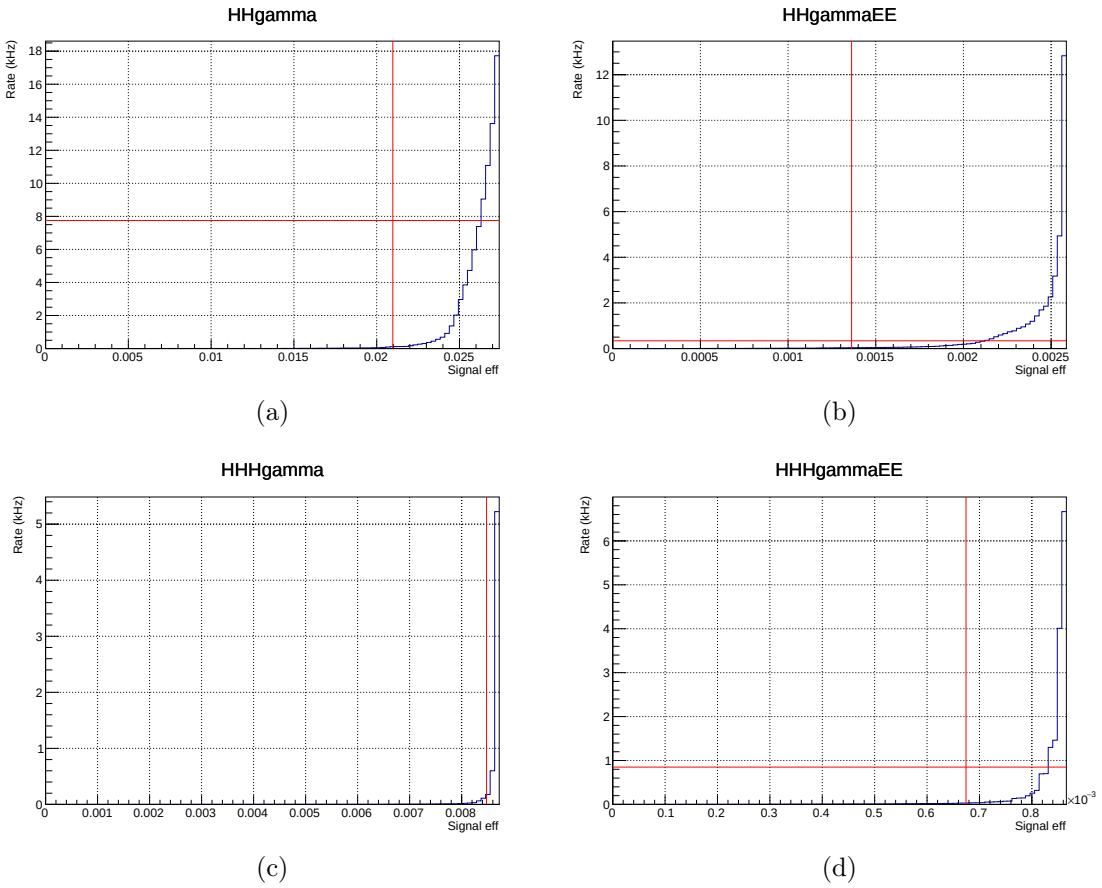

(a) (b) (c) (d)

Figura 3: Frecuencia de aceptación del fondo en función de la eficiencia en señal para los nuevos BDTs, entrenados con simulación de Run 3 (azul) y para cada línea inclusiva radiativa: `HHGamma` 3a, `HHGammaEE` 3b, `HHHGamma` 3c y `HHHGammaEE` 3d. La larga cruz roja indica el rendimiento del BDT entrenado con datos de Run 2 sobre las mismas muestras de Run 3.

Tabla 3: Multiplicidad (número de partículas guardadas por evento seleccionado por la línea `HHGamma`) para cada tipo de partícula extra, dado un corte preliminar en p_{T} y $\chi^2_{\mathrm{IP_{PV}}}$ y estudiado en eventos simulados de $B^0 \to K^{*0}\gamma$.

Partícula	Corte	Multiplicidad
$h^{\pm}$	$p_{\mathrm{T}} > 800\,\mathrm{MeV}$ & $\chi^2_{\mathrm{IP_{PV}}} > 8$	5.0
K^0_{S}	$p_{\mathrm{T}} > 500\,\mathrm{MeV}$	0.7
Λ	$p_{\mathrm{T}} > 500\,\mathrm{MeV}$	0.3
γ	$p_{\mathrm{T}} > 1400\,\mathrm{MeV}$	2.5
π^0 fusionado	$p_{\mathrm{T}} > 2000\,\mathrm{MeV}$	0.8
π^0 resuelto	$p_{\mathrm{T}} > 1600\,\mathrm{MeV}$	3

Búsqueda de la desintegración $\Lambda_b^0 \to p\pi^-\gamma$ en el LHCb

El proceso $\Lambda_b^0 \to p\pi^-\gamma$ (se supone simetría de carga-paridad (CP) a lo largo del texto) es una CNCS que a nivel de quarks puede escribirse como $b \to d\gamma$, lo que lo hace sensible a posibles efectos de nueva física. Este modo de desintegración está más suprimido que el proceso $\Lambda_b^0 \to pK^-\gamma$, correspondiente a una transición $b \to s\gamma$, el cual se utiliza como canal de normalización debido a que comparte con el estudiado tanto la partícula inicial como sus propiedades cinemáticas. Además, las desintegraciones de bariones b no han sido estudiadas con la misma profundidad que las de los mesones B como B^0 ó B_s^0, ya que el número de Λ_b^0 generados en la colisión pp es menor. Por último, la búsqueda del proceso $\Lambda_b^0 \to p\pi^-\gamma$ tiene otro desafío al no considerar ninguna resonancia del sistema $p\pi^-$ en particular, como sí ocurre en los estudios de $B^0 \to K^{*0}\gamma$ ó $\Lambda_b^0 \to \Lambda\gamma$, lo que supone una herramienta menos en la búsqueda de parejas de hadrones de interés para el trabajo.

Reconstrucción y selección de eventos

Los datos empleados en la búsqueda del proceso $\Lambda_b^0 \to p\pi^-\gamma$ corresponden a los tomados por el LHCb en el Run 1, donde la colisión pp se realizó a 7 y 8 TeV durante 2011 y 2012, respectivamente. Para reconstruir el Λ_b^0 inicial se buscan parejas de hadrones con cargas opuestas combinando la información de los calorímetros, de las estaciones de detección de trazas y del localizador de vértices (VELO). Las parejas seleccionadas son combinadas con un fotón, del cual sólo se conoce su energía a través de su interacción con los calorímetros, por lo que se asume que el fotón proviene del punto de la colisión pp. Esta aproximación es válida para este análisis ya que tanto el Λ_b^0 como las posibles resonancias intermedias del sistema de dos hadrones, n^*, tienen tiempos de vida medios muy pequeños. Sin embargo, la resolución del Λ_b^0 empeora en comparación con otros estudios donde se busca una pareja de muones en lugar de un fotón, convirtiéndose en un desafío separar la desintegración de interés de otras desintegraciones radiativas más frecuentes, como $B^0 \to K^{*0}\gamma$.

La selección de candidatos se divide en cuatro grandes partes. Primero se realiza una selección suave utilizando propiedades cinemáticas y topológicas de la desintegración. Tras ello, se entrena un BDT utilizando simulación de Monte Carlo (MC) de $\Lambda_b^0 \to p\pi^-\gamma$ que permite extraer en más profundidad los eventos de interés, explotando más eficientemente la topología y cinemática de la desintegración. Tras esta selección, más enfocada a separar fondo de combinaciones aleatorias de señal, se aplican vetos a diferentes regiones de masa para suprimir la contribución de otras desintegraciones radiativas, como $B^0 \to K^{*0}\gamma$ ó $B_s^0 \to \phi\gamma$. Finalmente, se utiliza la información de los detectores de luz de Cherenkov para seleccionar aquellas parejas de hadrones más probables de ser un protón y un pión, frente a cualquier otra combinación, de nuevo con el objetivo de seguir reduciendo la contaminación de las desintegraciones radiativas más frecuentes.

Extracción del cociente de fracciones de desintegración

Con el objetivo de reducir los errores sistemáticos, la selección utilizada para la señal y la normalización sólo difiere en el criterio de identificación de las partículas cargadas (PID). Así pues, el cociente de fracciones de desintegración puede escribirse como:

$$\frac{\mathcal{B}(\Lambda_b^0 \to p\pi^-\gamma)}{\mathcal{B}(\Lambda_b^0 \to pK^-\gamma)} = \frac{N_{p\pi^-\gamma}}{N_{pK^-\gamma}} \frac{\epsilon_{pK^-\gamma}}{\epsilon_{p\pi^-\gamma}} \tag{2}$$

Donde $\epsilon_{p\pi^-\gamma}$ ($\epsilon_{pK^-\gamma}$) es la eficiencia en la selección de señal (normalización), extraída de la simulación de MC o de la muestra de calibración correspondiente y $N_{p\pi^-\gamma}$ ($N_{pK^-\gamma}$) es el número de eventos de señal (normalización) encontrados por medio de un ajuste a los datos seleccionados. Para el cociente de eficiencias el valor obtenido es:

$$\frac{\epsilon_{pK^-\gamma}}{\epsilon_{p\pi^-\gamma}} = 0.74 \pm 0.05 \tag{3}$$

El ajuste a los datos se realiza mediante un ajuste simultáneo a tres canales de desintegración: señal ($\Lambda_b^0 \to p\pi^-\gamma$), normalización ($\Lambda_b^0 \to pK^-\gamma$) y $B^0 \to K^+\pi^-\gamma$, que permite tener un mayor control de las contaminaciones cruzadas que existen entre ellos. De manera similar a la normalización, la selección para $B^0 \to K^+\pi^-\gamma$ sólo difiere de la de señal en el criterio de PID. Las distribuciones empleadas para describir estas contribuciones, en cualquiera de las tres selecciones, tienen en común la presencia de un núcleo central tipo gaussiano, donde una o ambas colas son sustituidas por funciones exponenciales o leyes potenciales (Crystal-Ball), de acuerdo a la forma que mejor describa la correspondiente muestra de MC. Además de estas contribuciones, las muestras filtradas todavía contienen una parte importante de combinaciones aleatorias de partículas y, en el caso de la selección de $B^0 \to K^+\pi^-\gamma$, reconstrucciones parciales de otras desintegraciones radiativas, como $B^+ \to K_1^+(1270)\gamma$ ó $B^+ \to \overline{D}^0\rho^+$, que afectan a la parte de baja masa. Finalmente, el ajuste simultáneo también incluye los reflejos de $B^0 \to K^{*0}\gamma$ y $\Lambda_b^0 \to pK^-\gamma$, en los que se tiene en cuenta la contribución debida a intercambiar las hipótesis de masa de los hadrones.

El resultado del ajuste se muestra en la Figura 4 y muestra una contaminación no despreciable de eventos $\Lambda_b^0 \to pK^-\gamma$ y $B^0 \to K^+\pi^-\gamma$ en la zona de señal. A pesar de ello, el ajuste revela una pequeña contribución de señal de 30 ± 9 eventos, junto a 407 ± 24 eventos de normalización. Estos resultados, combinados con el cociente de eficiencias descrito anteriormente, dan lugar a un cociente de fracciones de desintegración de $(5.5 \pm 1.7)\%$. , lo que supone la primera evidencia del proceso $\Lambda_b^0 \to p\pi^-\gamma$, a falta por determinar el valor de $\mathcal{B}(\Lambda_b^0 \to pK^-\gamma)$ para obtener una medida absoluta.

Errores sistemáticos

Además del error estadístico obtenido del ajuste, se han tenido en cuenta diferentes fuentes de error sistemático, como son las diferencias entre la simulación y los datos o el efecto de tener una muestra finita de simulación para evaluar las eficiencias. De las discrepancias entre simulación y datos una de las más importantes es la incerteza

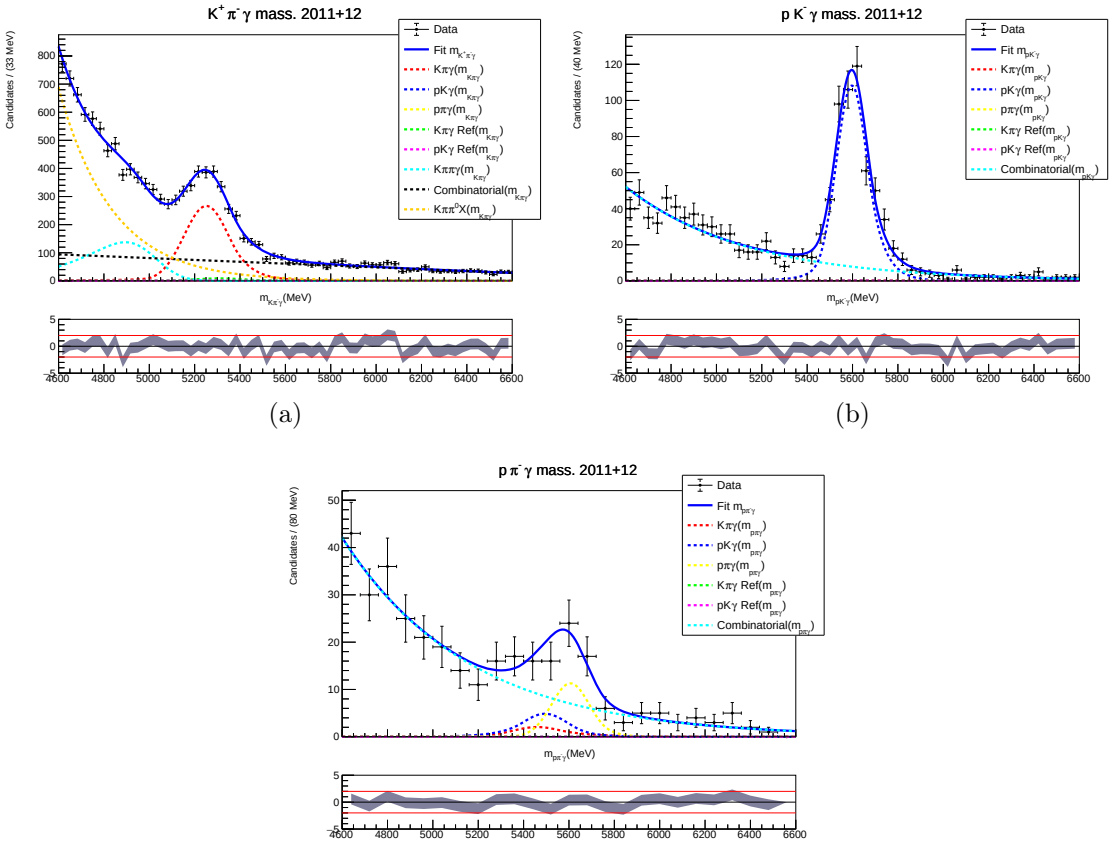

Figura 4: Resultado del ajuste simultáneo a la masa invariante de $K^+\pi^-\gamma$ (4a), $pK^-\gamma$ (4b) y $p\pi^-\gamma$ (4c), usando datos tomados durante el Run 1 en el LHCb.

en la posición de los picos de contaminación en la zona de señal, que representa un error relativo del 3.0%. Sin embargo, la fuente de error más importante proviene de algo más simple como es la limitación de muestra finita de la simulación, con una contribución del 6.4%. En total, el error sistemático contribuye en un 7.9% del resultado final.

Resultados

El error estadístico, del 31%, es el que claramente domina el estudio, frente al 7.9% de error sistemático. Combinando ambas fuentes de error, el resultado final es:

$$\frac{\mathcal{B}(\Lambda_b^0 \to p\pi^-\gamma)}{\mathcal{B}(\Lambda_b^0 \to pK^-\gamma)} = [5.5 \pm 1.7 \pm 0.4]\,\% \tag{4}$$

Lo que supone una desviación de 3σ de la hipótesis nula y la primera observación del proceso $\Lambda_b^0 \to p\pi^-\gamma$. Este resultado, además, es compatible con el valor predicho por el ME a través de la matriz de CKM: $[4.7 \pm 0.3]\%$.

Conclusiones

El trabajo de esta tesis se encuentra en el marco del estudio de las desintegraciones radiativas a partir de los datos recogidos por el LHCb en colisiones pp. Por un lado, el estudio del proceso $\Lambda_b^0 \to p\pi^-\gamma$ en Run 1 ha permitido obtener una primera observación de una transición $b \to d\gamma$ en bariones, y supone un primer paso para obtener una medida de su fracción de desintegración, al que los datos del Run 2 le servirán para reducir el error estadístico. Esta medida, sin embargo, está sujeta a la medida de $\mathcal{B}(\Lambda_b^0 \to pK^-\gamma)$, que estará próximamente disponible ya que es claramente observable con los datos actuales de LHCb. Por otro, el desarrollo de las líneas de trigger radiativas inclusivas permite continuar con el estudio de estas desintegraciones en el Run 3 sin necesidad de desarrollar una línea para cada posible combinación de partículas en el estado final. Además, la actualización del BDT usando eventos simulados en condiciones de Run 3 permite distinguir con mejor poder de separación los eventos radiativos del resto, en comparación a la configuración entrenada con Run 2.

1 Introduction

The Standard Model of particle physics is the set of theories that aim to describe the fundamental structure of matter. The theory was developed in the latter half of the 20th century and has demonstrated a huge success in describing the results from particle physics experiments, namely, the prediction of the top quark, the tau neutrino or the properties of the W and Z bosons. Its greatest success came with the discovery of the long-anticipated Higgs boson in 2012, the last piece of the puzzle in the Standard Model, forty years after the particle was theorised.

Despite its astounding success, there are some phenomena in nature that the Standard Model is unable to describe. While the theory describes the electromagnetic, weak and strong interactions, it fails to provide a quantum-like description of the fourth fundamental force, gravity. In addition, it does not provide a dark matter candidate that matches the results from observational cosmology, a successful explanation for the accelerated expansion of the universe (dark energy), or fully explains the asymmetry between matter and antimatter in the universe either. On top of that, the nature of the neutrino masses to explain neutrino oscillation is still a matter of debate. A short description of the Standard Model and the relevant phenomenology for this thesis is presented in chapter 2.

One of the necessary conditions to explain the matter/antimatter asymmetry is to have a sufficient amount of *CP* violation, for which the Standard Model can only account for part of it. Therefore, it is vital to experimentally check the Standard Model predictions on *CP* violation, as any deviation would hint towards a New Physics (NP) process that enhances *CP* violation. In this sense, the LHCb experiment, one of the experiments in the Large Hadron Collider (LHC), aims to measure *CP*-violating effects through the interaction of heavy flavour hadrons, although it has also produced important results in many other areas.

Out of the many processes studied in LHCb, which is further described in chapter 3, the cases relevant for this thesis are those which are suppressed in the Standard Model, called rare decays. These processes involve at least one off-diagonal element of the Cabibbo-Kobayashi-Maskawa (CKM) matrix and are an excellent probe for NP. In particular, we focus on radiative decays, which are flavour-changing neutral currents (FCNC) of b hadrons, a type of interaction in which a b quark changes its flavour without altering its electric charge and emitting a photon. These processes are specially sensitive to NP since they are forbidden at tree-level in the Standard Model, and can only occur through loop diagrams.

The photon emitted in these interactions is highly energetic and is one of their key aspects when it comes to developing a trigger selection that can efficiently find them in the vast sea of particles produced in the pp collision. During Run 1, which corresponds to 2011 and 2012 and had pp collisions at a centre-of-mass energy of 7 and 8 TeV, respectively, the software trigger selection included inclusive lines that allowed for any potential event containing a high energetic photon to be recorded, along with some exclusive lines dedicated to the selection of specific, more common radiative decays. In Run 2, which comprises the 2015-2018 period and had the energy of the collisions increased to 13 TeV, dedicated inclusive radiative lines were deployed which increased by a factor two the efficiency selecting radiative decays. This increase was mainly due to the implementation of multivariate techniques that allowed to further exploit the common properties of these decays.

As part of the work for this thesis, the lines have been adapted to run in the Run 3 framework, which will start in 2022. In Run 3, the fast, hardware trigger will no longer be present and everything will be running on software, processing 30 million events per second. Therefore, the techniques used in Run 2 need to be reoptimised in order to be able to reduce the input data rate to a manageable level. The details of the inclusive trigger performance are given in chapter 4.

In this work we study the $\Lambda_b^0 \to p\pi^-\gamma$ process (we also imply the CP conjugates throughout the text), a baryonic FCNC with a $b \to d\gamma$ transition which has not been observed yet, using LHCb data collected during Run 1. The main challenge for studying this decay, apart from being heavily Cabibbo-suppressed according to the Standard Model, is that it is unclear which possible neutron resonance dominates the proton-pion mass spectrum. This means that the selection allows for a broad range of proton-pion masses, allowing contamination from other, more likely, radiative decays. This effect is mitigated in two ways: by restricting regions of the dihadron mass system and by applying charged particle identification criteria. Finally, the remaining cross-feed events are controlled using data by performing a simultaneous fit to the signal and the two main sources of cross-feed contamination. The details of the search of this decay using Run I data are provided in chapter 5.

Lastly, chapter 6 contains the conclusions of this work, as well as future prospects and possible improvements.

2 Theoretical framework

This chapter summarises the theoretical framework in which this thesis is developed. It outlines the main features of the Standard Model of Particle Physics, focusing on flavour physics and *CP* violation. The last section describes the physics behind the $\Lambda_b^0 \to p\pi^-\gamma$ process.

2.1 The Standard Model of Particle Physics

The Standard Model (SM) of Particle Physics is the theory that describes the most basic building blocks of the universe, the elementary particles, as well as three of the fundamental interactions between them: electromagnetism, weak force and strong force. Gravity is not included, since it has not been yet possible to make a satisfactory description within the SM framework and its effects, related to the mass of the elementary particles, are negligible in front of the other interactions involved (28 orders of magnitude smaller).

According to the SM, the elementary particles that make up all known matter are fermions, which have half-integer spin. In addition, SM fermions are classified in quarks and leptons depending upon whether they undergo strong interactions or not, respectively. Quarks and leptons still interact weakly and electromagnetically. Fermions are finally split in three generations, each generation containing a pair of quarks and leptons, with the particles from one generation being generally heavier than those from the previous one. Therefore, a total of six quarks (up (u), down (d), charm (c), strange (s), top (t) and bottom (b)) and 6 leptons (electron (e), electron neutrino (ν_e), muon (μ), muon neutrino (ν_μ), tau (τ) and tau neutrino (ν_τ)) are included in the SM. The list is summarised in Table 2.1. Moreover, each fermion has its corresponding antiparticle of the same mass but opposite quantum numbers.

Table 2.1: Fermions of the SM classified by generation.

	1st generation	2nd generation	3rd generation
Quarks	u	c	t
	d	s	b
Leptons	ν_e	ν_μ	ν_τ
	e	μ	τ

Table 2.2: Fermion doublets and singlets of the SM along their respective third weak isospin component (T_3), electric charge (Q) and weak hypercharge (Y).

	1st gen	2nd gen	3rd gen	T_3	Q	Y
Doublets	$\begin{pmatrix} u \\ d \end{pmatrix}_L$	$\begin{pmatrix} c \\ s \end{pmatrix}_L$	$\begin{pmatrix} t \\ b \end{pmatrix}_L$	$\begin{pmatrix} 1/2 \\ -1/2 \end{pmatrix}$	$\begin{pmatrix} 2/3 \\ -1/3 \end{pmatrix}$	1/3
	$\begin{pmatrix} \nu_e \\ e \end{pmatrix}_L$	$\begin{pmatrix} \nu_\mu \\ \mu \end{pmatrix}_L$	$\begin{pmatrix} \nu_\tau \\ \tau \end{pmatrix}_L$	$\begin{pmatrix} 1/2 \\ -1/2 \end{pmatrix}$	$\begin{pmatrix} 0 \\ -1 \end{pmatrix}$	-1
Singlets	u_R	c_R	t_R	0	2/3	4/3
	d_R	s_R	b_R	0	-1/3	-2/3
	e_R	μ_R	τ_R	0	-1	-2

The interactions in the SM are based on the local gauge invariance of the groups [1–5]:

$$\mathrm{SU}(3)_C \times \mathrm{SU}(2)_L \times \mathrm{U}(1)_Y \tag{2.1}$$

Where $\mathrm{SU}(3)_C$ is the group corresponding to the strong interactions, indicated by C, the colour charge; while $\mathrm{SU}(2)_L \times \mathrm{U}(1)_Y$ stands for the electroweak part of the theory, with the subscript L indicating it only couples to left-handed fermions and Y being the weak hypercharge, which relates to the electric charge (Q) and the weak isospin (T_3) by:

$$Q = \frac{Y}{2} + T_3 \tag{2.2}$$

In order to accommodate that only left-handed fermions couple to the $\mathrm{SU}(2)_L$ group, left-handed fermions are represented as weak isospin doublets, whereas right-handed fermions are singlets. Table 2.2 contains a summary of all fermion doublets and singlets of the SM.

Physically, the generators of each group correspond to the gauge bosons of the interaction, which are the carriers of the force and have spin 1. Therefore, the strong force has eight gauge bosons, the gluons (g); while the electroweak interaction has a total of four: the $W^\pm$ and Z bosons and the photon (γ). However, the group defined in Equation 2.1 does not allow for any of the particles to be massive, which is in contrast with experiments. To tackle this issue the symmetry group of the SM is spontaneously broken into:

$$\mathrm{SU}(3)_C \times \mathrm{U}(1)_Q \tag{2.3}$$

With $\mathrm{U}(1)_Q$ being the group of the electromagnetic interactions. The Higgs mechanism [6] is responsible of this spontaneous symmetry breaking, giving mass to the fermions and the $W^\pm$ and Z bosons, while keeping the gluons and the photon massless. This mechanism introduces a new interaction, the Higgs field, and predicts the existence of a scalar boson, the Higgs boson (H^0), which gives rise to the mass of the particles it interacts with. Table 2.3 summarises the bosons of the SM.

With the discovery of the Higgs boson forty years after it was theorised at the ATLAS experiment in 2012 [7], the SM puzzle was finally completed. During

Table 2.3: Bosons of the SM, associated interaction and mass.

Particle(s)	Interaction	Mass (GeV/c^2)
γ	Electromagnetic	0
$W^{\pm}$	Weak force	80.379
Z	Weak force	91.189
g	Strong force	0
H^0	Higgs field	125.10

these years, predictions on the existence of the W and Z bosons [8–11], gluons [12, 13] and heavy quarks [14–17] were also confirmed experimentally, as well as many of their properties. Despite its huge success explaining results from particle physics experiments, the SM is not complete, as it fails to properly explain some phenomena, namely: gravity, dark matter, dark energy and the observed baryon and *CP* asymmetries. Many theories have been proposed to extend the SM in order to accommodate part of these issues, like supersymmetry or string theory, however, no sign of Beyond the SM effects have been observed up to date.

2.2 *CP* violation in the Standard Model

CP-symmetry is a combination of charge (C) and parity (P) symmetries, and it states that the laws of physics are the same when both the particles are exchanged with their antiparticles (C-symmetry) and the spatial coordinates are inverted (P-symmetry). *CP* violation was believed to be one of the fundamental conservation laws of nature until 1964, when, *CP* violation was discovered in kaon decays [18].

The study of *CP* asymmetries in the SM is vital in the attempt to explain the baryon asymmetry observed in the universe, since it is one of the Sakharov conditions [19] required for baryogenesis, along baryon number violation, C violation and out-of-equilibrium interactions. However, just having *CP* violation is not enough, and the SM falls short to account for the observed matter-antimatter asymmetry in the universe. In fact, the only source of *CP* violation allowed in the SM comes from the CKM matrix [20], a mixing matrix that describes the relationship between the quark mass eigenstates and the quark weak interaction eigenstates:

$$V_{CKM} = \begin{pmatrix} V_{ud} & V_{us} & V_{ub} \\ V_{cd} & V_{cs} & V_{cb} \\ V_{td} & V_{ts} & V_{tb} \end{pmatrix} \tag{2.4}$$

The matrix must be unitary, so 9 real parameters are required. However, 5 of those parameters do not carry physical meaning, as they can be reabsorbed in the quark fields as relative phases, reducing the physical parameters to 4. In the most common parameterisation, those parameters are expressed as three Euler angles ($\theta_{12}, \theta_{23}, \theta_{13}$) and one *CP*-violating phase (δ), Denoting the cosines and sines of the

angles as c_{jk} and s_{jk}, respectively, the CKM matrix can be rewritten as:

$$V_{CKM} = \begin{pmatrix} 1 & 0 & 0 \\ 0 & c_{23} & s_{23} \\ 0 & -s_{23} & c_{23} \end{pmatrix} \begin{pmatrix} c_{13} & 0 & s_{13}e^{-i\delta} \\ 0 & 1 & 0 \\ -s_{13}e^{i\delta} & 0 & c_{13} \end{pmatrix} \begin{pmatrix} c_{12} & s_{12} & 0 \\ -s_{12} & c_{12} & 0 \\ 0 & 0 & 1 \end{pmatrix}$$
$$V_{CKM} = \begin{pmatrix} c_{12}c_{13} & s_{12}c_{13} & s_{13}e^{-i\delta} \\ -s_{12}c_{23} - c_{12}s_{23}s_{13}e^{i\delta} & c_{12}c_{23} - s_{12}s_{23}s_{13}e^{i\delta} & s_{23}c_{13} \\ s_{12}s_{23} - c_{12}c_{23}s_{13}e^{i\delta} & -c_{12}s_{23} - s_{12}c_{23}s_{13}e^{i\delta} & c_{23}c_{13} \end{pmatrix} \tag{2.5}$$

Finding these values is an important test of the SM, and one of the main objectives of the LHCb experiment. For the *CP*-violating phase in particular, one needs to study weak decays of heavy quarks, which are the ones that carry this information. The current experimental values for the 4 physical parameters are [21]:

$$\begin{aligned} s_{12} &= 0.22650 \pm 0.00048 \quad & s_{13} &= 0.00361^{+0.00011}_{-0.00009} \\ s_{23} &= 0.04053^{+0.00083}_{-0.00061} & \delta &= 1.196^{+0.045}_{-0.043} \end{aligned} \tag{2.6}$$

These results state a hierarchy in the CKM matrix: the mixing between the first two generations is stronger than that between the last two, with the mixing between first and third being the weakest. One of the consequences of this is that in B decays, which are the case study in this thesis, processes where the b quark decays into a state with a second generation quark are more likely to occur than those with a first generation quark.

2.3 Radiative B decays

The processes of interest in this work are radiative B decays, a type of FCNC mediated by a $b \to q\gamma$ transition at quark level, where q can either be an s or d quark. These processes are forbidden at tree-level in the SM and are sensitive to NP processes. The dominant Feynman diagram of the $b \to d\gamma$ transition can be seen in Figure 2.1.

From a more formal point of view, the effective Hamiltonian describing the $b \to d\gamma$ transitions is [22]:

$$\mathcal{H}_{eff} = -\frac{4G_F}{\sqrt{2}} \left(V_{td}^* V_{tb} \mathcal{H}_{eff}^{(t)}(\mu_b) + V_{ud}^* V_{ub} \mathcal{H}_{eff}^{(u)}(\mu_b) \right) \tag{2.7}$$

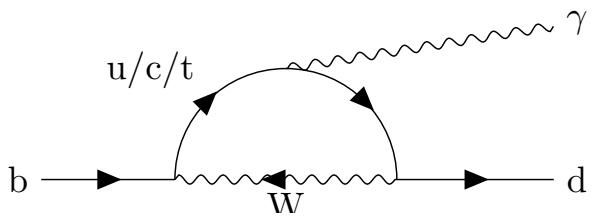

Figure 2.1: Dominant Feynman diagram of the $b \to d\gamma$ transition.

Where G_F is the Fermi constant, $\mu_b = m_b$ is the relevant scale (the mass of the b quark) and

$$\mathcal{H}_{eff}^{(t)}(\mu_b) = \sum_{i=1}^{2} C_i(\mu_b)\mathcal{O}_i^c(\mu_b) + \sum_{i=3}^{6} C_i(\mu_b)\mathcal{O}_i(\mu_b) + \sum_{i=7}^{10} \left[C_i(\mu_b)\mathcal{O}_i(\mu_b) + C_i'(\mu_b)\mathcal{O}_i'(\mu_b)\right]$$
$$\mathcal{H}_{eff}^{(u)}(\mu_b) = C_1(\mu_b)\left[\mathcal{O}_1^c(\mu_b) - \mathcal{O}_1^u(\mu_b)\right] + C_2(\mu_b)\left[\mathcal{O}_2^c(\mu_b) - \mathcal{O}_2^u(\mu_b)\right] \tag{2.8}$$

With $C_i(\mu_b)$ the Wilson coefficients and $\mathcal{O}_i(\mu_b)$ the local effective operators built from the operator product expansion formalism [23]. The main operators contributing to the $b\to d\gamma$ transition are $\mathcal{O}_1(\mu_b)$, $\mathcal{O}_2(\mu_b)$, $\mathcal{O}_7(\mu_b)$ and $\mathcal{O}_7'(\mu_b)$, defined as:

$$\begin{aligned}
\mathcal{O}_1^q(\mu_b) &= \left(\bar{d}_{L\alpha}(\mu_b)\gamma_\mu q_{L\beta}(\mu_b)\right)\left(\bar{q}_{L\beta}(\mu_b)\gamma^\mu b_{L\alpha}(\mu_b)\right)\\
\mathcal{O}_2^q(\mu_b) &= \left(\bar{d}_{L\alpha}(\mu_b)\gamma_\mu q_{L\alpha}(\mu_b)\right)\left(\bar{q}_{L\beta}(\mu_b)\gamma^\mu b_{L\beta}(\mu_b)\right)\\
\mathcal{O}_7(\mu_b) &= \frac{e^2}{16\pi^2} m_b \bar{d}(\mu_b)\sigma_{\mu\nu} b_R(\mu_b) F^{\mu\nu}(\mu_b)\\
\mathcal{O}_7'(\mu_b) &= \frac{e^2}{16\pi^2} m_b \bar{d}(\mu_b)\sigma_{\mu\nu} b_L(\mu_b) F^{\mu\nu}(\mu_b)
\end{aligned} \tag{2.9}$$

Where $q(\mu_b)$, $d(\mu_b)$, $b(\mu_b)$ are the respective quark fields at the scale of the b mass, γ the gamma matrices, $F^{\mu\nu}(\mu_b)$ the electromagnetic tensor, also at the μ_b scale, and $\sigma_{\mu\nu}$ are the generators of the Lorentz group in the spinor representation [24]

Among all these, the leading term is the one with the $\mathcal{O}_7^{(\prime)}(\mu_b)$ operator, so that the effective Hamiltonian from Equation 2.7 reads:

$$\mathcal{H}_{eff} \approx -\frac{4G_F}{\sqrt{2}} V_{td}^* V_{tb}\Big[C_7(\mu_b)\mathcal{O}_7(\mu_b) + C_7'(\mu_b)\mathcal{O}_7'(\mu_b)\Big] \tag{2.10}$$

Since the weak interaction only affects left-handed particles, the C_7' coefficient is suppressed with respect to C_7 by a factor m_d/m_b. This accounts for the chirality flip required in the interaction, which can only happen if the quarks are massive.

In order to obtain the effective Hamiltonian for $b\to s\gamma$ transitions, one just needs to replace the d quark by an s quark. This means that the branching ratio (BR) of a $b\to d\gamma$ over a $b\to s\gamma$ transition is approximately:

$$\frac{\mathcal{B}(b\to d\gamma)}{\mathcal{B}(b\to s\gamma)} \approx \left|\frac{V_{td}}{V_{ts}}\right|^2 = 0.047 \pm 0.003 \tag{2.11}$$

Nevertheless, this approximation does not take into account differences between the hadron factors in play, nor the fact that while $|V_{us}^* V_{ub}| << |V_{ts}^* V_{tb}|$ holds, $|V_{ud}^* V_{ub}|$ and $|V_{td}^* V_{tb}|$ are of the same order of magnitude, which can account for up to a $O(15\%)$ correction [25, 26].

2.3.1 The $\Lambda_b^0 \to p\pi^-\gamma$ decay

Since quarks are bound to each other forming hadrons, $b\to d\gamma$ transitions must be studied within a given hadron. In this work, the process is studied in Λ_b^0 baryons

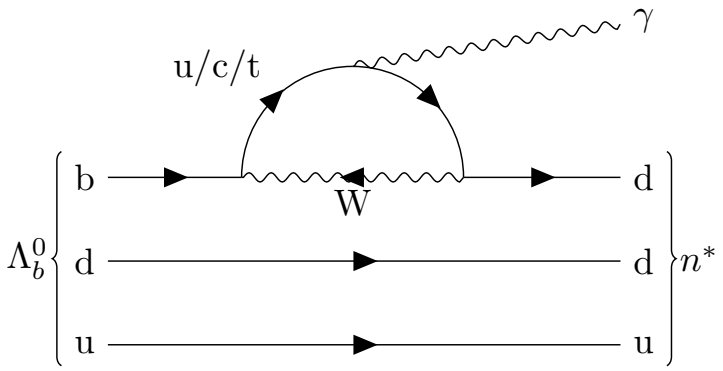

Figure 2.2: Dominant Feynman diagram of the $\Lambda_b^0 \to n^*\gamma$ decay.

decaying into a neutron resonance (n^*) and a photon, where two spectators quarks are present (see Figure 2.2). A ground-state neutron can also be produced in the process, but it is not taken into account in this analysis since it cannot decay into $p\pi^-$.

Many n^* have been already experimentally confirmed [27], and those with mass lower than $2.2\,\text{GeV}/c^2$ are displayed in Table 2.4. On top of that, the rate at which each one is produced in $\Lambda_b^0 \to n^*\gamma$ decays is currently unknown, and their branching fraction (BF) into $p\pi^-$ is also poorly known and seems to vary greatly on each resonance [21]. To accommodate this problem, the Λ_b^0 is directly reconstructed from a proton and a pion of opposite charge and a photon, without further constraints on the mass of the possible n^* resonance other than being below the $2.2\,\text{GeV}/c^2$ threshold. The main purpose of this threshold is to remove events with a high dihadron invariant mass, since it has been observed in $\Lambda_b^0 \to pK^-J/\psi$ decays [28] that the main contribution to the pK^- mass comes from the lightest Λ^{*0} resonances, and the same applies to the n^*. In addition, the threshold removes events that contain massive intermediate particles, like J/ψ, which are an important source of background when combined with a random photon present in the event.

The normalisation mode, $\Lambda_b^0 \to pK^-\gamma$, presents the same issue as the signal mode, where there is a variety of Λ^{*0} resonances [29, 30]. In this case, the Λ_b^0 is reconstructed from a proton and a kaon of opposite charge and a photon. Similarly to the signal mode, the main contributions to the pK^- mass comes from the lightest Λ^{*0} resonances. Therefore, the same $2.2\,\text{GeV}/c^2$ cut can be applied while keeping almost all $\Lambda_b^0 \to pK^-\gamma$ events.

Table 2.4: List of neutron resonances in the 1440-2200 MeV range with at least a "existence is very likely" status, as in [21].

Particle	Mass (MeV)	J^P
N(1440)	1370 ± 15	$\left(\frac{1}{2}\right)^+$
N(1520)	1510 ± 5	$\left(\frac{3}{2}\right)^-$
N(1535)	1510 ± 20	$\left(\frac{1}{2}\right)^-$
N(1650)	1655 ± 15	$\left(\frac{1}{2}\right)^-$
N(1675)	1660 ± 5	$\left(\frac{5}{2}\right)^-$
N(1680)	1675 ± 10	$\left(\frac{5}{2}\right)^+$
N(1700)	1700 ± 50	$\left(\frac{3}{2}\right)^-$
N(1710)	1720 ± 50	$\left(\frac{1}{2}\right)^+$
N(1720)	1675 ± 15	$\left(\frac{3}{2}\right)^+$
N(1875)	1875 ± 75	$\left(\frac{3}{2}\right)^-$
N(1880)	1870 ± 40	$\left(\frac{1}{2}\right)^+$
N(1895)	1907 ± 10	$\left(\frac{1}{2}\right)^-$
N(1900)	1920 ± 20	$\left(\frac{3}{2}\right)^+$
N(2060)	2070 ± 50	$\left(\frac{5}{2}\right)^-$
N(2100)	2100 ± 50	$\left(\frac{1}{2}\right)^+$
N(2120)	2120 ± 50	$\left(\frac{3}{2}\right)^-$
N(2190)	2100 ± 50	$\left(\frac{7}{2}\right)^-$

3 The LHCb experiment inside LHC

This chapter describes the main features of the Large Hadron Collider (LHC), while providing a more detailed description of the LHCb detector.

3.1 The Large Hadron Collider

The LHC is the world's largest and most powerful particle accelerator to date [31]. In consists in a 27-kilometre long ring of superconducting magnets, lying in a tunnel as deep as 175 metres beneath the surface. The accelerator is located in the main site of the European Organisation for Nuclear Research (CERN), at the Franco-Swiss border near Geneva.

Inside the accelerator, two beams of high-energy particles travel in opposite directions in separate pipes, at speeds close to the speed of light. The particles are guided through the ring by superconducting electromagnets, which need a temperature of -271.3° C to operate, until they reach the target energy and are deflected to collide. The collisions occur at four different locations around the ring, where the four big particle detector are located: ATLAS [32], CMS [33], LHCb [34] and ALICE [35].

The main program of the LHC consists in pp collisions, although it also provides heavy-ion collisions, which study is the objective of the ALICE detector. The protons collide at very high centre-of-mass energies ($\sqrt{s}$), starting at 7 TeV during 2010 and 2011, 8 TeV in 2012 and reaching 13 TeV from 2015 to 2018. During run 3, which is planned to start in 2022, the energy will be increased to 14 TeV.

3.2 The LHCb experiment

The work of this thesis is included within the LHCb physics program. The LHCb detector [34,36] is a single-arm forward spectrometer (Figure 3.1) covering the pseudorapidity[1] range $2 < \eta < 5$, designed for the study of particles containing b or c quarks, which are mainly produced in the forward and backward regions (Figure 3.2). The primary objective of the detector is to study the asymmetry between matter and antimatter in the universe, although it has also shown success in other

[1]The pseudorapidity is defined as $-\ln\left[\tan\left(\frac{\theta}{2}\right)\right]$, with θ being the angle with respect to the beam axis.

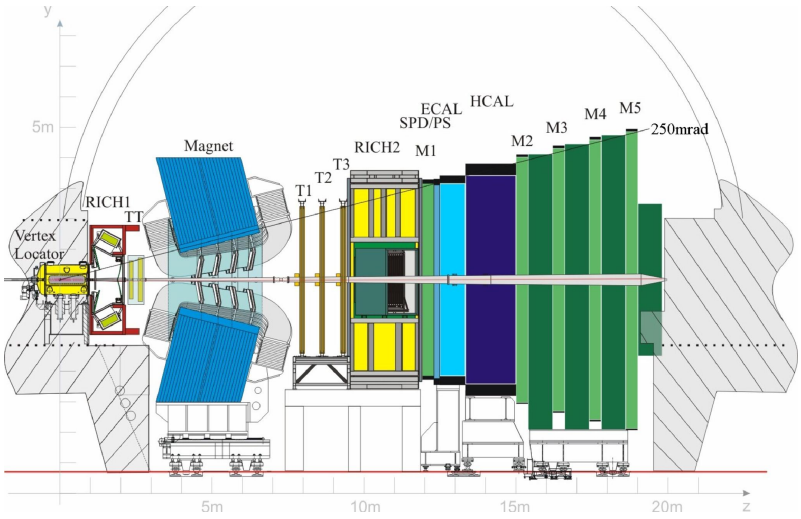

Figure 3.1: Lateral view of the LHCb detector. The sub-detectors are marked.

areas like exotic hadron spectroscopy or electroweak physics. The different sub-detectors the LHCb is made of can be divided into two independent systems: the tracking system and the particle identification (PID) system. In addition, the LHCb detectors include a trigger system, which combines information from dedicated sub-detectors and the previous systems to reduce the input rate to a manageable level while keeping as many interesting events as possible.

3.2.1 The tracking system

The tracking system is in charge of reconstructing the pp interaction point, also known as Primary Vertex (PV), as well as the trajectory of the charged particles produced. It consists in four sub-detectors: the Vertex Locator (VELO), the Tracker Turicensis (TT), the dipole magnet and the T1-T3 tracking stations.

The **Vertex Locator** (VELO) [37] surrounds the interaction point and its primary goal is the identification of the PV and the point where the b- or c- hadron decays, the Secondary Vertex (SV). It consists in a series of disk-shaped silicon modules centred around the beam pipe that provide a measure of the r and ϕ coordinates. To achieve better precision, the VELO sensors are placed at a radial distance from the beam smaller than the aperture required by the LHC in the injection phase, when protons are being injected into the ring and the beam is still unstable. Therefore, the sensor discs are divided in two halves that are kept away from the beam while it is unstable and put back together once the physics measurements may begin.

The **Tracker Turicensis** (TT) [38] is situated directly downstream the VELO. It is a 150 cm wide and 130 cm high planar tracking station made of four layers of silicon microstrip sensors. The layout of the microstrip sensor varies from one layer to another, being vertical in the first and fourth layers, and rotated $\mp 5°$ in the second and third, respectively.

The **dipole magnet** [39] generates an approximately constant magnetic field in

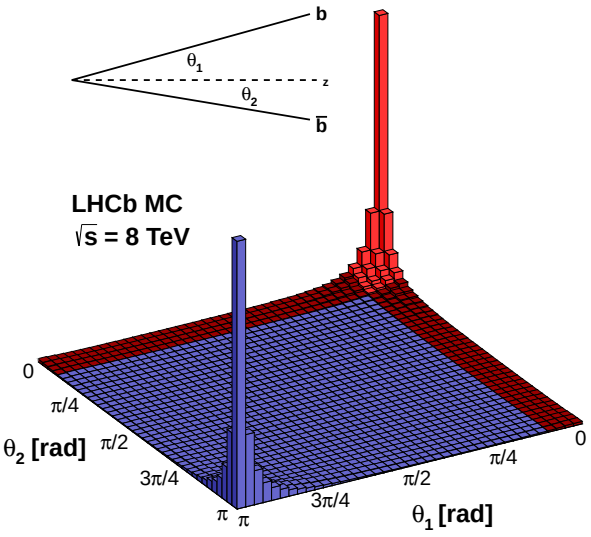

Figure 3.2: Angular distribution of the $b\bar{b}$ pairs produced in pp collisions at $\sqrt{s} = 8\,\text{TeV}$. The z-axis corresponds to the beam direction.

the vertical axis, deflecting charged particles in the horizontal plane. It provides an integrated field of about 4 T m, bending positive and negative particles in opposite directions and allowing for a precise measurement of the particle's momentum. In order to reduce systematic effects from detector asymmetries, about half of the data is taken with the magnet polarity up and the other half with polarity down.

The **T stations** (T1-T3) [40, 41] are located downstream the magnet and are divided in two regions: the **Inner Tracker** (IT) and the **Outer Tracker** (OT). The IT is built with the same silicon microstrips as the TT and covers the innermost part of the detector. On the other hand, the OT is a straw-tube detector covering the outermost part, in which charged particles traversing the straw-tubes ionise the gas along their trajectory.

The trajectories of the charged particles traversing the tracking system are reconstructed from hits in the VELO, TT and T1-T3 detectors. Depending on their paths through LHCb, the following track types are defined, as illustrated in Figure 3.3:

- **Long tracks** traverse the full tracking system. They have hits in both the VELO and the T stations, and optionally in the TT. Since they traverse the full magnetic field they have the most precise momentum measurement.

- **Upstream tracks** generally have low momentum, so they only traverse the VELO and TT stations. However, they pass the RICH1 detector and are therefore useful to understand backgrounds in the PID algorithm of the RICH, which is described afterwards in this chapter.

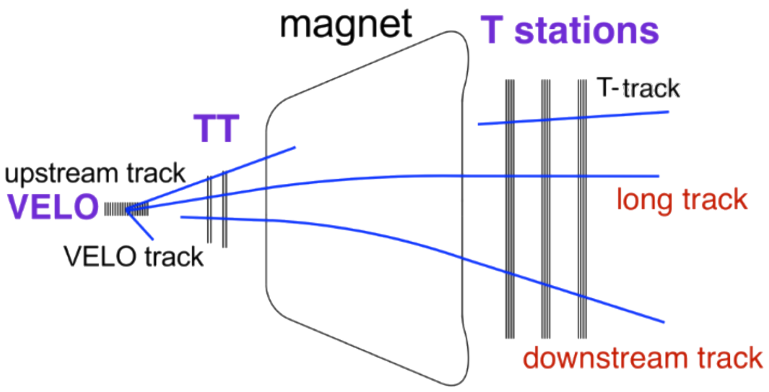

Figure 3.3: A schematic illustration of the various track types in LHCb [42]: long, downstream, upstream, VELO and T tracks.

- **Downstream tracks** pass only through the TT and T stations. They are important for the reconstruction of neutral long-lived particles, like the Λ_b^0 or the K_S^0, that leave no signal in the tracking detectors before they decay outside the VELO.
- **VELO tracks** pass only through the VELO and are typically large-angle or backward tracks. They are useful for the reconstruction of the PV.
- **T tracks** only traverse the T stations. They are typically produced in secondary interactions and are useful for the optimisation of the PID algorithm of the RICH, since they traverse the RICH2 detector.

3.2.2 The particle identification system

The particle identification system is important for LHCb (and any other flavour physics experiment) mainly to separate kaons from pions, which is done with the **RICH detectors**. Additionally, π^0 and γ are identified by making use of the **calorimeters**, while the **muon chambers** focus on identifying muons produced in the pp collision.

- The **Ring Imaging Cherenkov** (RICH) detectors [43] consist in two sub-detectors: the RICH1, placed immediately downstream the VELO; and the RICH2, located downstream the T stations. The RICH1 sub-detector uses aerogel (only in Run 1) and C_4F_{10} radiators, covering the low-momentum range $\sim$ 1-60 GeV/c, while the RICH2 uses a CF_4 radiator and covers the high-momentum range, starting at $\sim$15 GeV/c and going up to and beyond 100 GeV/c (see Figure 3.4). The system measures the velocity of the charged particles traversing the medium of the detector using the Cherenkov radiation [44] emitted. This information, combined with the momentum measurement in the tracking system, allows the identification of charged particles. The Cherenkov light emitted is focused using a combination of spherical and flat mirrors that reflect the light out of the spectrometer acceptance.
- The **calorimeter system** [45] provides the identification of electrons, pho-

tons and hadrons, as well as the measurement of their energies and positions and selecting transverse energy candidates for the first trigger level (L0). The calorimeter is situated downstream the RICH2 detector and is composed by a scintillator pad detector (SPD), a preshower detector (PS), an electromagnetic calorimeter (ECAL) and a hadron calorimeter (HCAL), in that order. All four sub-detectors adopt a variable lateral segmentation, since the hit density greatly varies from the part closest to the beam to the outermost part. The SPD selects charged particles, which allows the rejection of π^0's with high E_{T} from actual electron candidates, while the PS selects electromagnetic particles, allowing the rejection of charged hadrons. The ECAL is a sampling scintillator/lead structure with a thickness of 25 radiation lengths, which is able to fully contain the showers of high energetic photons. Hadrons barely interact with the ECAL, triggering a particle shower in the HCAL, which is made of iron and scintillating tiles. The HCAL does not require such a stringent particle shower containment condition, so its thickness is set to 5.6 interaction lengths due to space limitations.

- The **muon chambers** [46] are composed of five stations (M1-M5) of rectangular shape equipped predominantly with Multi Wire Proportional Chambers (MWPC), except in the highest rate region of M1, where triple Gas Electron Multiplier (GEM) detectors, which are capable of working at a much higher rate, are used. The M1 station is placed upstream the calorimeters, while the other stations are downstream. These M2-M5 stations are interleaved with iron absorbers 80 cm thick to select penetrating muons, which require a minimum momentum of approximately 6 GeV/c to cross the five stations. On the other hand, the M1 station is used to improve the p_{T} measurement in the trigger. The stations have a projective geometry, meaning that their transverse dimensions scale with the distance from the interaction point.

3.2.3 The trigger system

The LHC provides a beam crossing rate of 40 MHz, which needs to be reduced to a manageable level of a few kHz (∼5 kHz in Run 1 and ∼12.5 kHz in Run 2). This reduction is achieved in two trigger levels: a hardware first level trigger (L0) and a software high level trigger (HLT) stage. Figure 3.5 shows the LHCb trigger dataflow for Run 1 and Run 2, as well as the design for Run 3, which is further discussed in chapter 4.

- The **L0** is a fast, hardware-driven system aiming to reduce the incoming 40 MHz beam crossing rate to 1 MHz. It is divided in 3 subsystems: the L0-Calorimeter trigger, which uses the information for the calorimeters to reconstruct the electron, photons and hadrons with the highest E_{T}; the L0-Muon trigger, which reads the output of the muon chambers to reconstruct the two muons with the highest p_{T}; and the L0-PileUp trigger, which is not used to reconstruct physics events but to determine the luminosity.

- The **HLT** takes the output of the L0 with the goal of reducing the event rate to the kHz level. Unlike the L0, it is a software system that runs separate

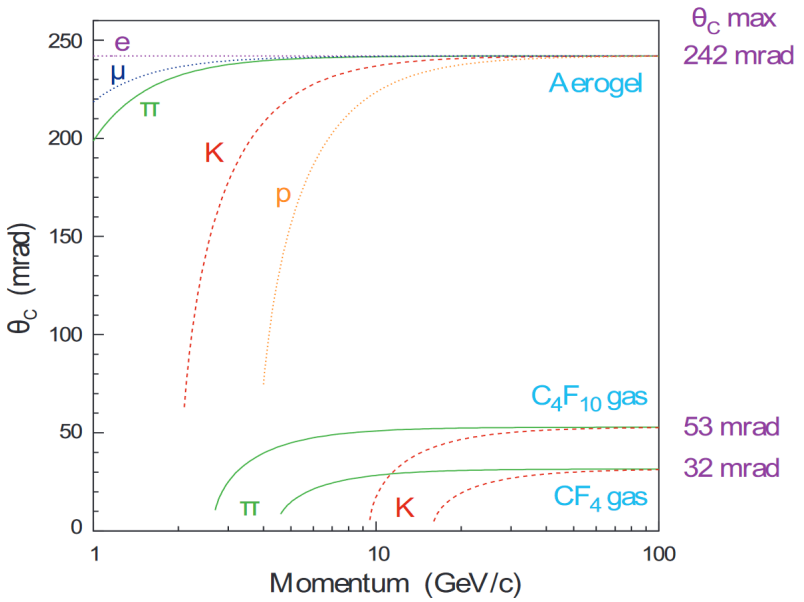

Figure 3.4: Cherenkov angle versus particle momentum for the RICH radiators ([43]).

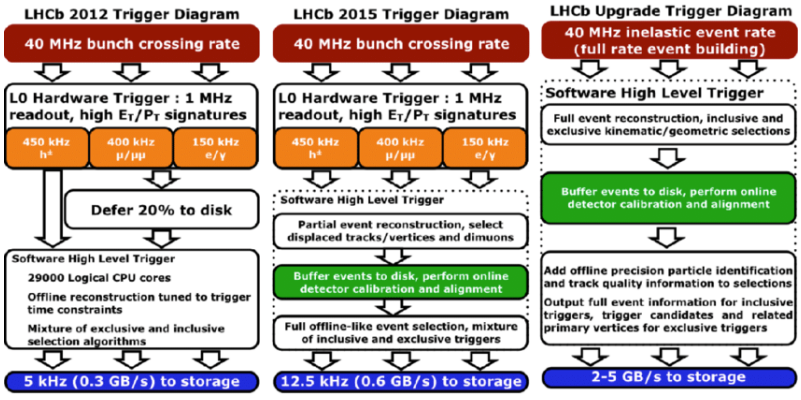

Figure 3.5: Diagrams of the LHCb trigger data-flow in Run 1 (left), Run 2 (centre) and the one foreseen for Run 3 (right) [47].

from the detector in the Event Filter Farm (EFF) and uses all of LHCb sub-detectors to reconstruct the full event. The HLT is actually sub-divided in two stages: the HLT1, which performs a partial event reconstruction to reduce the rate to $\sim 40\,\text{kHz}$; and the HLT2, which does a full event reconstruction to eventually reduce the rate to 5 (Run 1) or 12.5 kHz (Run 2).

While the L0 system remained the same between Run 1 and 2, the HLT underwent important changes in its data-flow. During Run 1, 20% of the L0 output was deferred to disk to be later processed while LHCb was not taking data. Furthermore, the alignment and calibration of the detector was performed offline using the data processed by the HLT, meaning that the whole data had to be re-processed in order to had its calibration updated. In Run 2, the computational power of the EFF was increased so now the whole L0 output could be fed into the HLT system. However, a change was introduced to perform online detector calibration and alignment: the HLT processing would be halted in order to use the HLT1 output to calibrate, before running the HLT2. After performing the necessary adjustments, it would then be run with the updated calibration.

This online processing will be taken a step further in Run 3 with the implementation of a real-time analysis strategy, where the full event reconstruction will be performed in real-time solely using software, without the aid of a hardware trigger.

4 Development of the Run 3 inclusive radiative trigger

It has been discussed in section 2.3 the importance of radiative decays in the search of NP. For that reason, LHCb has always had different HLT2 trigger lines dedicated to the selection of radiative decays. In Run 1, these radiative lines were focused on selecting $B^0 \to K^{*0}\gamma$ and $B_s^0 \to \phi\gamma$ exclusively, which meant that to study other radiative decays using Run 1 data, like in this thesis, one has to use trigger lines that select a number of hadrons, but do not exploit the peculiarities of having a high-energetic photon.

For that reason, inclusive radiative trigger lines were developed for Run 2, which increased the efficiency at which radiative decays are selected. Following their success, these lines are being carried over Run 3, for which we present their preliminary performance in terms of efficiency and bandwidth, using simulation samples that aim to reproduce the Run 3 conditions.

4.1 The inclusive radiative trigger in Run 2

The design of the inclusive radiative trigger is inspired by the topological trigger [48], which uses multivariate techniques to select events with at least 2 charged tracks. In addition, the radiative trigger looks for events containing a high-energetic photon, which is characteristic of radiative decays.

The inclusive radiative HLT2 selections are split in two: `RadiativeIncHHGamma` and `RadiativeIncHHHGamma`, which select combinations of two- and three-body candidates plus a high energetic photon, respectively. These two selections, often referred as lines, include both direct and converted photons. Direct photons are photons that have reached the calorimeter and produced an electromagnetic cascade, while converted photons have created an electron-positron pair beforehand by interacting with the detector material.

All lines follow the same selection steps. First, two or three particles, (either charged, K_S^0 or Λ) are reconstructed with a loose selection, based on a few topological and kinematic variables. This two- or three-body system is then combined with a high-energy photon to form the preliminary b candidate. Finally, a dedicated selection is performed in it by exploiting the common decay topology of b-radiative

Table 4.1: Simulated signal samples used to optimise the radiative inclusive triggers for Run 2.

2-body selection	3-body selection
$B^0 \to (K^{*0} \to K^+\pi^-)\gamma$	$B^+ \to (K_1^+(1270) \to K^+\pi^-\pi^+)\gamma$
$B_s^0 \to (\phi \to K^+K^-)\gamma$	$B_s^0 \to (\phi \to K^+K^-)(\phi \to K^+K^-)\gamma$
$B^0 \to K^+\pi^-\gamma$	
$B^+ \to (K^{*+} \to K^+\pi^+\pi^-)\gamma$	
$\Lambda_b^0 \to (\Lambda^{*0} \to pK^-)\gamma$	

decays with a Bonsai Boosted Decision Tree (BBDT), which performs much faster than a typical BDT by binning the multidimensional space formed by the input variables [49].

A single BBDT was trained for both trigger lines, which includes a discrete variable to identify whether an input event includes a two- or three-body candidate. The training was done with a set of simulation samples under 2015 conditions. For the signal proxy, 10^5 candidates were generated for each decay mode listed in Table 4.1, requiring the reconstructed particles to match the generated ones, besides requiring a photon with E_{T} above 1.5 GeV. For the two-body configuration, modes with two or three particles and a photon in the final state were used in the training, while the three-body configuration was trained using modes with three or four particles in the final state, plus a photon. For the background proxy, a simulated minimum bias sample was used; although the final configuration was retrained using the first data provided by LHCb in 2015 to achieve better performance [50].

One of the key points in the trigger lines is the absence of cuts in the mass variables. Instead, cuts are applied on the corrected mass, which is defined as:

$$m_{corr} = \sqrt{m^2 + |p_{\mathrm{T}miss}|^2} + |p_{\mathrm{T}miss}| \tag{4.1}$$

Where m is the reconstructed invariant mass of the b-candidate and $|p_{\mathrm{T}miss}|$ is the missing transverse momentum reconstructed with respect to the flight direction of the candidate. In other words, $|p_{\mathrm{T}miss}|$ is the component of the reconstructed momentum (as the sum of the momentum of the daughters) perpendicular to the direction of flight of the mother particle, which is determined from the initial and end vertices. This variable is designed to recover as much as possible the momentum lost by the missing particles in partially reconstructed decays. For example, when a massless particle is missing, it recovers the mass of the head of the decay, with its performance degrading with the number of missing particles. This allows for the three-hadron line to be able to select decays with a higher number of hadrons.

4.2 The inclusive radiative trigger in Run 3

At the time of this thesis, the inclusive radiative trigger lines are in a functional preliminary state, meaning they are not in their definitive state and are still suscep-

Table 4.2: List of Run 3 inclusive radiative trigger lines.

Name	Decay tree
`Hlt2BToHHGamma_Inclusive_Line`	$B^0 \to (h^+h^-)\gamma$
`Hlt2BToHHGammaEE_Inclusive_Line`	$B^0 \to (h^+h^-)\gamma$
`Hlt2BToHHHGamma_Inclusive_Line`	$B^+ \to (h^+h^-h^+)(\gamma \to e^+e^-)$
`Hlt2BToHHHGammaEE_Inclusive_Line`	$B^+ \to (h^+h^-h^+)(\gamma \to e^+e^-)$

tible to changes. The lines keep the same structure from Run 2, with few changes to adapt to the Run 3 framework. The main difference lies in the separation between direct and converted photons, for a total of four radiative lines Table 4.2, depending on whether two or three charged hadrons are reconstructed and whether the photon is converted or not.

The main difference in the trigger strategy between Run 2 and Run 3 is the removal of the hardware trigger, L0, leaving only a software-based trigger, with a HLT1 and a HLT2 stage. The HLT1 stage will be responsible for reducing the input rate from LHCb by performing a fast track reconstruction based on Graphics Processing Units (GPUs) [51]. GPUs are a great choice to perform trigger and reconstruction duties as they excel at data parallel tasks and map well onto LHCb's data acquisition architecture.

A second big difference lies on the output of the HLT2 lines. While in Run 2 the inclusive radiative lines are part of the full stream, which saves the whole underlying event after a positive trigger response; in Run 3 all HLT2 lines will be run as in the Turbo Stream [52], keeping only the information of the particles within the decay chain and discarding the storage of the underlying event. This is specially critical for the inclusive lines, which aim to keep events with a high-energetic photon, no matter the number of charged hadrons present in the decay. To compensate for this change, the lines keep the same main reconstruction as in Run 2, looking for two- or three-body decays plus a photon, while a handful of interesting underlying particles, including K^0_S, Λ, π^0, γ and charged hadrons are also saved, but not the whole event.

The selection steps are as follows: first, two opposite charged hadrons are selected and combined into an intermediate particle, requiring that both have originated at the same point, to which a third charged hadron is added in the case of the three-hadron line. Then, a photon is added to the hadron combination (either direct or converted depending on the line) to form the preliminary b candidate. Finally, the main decay event is put through a BDT to exploit the main features of radiative decays to further suppress the background [53]. For Run 3, each line has its own BDT, which is trained using simulated signal samples reproducing Run 3 conditions Table 4.3, as well as minimum bias MC. BDTs are being used during the development of the lines as they are easier to manage and work with than BBDTs, although the final BDTs will be converted into BBDTs before starting the data-taking period. The variables used in each BDT (Table 4.4) are mostly inherited from the Run 2 configuration, aiming to inclusively select radiative decays, either fully or partially

Table 4.3: Simulated signal samples used to optimise the radiative inclusive triggers for Run 3.

2-body selection	3-body selection
$B^+ \to (K^{*+} \to K^+\pi^+\pi^-)\gamma$	$B^+ \to (K^{*+} \to K^+\pi^+\pi^-)\gamma$
$B_s^0 \to (\phi \to K^+K^-)\gamma$	
$B^0 \to (K^{*0} \to K^+\pi^-)\gamma$	

Table 4.4: List of variables used to optimise the inclusive radiative trigger BDTs (DOCA = Distance Of Closest Approach between two particles, #(child(condition)) = number of children particles from the reconstructed b hadron (either charged hadron, ΛK_S^0 or γ) that pass a certain condition). `Hlt2BToHHGammaEE` and `Hlt2BToHHHGammaEE` use the same set.

`Hlt2BToHHGamma`	`Hlt2BToHHHGamma`	`Hlt2BToHH(H)GammaEE`
B $\chi^2_{\mathrm{IP_{PV}}}$	B $\chi^2_{\mathrm{IP_{PV}}}$	B m_{corr}
h min($\chi^2_{\mathrm{IP_{PV}}}$)	h min($\chi^2_{\mathrm{IP_{PV}}}$)	B χ^2_{vtx}
γ p_{T}	γ p_{T}	sum($h^{\pm}p_{\mathrm{T}}$)
-	γ p	B η
B m_{corr}	B m_{corr}	B χ^2_{VD}
(h^+h^-) m_{corr}	-	min($h^{\pm}p_{\mathrm{T}}$)
B $\chi^2_{\mathrm{FD_{PV}}}$	B $\chi^2_{\mathrm{FD_{PV}}}$	#(child ($\chi^2_{\mathrm{IP_{PV}}} < 16$))
B χ^2_{vtx}	B χ^2_{vtx}	B $\chi^2_{\mathrm{IP_{PV}}}$
DOCA (h^+, h^-)	$h^{\pm}$ Track max(χ^2/ndf)	#(child ($\chi^2_{\mathrm{IP_{PV}}} > 16$ & $p_{\mathrm{T}} > 1\,\mathrm{GeV}$))

reconstructed, in front of combinatorial background. The final cut of each BDT is constrained by the desired output rate, measured on the minimum bias sample, which is established to be around 0.1 kHz for each line.

In addition to the particles belonging to the main decay tree, a set of extra particles is saved along in order to be able to reconstruct other types of radiative decays which can only be partially reconstructed using the two- or three-body plus a photon scheme. The criteria used to select the extra particles is shared among all four inclusive radiative lines, although it might be modified in the future. The selection uses few variables to apply looser cuts on each type of particle, compared to the requirements for the main decay tree. The list of extra particles saved from the underlying event includes:

- Charged hadrons, with good reconstruction, not directly coming from any PV and with high p_{T}. No PID requirements are applied.
- $K_S^0 \to \pi^+\pi^-$ with an invariant mass close to that of the K_S^0, not coming from any PV and with high p_{T}. Both long and downstream tracks are used to reconstruct the K_S^0, with slight changes in the selection criteria for each.
- $\Lambda \to p\pi^-$ with an invariant mass close to that of the Λ, not coming from any PV and with high p_{T}. Both long and downstream tracks are used to reconstruct the Λ, with slight changes in the selection criteria for each.

- Photons with high p_{T}.
- Merged π^0 with high p_{T}, where the two photons emerging from the decaying π^0 are reconstructed as a single cluster in the ECAL.
- Resolved π^0 with high p_{T}, where the emerging photons are reconstructed separately.

4.3 Expected performance

In this section we show the preliminary expected performance in Run 3 of the inclusive radiative lines. The results have been obtained on simulated data samples because Run 3 data-taking is planned to begin in 2022.

The expected performance of the lines in Run 3 cannot be directly compared to that in Run 2, as the detector conditions and the data fed into HLT2 are quite distinct. However, it is possible to compare the performance between the old BDT, trained with Run 2 data, and the new BDTs, which have used Run 3 simulation, using the same testing samples and the same set of variables, in order to check that retraining actually improves the performance. Figure 4.1 shows the rate at which the trigger line accepts an event in front of the signal efficiency, which is composed by the mixture presented in Table 4.3. For any of the four lines, these plots show an overall improved performance when using the new BDTs, providing an increased signal efficiency when working at the same acceptance rate.

After showing an improved performance due to the retraining of the classifiers, we must choose a cut on the classifier output. The limiting factor in this case is the acceptance rate, which is estimated to about 0.1 kHz for each line. With this threshold, we compute the efficiency of each line when acting on different simulated signal samples as:

$$\epsilon = \frac{\#\text{ accepted events}}{\#\text{ input events}} \tag{4.2}$$

The choice in denominator means that the efficiencies given in Table 4.5 do not take into account that part of these input events will be previously rejected either by the HLT1 stage or by the reconstruction algorithms, nor that the events containing converted photons compose only about 10% of the simulated sample. However, it provides a number that reflects the fraction of signal events that are expected to be accepted by the whole HLT stage. Another feature of these lines is that they can easily be tuned to a desired output rate if needed by changing the cut on the classifier output.

In addition to study the output rate of these lines, it is necessary to study the average event size, in kbytes, to determine the bandwidth that must be allocated to a given line, measured in kbits/s, which results from multiplying it by the acceptance rate. At the date of this thesis, this number has been measured to be about 5 kbytes for a trigger line with a decay tree containing 3-4 particles, and coincides with the measurements performed directly on the output of the inclusive radiative trigger. Nevertheless, the goal of these lines is to select events containing at least two or

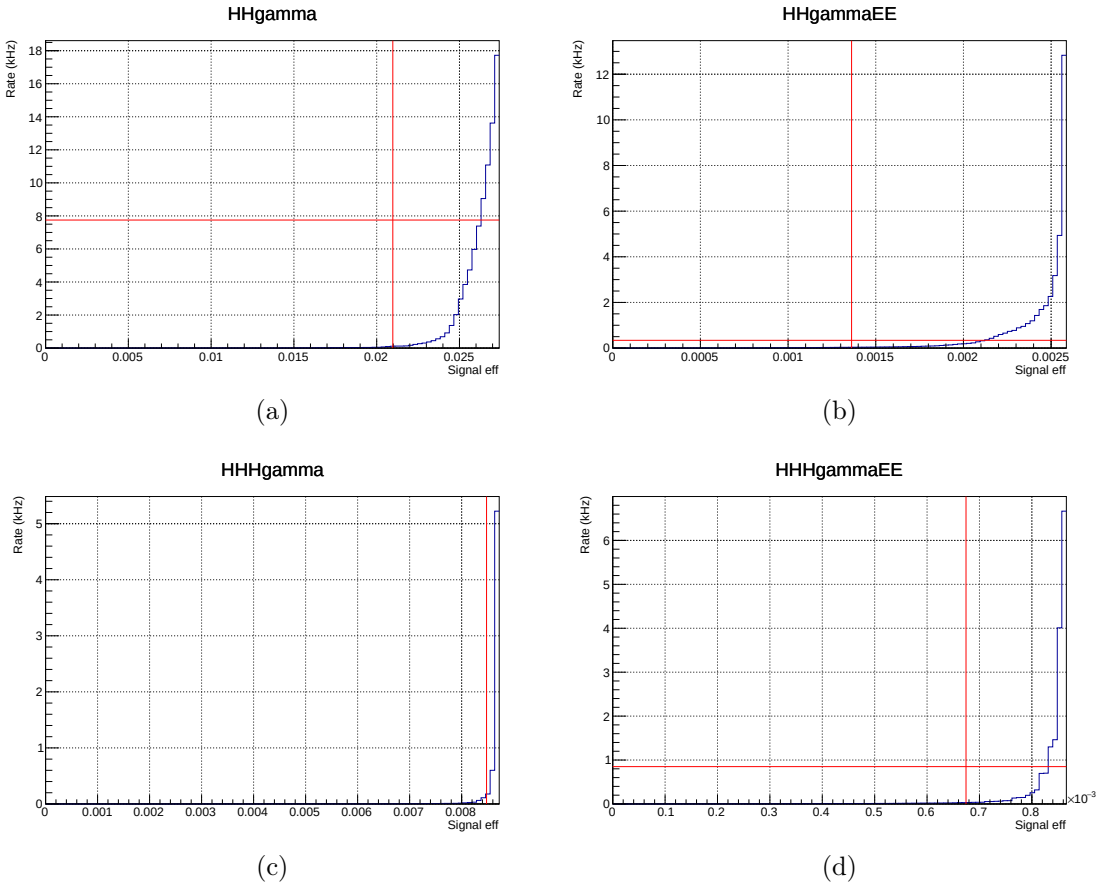

Figure 4.1: Background acceptance rate in terms of the signal efficiency for the new BDTs trained with Run 3 simulation (blue) and each inclusive radiative line: `HHGamma` Figure 4.1a, `HHGammaEE` Figure 4.1b, `HHHGamma` Figure 4.1c and `HHHGammaEE` Figure 4.1d. The intersection of the long red cross marks the performance of the BDT trained with Run 2 data over the same simulated Run 3 samples.

Table 4.5: Efficiencies of the different radiative inclusive lines for different radiative MC samples reproducing Run 3 conditions.

MC sample	$\epsilon_{\texttt{HHGamma}}$ (%)	$\epsilon_{\texttt{HHGammaEE}}$ (%)	$\epsilon_{\texttt{HHHGamma}}$ (%)	$\epsilon_{\texttt{HHHGammaEE}}$ (%)
$B^0 \to K^{*0}\gamma$	2.2	0.2	-	-
$B_s^0 \to \phi\gamma$	3.5	0.2	-	-
$B^+ \to K_1^+(1270)\gamma$	1.4	0.15	0.8	0.1

three hadrons plus an energetic photon, so decays with more particles in the final state must also be saved. These extra particles, even though they do not contribute to the rates, can drastically increase the average event size, so must be handled with care.

As a first approach, we have determined a reasonable cut on the p_{T} and $\chi^2_{\mathrm{IP_{PV}}}$ of the extra particles, if applicable, using the signal $B^0 \to K^{*0}\gamma$ sample, which has a higher efficiency than the minimum bias sample and so it is faster to work with. The resulting cuts are shown in Table 4.6, along the average number of extra particles saved per accepted event by the `HHGamma` line. Another thing to take into account is that the selection for the extra particles does not identify whether that same particle has already been saved by the main selection, meaning that if an average of 3 charged hadrons are being saved, 2 of them are already being included in the main decay tree. This double-counting is not an issue in terms of bandwidth, since the information of the particle is only saved once by the LHCb software. With these cuts, where just a few particles of each type are saved per event, the average event size jumps to $\sim 15\,\mathrm{kbytes}$, three times higher than the initial value. The extra particles saved correspond to background particles included within the sample, showing that a more precise selection is required, using MC samples that contain signal K^0_{S}, Λ or π^0 events to assess that there is not a significant loss of interesting events. This check, however, requires new MC samples to be produced and falls beyond the timescale of this thesis.

Finally, the approach taken when studying the performance of the inclusive radiative trigger lines assumes that these lines, although being constructed in similar ways, have uncorrelated outputs. In fact, this is the worse case scenario, as two lines triggering on the same event would decrease the bandwidth because the information saved is not duplicated. However, studying the correlation serves to know how much additional information the 3-hadron lines are saving on top of the 2-hadron counterparts, in order to decide whether it is worth keeping the 3-hadron lines. We have studied this correlation using the $B^+ \to K_1^+(1270)\gamma$ simulated sample, obtaining that from those events selected by the `HHHGamma` line, around 73% are also being selected by the 2-hadron one, while 76% of the events saved by the 2-hadron line are also saved by the 3-hadron line. All in all, the 3-hadron lines are able to considerably increase the efficiency at which three-hadron decays are saved by a $\sim 25\%$, while utilising a big part of the 2-hadron selection, which justifies them having their own trigger lines.

Table 4.6: Multiplicity (number of particles saved per selected `HHGamma` event) for each type of extra particle, given a preliminary cut in p_{T} and $\chi^2_{\mathrm{IP_{PV}}}$, ran over $B^0 \to K^{*0}\gamma$ simulated events.

Particle	Cut	Multiplicity
$h^{\pm}$	$p_{\mathrm{T}} > 800\,\mathrm{MeV}$ & $\chi^2_{\mathrm{IP_{PV}}} > 8$	5.0
K^0_{S}	$p_{\mathrm{T}} > 500\,\mathrm{MeV}$	0.7
Λ	$p_{\mathrm{T}} > 500\,\mathrm{MeV}$	0.3
γ	$p_{\mathrm{T}} > 1400\,\mathrm{MeV}$	2.5
Merged π^0	$p_{\mathrm{T}} > 2000\,\mathrm{MeV}$	0.8
Resolved π^0	$p_{\mathrm{T}} > 1600\,\mathrm{MeV}$	3

5 Search for $\Lambda_b^0 \to p\pi^-\gamma$ decays at LHCb using Run I data

5.1 Introduction

The decay mode studied in this thesis is $\Lambda_b^0 \to p\pi^-\gamma$, a $b \to d\gamma$ FCNC which is forbidden at tree level in the SM. Therefore, these decays are of interest because NP models can significantly change the properties of the process. For example, a new heavy particle may enter the loop in Figure 2.1 or allow the process to happen at tree-level. This is why a precise measurement of the branching ratio is a powerful probe for NP.

While several branching fractions of FCNC mesonic decays have already been measured, including both $b \to s\gamma$ and $b \to d\gamma$ transitions (Table 5.1), only a single radiative baryonic FCNC branching fraction has been measured up to date, the one from $\Lambda_b^0 \to \Lambda\gamma$ [54], corresponding to a $b \to s\gamma$ process. Such decay has been first observed using LHCb data, thus setting the ground for the search of the $\Lambda_b^0 \to p\pi^-\gamma$ decay mode, despite being Cabibbo-suppressed. Contrary to the Λ, the intermediate n^* resonance is short-lived, and so it can be reconstructed from its decay into $p\pi^-$ using all the information from the tracking system.

Nevertheless, since there is an abundance of n^* resonances (see Table 2.4), it is unclear which ones are favoured in the decay, so we inclusively select $p\pi^-$ pairs with an invariant mass below 2.2 GeV ($c = 1$ is used from this point onward when referring to energy, momentum or masses). This decision has a major drawback: crossfeed contamination from $b \to s\gamma$ radiative modes. Following Equation 2.11, these modes are expected to have a branching fraction ~ 20 times bigger than the

Table 5.1: Known branching fractions of $b \to s\gamma$ and $b \to d\gamma$ decays. The branching fraction of the decay mode $\Lambda_b^0 \to pK^-\gamma$ has not been officially measured yet, but other ongoing analyses point to a value close to $\mathcal{B}(B^0 \to K^{*0}\gamma)$. All the values have been extracted from [21].

Decay ($b \to s\gamma$)	Branching fraction	Decay ($b \to d\gamma$)	Branching fraction
$B^0 \to K^{*0}\gamma$	$(4.33 \pm 0.15) \times 10^{-5}$	$B^0 \to \rho^0\gamma$	$(8.6 \pm 1.5) \times 10^{-7}$
$B_s^0 \to \phi\gamma$	$(3.52 \pm 0.34) \times 10^{-5}$	$\Lambda_b^0 \to p\pi^-\gamma$	?
$B^0 \to K_2^{*0}(1430)\gamma$	$(1.24 \pm 0.24) \times 10^{-5}$		

Table 5.2: List of Λ resonances in the 1440-2200 MeV range with at least a "existence is very likely" status, as in [21].

Particle	Mass (MeV)	J^P
$\Lambda(1520)$	1517.5 ± 0.4	$\left(\frac{3}{2}\right)^-$
$\Lambda(1600)$	1546 ± 6	$\left(\frac{1}{2}\right)^+$
$\Lambda(1670)$	1674 ± 4	$\left(\frac{1}{2}\right)^-$
$\Lambda(1690)$	1690 ± 10	$\left(\frac{3}{2}\right)^-$
$\Lambda(1800)$	1809 ± 9	$\left(\frac{1}{2}\right)^-$
$\Lambda(1810)$	1773 ± 7	$\left(\frac{1}{2}\right)^+$
$\Lambda(1820)$	1818 ± 6	$\left(\frac{5}{2}\right)^+$
$\Lambda(1830)$	1830 ± 30	$\left(\frac{5}{2}\right)^-$
$\Lambda(1890)$	1872 ± 5	$\left(\frac{3}{2}\right)^+$
$\Lambda(2100)$	2040 ± 14	$\left(\frac{7}{2}\right)^-$
$\Lambda(2110)$	2048 ± 10	$\left(\frac{5}{2}\right)^+$

signal mode. Furthermore, they mimic the kinematics of the signal and can only be dealt with by vetoing the mass of the intermediate resonance or by applying PID requirements.

Finally, despite not having been observed yet, the $\Lambda_b^0 \to pK^-\gamma$ process is used as a normalisation channel to cancel out the uncertainty from the cross-section at LHCb, the hadronization factor for a b quark to form a Λ_b^0 and other systematic uncertainties that may occur in both the signal and normalisation modes. As it happens with the signal, several particular Λ^{*0} resonances are reconstructed with the pK^- pair, as there are many to choose from (see Table 5.2) in our working range. Therefore, if evidence of the $\Lambda_b^0 \to p\pi^-\gamma$ is obtained, a value for its branching fraction alone will be obtained once the $\Lambda_b^0 \to pK^-\gamma$ branching ratio is measured, which is the topic of a different analysis at LHCb.

5.2 Data samples

5.2.1 LHCb data samples

The data samples used in this study were collected from pp collisions in the LHCb experiment during 2011 and 2012, at a centre-of-mass energy of $\sqrt{s} = 7\,\text{TeV}$ and $\sqrt{s} = 8\,\text{TeV}$, respectively. The total luminosity recorded these two years was $3.0\,\text{fb}^{-1}$, with $1.0\,\text{fb}^{-1}$ recorded in 2011 and $2.0\,\text{fb}^{-1}$ in 2012. In addition, approximately half of the data was taken with the magnet polarity "up", and the other half with polarity "down", to take care of possible detection asymmetries between positive and negative charged particles. However, the differences between polarities and years are small enough so that both magnet polarities and years are treated together, while assigning a systematic uncertainty due to the differences between 2011 and 2012.

For consistency, the reconstruction configuration used is the same for the whole

Table 5.3: Summary of the simulated samples used in the study. The amount of candidates corresponds to the number of entries in the ntuple, this is, the number of candidates accepted by the `B2XGamma2pi` stripping line, times the multiplicity.

Decay mode	Reconstruction	EvtGen	Candidates
$B^0 \to (K^{*0} \to K^+\pi^-)\gamma$	`Reco14c`	`Sim09b`	807800
$B^0 \to K^+\pi^-\gamma$	`Reco14c`	`Sim09c`	59375
$B^0 \to (\rho^0 \to \pi^+\pi^-)\gamma$	`Reco14a`	`Sim08a`	137865
$B_s^0 \to (\phi \to K^+K^-)\gamma$	`Reco14a`	`Sim08d`	530273
$\Lambda_b^0 \to (\Lambda^0(1520) \to pK^-)\gamma$	`Reco14c`	`Sim09d`	62528
$\Lambda_b^0 \to (\Lambda^0(1670) \to pK^-)\gamma$	`Reco14c`	`Sim09d`	25266
$\Lambda_b^0 \to (\Lambda^0(1820) \to pK^-)\gamma$	`Reco14c`	`Sim09d`	14154
$\Lambda_b^0 \to (\Lambda^0(1830) \to pK^-)\gamma$	`Reco14c`	`Sim09d`	13822
$B^0 \to K_2^{*0}(1430) \to K^+\pi^-\gamma$	`Reco14c`	`Sim09c`	93458
$B^+ \to (K_1^+(1270) \to K^+\pi^-\pi^+)\gamma$	`Reco14a`	`Sim08a`	121500
$B^+ \to (K_1^+(1400) \to K^+\pi^-\pi^+)\gamma$	`Reco14a`	`Sim08a`	37318
$B^+ \to K_2^{*+}(1430) \to K^+\pi^-\pi^+\gamma$	`Reco14a`	`Sim08a`	37296
$B^+ \to (\overline{D}^0 \to K^+\pi^-\pi^0)(\rho^+ \to \pi^+\pi^0)$	`Reco14a`	`Sim08e`	5648
$\Lambda_b^0 \to pK^-\gamma$	`Reco14c`	`Sim09b`	721910
$\Lambda_b^0 \to p\pi^-\gamma$	`Reco14c`	`Sim09d`– `ReDecay01`	383708

data set, which corresponds to `Reco14`. This particular version was used to reprocess the Run 1 data and included improvements in the calibration and alignment of the detector, as well as more tools and algorithms to work with.

5.2.2 Simulation samples

The simulation samples, also called Monte Carlo (MC) samples, used in this analysis reproduce 2012 conditions. The simulated events are all generated using PYTHIA 8 [55] and according to a phase-space model, which are further required to be accepted by the `B2XGamma2pi` stripping line (see subsection 5.3.2). It is important that the simulation samples have been generated with the same software versions, since different versions may introduce biases in the analysis. On the one hand, the reconstruction algorithms all correspond to the same version, labelled as `Reco14`, keeping an homogeneous criteria between 2011 and 2012. `Reco14c` only includes minor fixes with respect to `Reco14a`. On the other hand, the configuration used to generate the *pp* collision and the subsequent decays is done by EvtGen [56]. The target version used in this analysis is `Sim09`, which collects the latest software enhancements developed for Run 2, although `Sim08` has also been used in some other decays without `Sim09` available. These, however, do not play a key role in the analysis in terms of precisely computing efficiencies, but give context and reflect the big similarities among radiative decays, and are only used to extract their mass distributions. Table 5.3 provides a list of the simulation samples and their configurations.

Besides the reconstruction and EvtGen versions, the simulated samples contain

some cuts at the generator stage to prevent saving some events that will be discarded at a later stage. These cuts require the daughter particles to be within the LHCb acceptance, although some samples contain an additional requirement on the transverse momentum of the photon ($\gamma\ p_{\mathrm{T}} > 0.5\,\mathrm{GeV}$), which is further constrained by the stripping line.

The signal MC, corresponding to the $\Lambda_b^0 \to p\pi^-\gamma$ decay, has been generated using ReDecay [57]. The basic concept of this technique is to simulate a full event, take out the signal except for the mother particle, generate a new signal (the decay products of the Λ_b^0) and combine it with the stored underlying event. This technique allows for much faster simulation, at the cost of poorer Λ_b^0 generation, although the effect can be diluted by generating more events.

Furthermore, both the signal and normalisation MC samples have two main flaws when reproducing the real decays. On the one hand, they do not reproduce an intermediate dihadron resonance: the three final-state particles are produced according to a phase-space model. This leads to an important miss-representation of the reconstructed dihadron mass, as well as to a poor modelling of the transverse momentum of the photon. On the other, the transverse momentum of the Λ_b^0 is also known to be poorly reproduced in the simulation, which affects also the daughters particles. To counteract these effects, these samples are reweighted to match the distributions obtained from LHCb data.

Simulation samples reweighting

A reweighting of the signal and normalisation simulation samples is necessary to properly reproduce the dihadron mass and the Λ_b^0 p_{T}, due to the poor theoretical knowledge on the distribution of n^* and Λ^* and the miss-representation of the simulation, respectively. With the phase-space model used in the simulation, the dihadron mass is distributed over a huge range, steadily rising until $m_{p\pi} \approx 3000\,\mathrm{MeV}$, to then decrease until the mass of the Λ_b^0 ($\approx 5620\,\mathrm{MeV}$), within resolution effects, is reached. This distribution is shown in Figure 5.1. Since we are looking for three-body decays of Λ_b^0, which have two degrees of freedom (ignoring the spin), a 2-D reweighting with the dihadron and photon-hadron mass is necessary to fully describe the kinematics of the process. However, the reference data sample used to model the dihadron mass contains a J/ψ instead of a γ. Such huge mass difference means that the photon-hadron mass cannot be reproduced properly, so only the dihadron mass is used. We show that reweighting with this variable alone is enough to properly model all the relevant dihadron mass distributions, which are the most relevant for this analysis.

Despite the phase-space model avoids specifying the intermediate resonance of the decay chain, it provides a dihadron mass distributed over the $m_p + m_\pi < m_{p\pi} < m_{\Lambda_b^0} - m_\gamma$ range for the signal, and over the $m_p + m_K < m_{pK} < m_{\Lambda_b^0} - m_\gamma$ range for the normalisation mode. Most of the events, however, happen to fall below the $m_{p\pi} = 2200\,\mathrm{MeV}$ upper limit, which is where most of the n^* and Λ^{*0} resonances are found. This can be seen in Figure 5.4 and Figure 5.5, where the reference data and the MC samples are compared.

In addition, we take into account that the reweighting is performed after the stripping selection, so that the efficiencies computed beforehand need to be corrected. This is illustrated in Figure 5.1c, where the distribution of the dihadron mass after stripping is divided by the distribution generated. The division shows that the stripping efficiency remains approximately constant for our working range of $m_{p\pi^-} < 2200\,\text{MeV}$, then slowly raises to a factor 1.2 around 3500 MeV, to finally meet a steady drop as the mass increases.

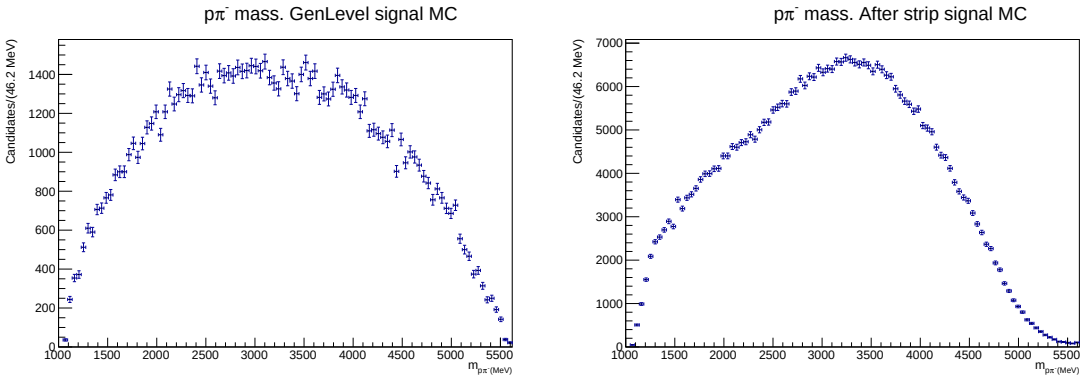

(a) (b)

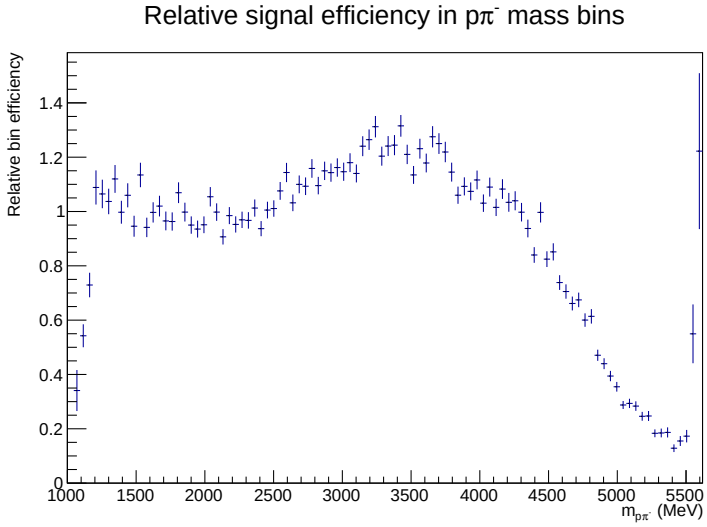

(c)

Figure 5.1: $p\pi^-$ mass distributions for the signal MC at generator level (a) and after the stripping has been applied (b). The division of the latter over the former, with both normalised to 1, provides the relative efficiency per mass bin (c).

Independent data samples are used to serve as reference for the reweighting of the signal and normalisation MC. For the signal mode, the data selected to search for the $\Lambda_b^0 \to p\pi^- J/\psi$ decay [58] has been chosen to reweight the dihadron mass, which also analyses the whole Run 1 data. For the normalisation mode, we have chosen the study of a pentaquark using the $\Lambda_b^0 \to pK^- J/\psi$ decay [28] for the dihadron mass, also employing Run 1 data. As for the modelling of the Λ_b^0

p_{T}, in both cases the $\Lambda_b^0 \to pK^-J/\psi$ data is used as reference, since it provides a substantially larger amount of events than the $\Lambda_b^0 \to p\pi^-J/\psi$ data. This means that the $\Lambda_b^0 \to p\pi^-\gamma$ simulation undergoes two 1-D reweightings, which can be done because of the low correlation between the Λ_b^0 p_{T} and the dihadron mass; while the $\Lambda_b^0 \to pK^-\gamma$ MC undergoes a single 2-D reweighting. We employ the *sPlot* [59] technique to extract the signal distribution from the background. As mentioned earlier, the effect of having a J/ψ in the decay chain instead of a γ is reflected in the dihadron mass distributions, that are now capped at $m_{\Lambda_b^0} - m_{J/\psi} \approx 2523\,\mathrm{MeV}$. Using this distribution as reference results in removing all simulated signal events above that value, which, in principle, are allowed kinematically when there is a γ in the decay chain. Nevertheless, the main n^* and Λ^* resonances are located safely below this limit, and the *sWeighted* data show only few events with mass above our working limit of $m_{p\pi} < 2200\,\mathrm{MeV}$. This means that, for this analysis, the *sWeighted* reference samples properly reproduce the expected dihadron mass distributions of both the signal and normalisation modes.

In order to apply the *sPlot* technique, we must model the Λ_b^0 mass. In the $\Lambda_b^0 \to p\pi^-J/\psi$ analysis it is described using three components:

- A double-sided Crystal Ball function [60] for the signal.
- An exponential function to describe the combinatorial background.
- A custom histogram distribution, with free yield, to account for the miss-identified $\Lambda_b^0 \to pK^-J/\psi$ background.

For the sake of simplicity, the fit used in this analysis to extract the signal only uses a gaussian and an exponential distribution. The first accounting for the signal and the second for the combinatorial background, while ignoring the small contribution arising from the miss-identified background. This contribution is important in the original fit in order to count the number of signal events as precisely as possible. In our case, we are only interested in extracting the $m_{p\pi}$ distribution of the signal component, for which the number of signal events found has little effect. As in the $\Lambda_b^0 \to p\pi^-J/\psi$ analysis, the parameters are determined through an unbinned maximum likelihood fit to the data. The comparison in Figure 5.2 between the original and the simplified model shows that the latter also correctly describes the data.

On the other hand, the $\Lambda_b^0 \to pK^-J/\psi$ mode is modelled as in the original analysis, with an added requirement on the J/ψ p_{T} to be above 2 GeV to match the requirement of the radiative stripping line Table 5.7:

- A gaussian core with exponential tails to describe the signal.
- An exponential function to describe the combinatorial background.

The signal is clear enough so that all parameters can be left free in the fit. As in the $\Lambda_b^0 \to pK^-J/\psi$ analysis, the parameters are determined through an unbinned maximum likelihood fit to the data. The comparison in Figure 5.3 between the original and the simplified model show that the fit is properly reproduced.

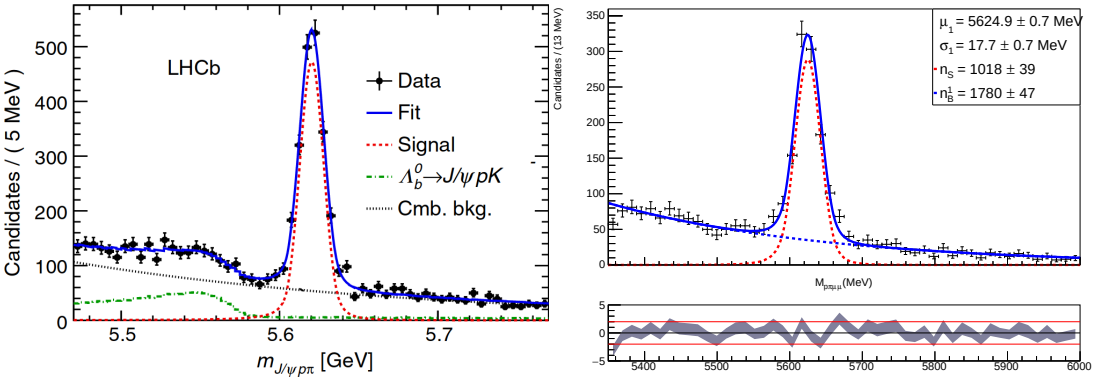

(a) (b)

Figure 5.2: Comparison of the $p\pi^-\mu^+\mu^-$ mass fits done in the original analysis (a) and in this one (b).

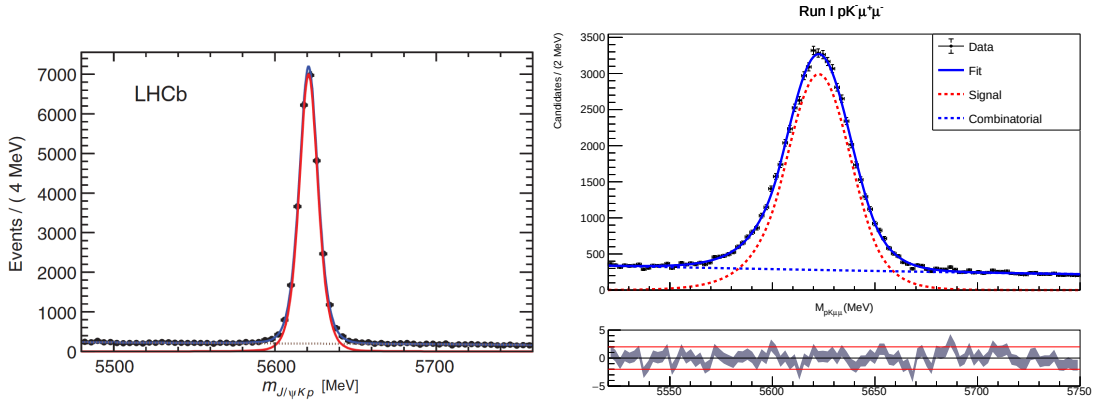

(a) (b)

Figure 5.3: Comparison of the $pK^-\mu^+\mu^-$ mass fits done in the original analysis (a) and in this one (b).

Once the fits have been performed, each signal component is extracted by using the *sPlot* technique independently, assigning an *sWeight* to each candidate in the $\Lambda_b^0 \to p\pi^- J/\psi$ ($\Lambda_b^0 \to pK^- J/\psi$) data samples. Then, the Λ_b^0 p_{T} and $m_{p\pi^-}$ (m_{pK^-}) variables of the signal (normalisation) MC are reweighted in order to match the *sWeighted* distribution that has just been obtained. For the signal, 25 equally populated bins are used for the dihadron mass, while 100 are used for the Λ_b^0 p_{T}. For the normalisation, 25 equally populated bins are used for each variable, for a total of 625 2-D bins.

Figure 5.4 and Figure 5.5 show the change of the $p\pi^-$ and pK^- mass, respectively, and the Λ_b^0 p_{T}. The rest of the mass hypotheses, which are compared in section A.2, show how the reweighted distributions are much better matched to the reference than the unweighted ones. This proves that reweighting on these variables is able to fix the main misrepresentations of the simulation.

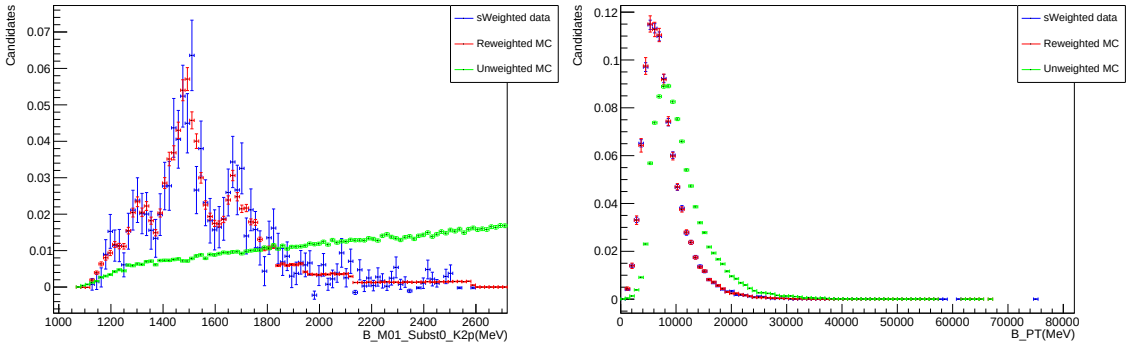

(a) (b)

Figure 5.4: Comparison of the $p\pi$ mass (a) and Λ_b^0 p_{T} (b) distributions between *sWeighted* data (blue) and the signal MC, both unweighted (green) and reweighted (red). *sWeighted* $\Lambda_b^0 \to p\pi^- J/\psi$ data is used in (a) and *sWeighted* $\Lambda_b^0 \to pK^- J/\psi$ data is used in (b).

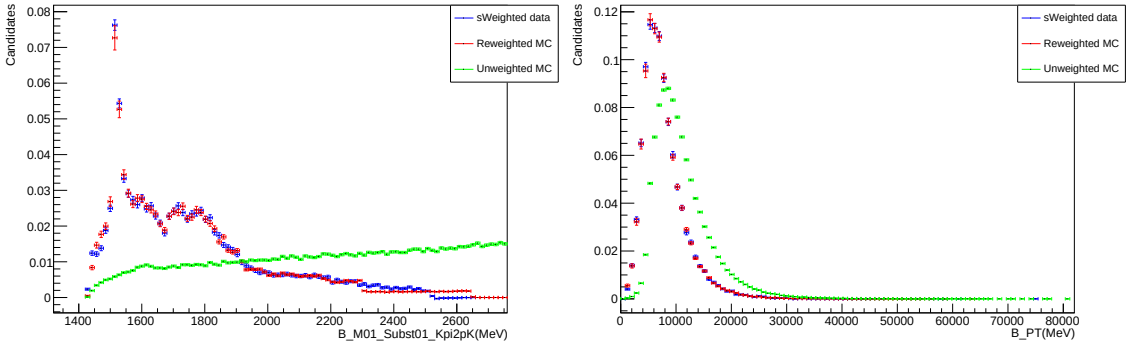

(a) (b)

Figure 5.5: Comparison of the pK mass (a) and Λ_b^0 p_{T} (b) distributions between *sWeighted* $\Lambda_b^0 \to pK^- J/\psi$ data (blue) and the signal MC, both unweighted (green) and reweighted (red).

5.3 Event selection

After the samples to be used in this analysis have been decided, a selection must be developed to extract the underlying signal from the huge bulk of LHCb data. This is done through a series of requirements starting with the trigger and stripping lines, which serve a more general purpose, and finishing with the kinematic, mass vetoes and PID requirements, which are tuned for the particular signal mode under search.

5.3.1 Trigger selection

As described in section 3.2, the trigger system is divided in three stages: L0, HLT1 and HLT2. For an event to be selected in this analysis, it must match the requirements from Table 5.4. Furthermore, the event must be Triggered On Signal (TOS), meaning that the main $\Lambda_b^0 \to p\pi^-\gamma$ candidate alone satisfies the trigger requirements, without needing any the particles that form the rest of the event. Therefore, the events that pass a trigger selection fall into two other categories, namely TIS (Trigger Independent on Signal) and TOB (Trigger On Both), depending on whether the remaining of the event alone is enough to trigger a positive response or both the event and the underlying event are required to trigger the positive response.

For the L0 stage, three different lines have been employed. The `L0Photon` and `L0Electron` are the most important lines, since they are used to select events containing a highly-energetic photon, a key signature in radiative decays. The `L0Electron` in particular catches photon converted into electrons in the electromagnetic cascade. The `L0Hadron` line complements these two by adding events with highly-energetic hadrons. It has been checked that the inclusion of this line does not dilute the presence of radiative events in data.

For the HLT1 stage, the `Hlt1TrackAllL0` line is able to select events containing a track with large transverse momentum and large Impact Parameter χ^2 (IPCHI2), meaning that the tracks must not have originated in the PV. This is a key signature of b-hadron decays. The `Hlt1TrackPhoton` line allows to complement the selection, since it allows to loosen the track requirements by demanding, in turn, an event with a high p_{T} photon.

For HLT2 three lines were used, as the inclusive radiative lines described in chapter 4 was first implemented for Run 2. The `Hlt2RadiativeTopoPhoton` and `Hlt2RadiativeTopoTrack` lines both focus on selecting events with two tracks and a photon, the former focusing on a harder photon and softer tracks, while the latter aims for softer photons but harder tracks. The `Hlt2Topo2BodyBBDT` only looks for pairs of hadrons using multivariate techniques, and is included to further increase the efficiency selecting our signal mode.

Trigger efficiency

The trigger efficiency, which corresponds to the joint L0, HLT1 and HLT2 efficiencies is measured from the MC. Nevertheless, it is possible to retrieve the trigger efficiency

Table 5.4: List of trigger lines used in the study, accepting only TOS events. Events are required to pass at least one L0, one HLT1, and one HLT2 line.

Trigger line
`L0Photon`
`L0Electron`
`L0Hadron`
`Hlt1TrackAllL0`
`Hlt1TrackPhoton`
`Hlt2RadiativeTopoPhoton`
`Hlt2Topo2BodyBBDT`
`Hlt2RadiativeTopoTrack`

Table 5.5: PID requirements used in the selection prior to the TISTOS method.

Decay mode	Particle	Requirement
$B^0 \to K^{*0}\gamma$	K	$ProbNNk(1-ProbNNp)(1-ProbNNpi) > 0.3$
	π	$ProbNNpi(1-ProbNNk)(1-ProbNNp) > 0.4$
$\Lambda_b^0 \to pK^-\gamma$	p	$ProbNNp(1-ProbNNk)(1-ProbNNpi) > 0.3$
	K	$ProbNNk(1-ProbNNp)(1-ProbNNp) > 0.4$

from data using the TISTOS method [61] as a means to cross-check the result from the simulation. In the TISTOS method, the trigger efficiency, measured after a certain preliminary selection, relies on the assumption that the TIS and TOS selections used in it are independent, and so that $\epsilon_{TIS} = \epsilon_{TIS|TOS}$ holds. This assumption, however, is not entirely true since the trigger selections are mainly based on the transverse momentum and impact parameter of the mother B particle. However, there is no need to bin the phase-space of the Λ_b^0 in this analysis because the same bias occurs in both the signal and normalisation modes, and so it will cancel in the ratio. The trigger efficiency from data is then computed as:

$$\epsilon_{Trig} = \frac{N_{Trig}}{N_{TIS}} \frac{N_{TIS\&TOS}}{N_{TOS}} \tag{5.1}$$

Which, for this analysis where the trigger selection corresponds to a TOS selection, simplifies to:

$$\epsilon_{Trig} = \frac{N_{TIS\&TOS}}{N_{TIS}} \tag{5.2}$$

In order to get the number of TIS and TIS&TOS events from data, we use $B^0 \to K^{*0}\gamma$ and $\Lambda_b^0 \to pK^-\gamma$ events obtained from fits to data following the selection developed in the analysis, but removing the mass vetoes described in subsection 5.3.4 and the trigger requirements from Table 5.4, while applying particular PID requirements shown in Table 5.5.

The trigger efficiency is then obtained in three steps, one for each trigger stage:

Table 5.6: Trigger efficiencies computed in MC and in data, the latter using the TISTOS method, as well as the correction factor for the two control modes used.

Decay mode	$B^0 \to K^{*0}\gamma$	$\Lambda_b^0 \to pK^-\gamma$
$\epsilon_{Trig}(MC)$	0.5581 ± 0.0015	0.740 ± 0.006
$\epsilon_{Trig}(Data)$	0.51 ± 0.03	0.65 ± 0.07
f_{Trig}	0.92 ± 0.05	0.88 ± 0.09

1. The efficiency of the HLT2 stage $\epsilon(HLT2)$ is obtained from MC because it is properly reproduced in the simulation and to reduce the uncertainty that would come out of TISTOS method in this stage due to low number of HLT2 TIS events present.

2. The TISTOS method is done on the HLT1 stage, with no particular selection for L0 and applying the TOS requirements from Table 5.4 into HLT2, using `HLT1Phys` for the TIS selection. $\epsilon(HLT1|HLT2)$ is obtained from it.

3. The TISTOS method is done on the L0 stage, using the TOS requirements from Table 5.4 in HLT1 and HLT2 and `L0Global` for the TIS selection. This allows to obtain $\epsilon(L0|HLT1 \cap HLT2)$.

Multiplying these three efficiencies one obtains the trigger efficiency from data:

$$\epsilon_{Trig} = \epsilon(HLT2)\epsilon(HLT1|HLT2)\epsilon(L0|HLT1 \cap HLT2) \tag{5.3}$$

Which is compared to the efficiency obtained from the simulation in Table 5.6 by computing the trigger efficiency correction factor:

$$f_{trigger} = \frac{\epsilon_{Trig}(data)}{\epsilon_{Trig}(MC)} \tag{5.4}$$

The correction factors show that the MC slightly overestimates the trigger efficiency. However, this correction is shared among two different radiative processes such as $B^0 \to K^{*0}\gamma$ and $\Lambda_b^0 \to pK^-\gamma$, and so the signal mode, being so similar to the normalisation mode, will also have the same correction factor, thus vanishing in the Branching Ratio up to minor secondary effects. Therefore, no systematic uncertainty is assessed.

5.3.2 Stripping selection

The next step in the selection is the choice of a stripping line to be used to reconstruct the signal and normalisation modes. A stripping line is a standardised selection developed within LHCb that aims to reconstruct a particular decay or set of decays. For the case being, there are no dedicated stripping lines that aim exclusively at reconstructing $\Lambda_b^0 \to p\pi^-\gamma$ or $\Lambda_b^0 \to pK^-\gamma$ decays, so we have used a stripping line that selects $h^+h^-\gamma$ final states in an inclusive fashion. This line is called `B2XGamma2pi` and reconstructs $h^+h^-\gamma$ events that pass the requirements in Table 5.7.

Since this stripping line is inclusive, it does not restrict the dihadron mass nor ask for any PID requirements on the reconstructed hadrons, which are hypothesised to have the mass of a pion during the reconstruction. However, the hadron composition of the signal mode is different, which means that a change in the mass hypothesis must be done to properly reconstruct it. In particular, one of the hadrons is given the mass of the proton, while the other remains with the pion mass.

This change in mass hypothesis is important because now for each event selected by this stripping line, two possible candidates are saved: one where the positive hadron is given the mass of the proton, with the negative hadron having the mass of the pion, and vice versa. At this stage we are unable to tell which of the combinations is better, but the duplication will be taken care of by the PID selection, which will actually require the particles to match their mass hypothesis, thus favouring one of the two possible cases in front of the other.

In the MC samples, where the true ID of the candidates generated is matched, we operate differently depending on the type of final state, in order to properly accommodate the different mass hypothesis cases:

- $h_1h_2\gamma$ ($h_1 \neq h_2$): Each sample is split in its main and reflection (Ref) components by requiring the true ID of the particles. The main part is chosen as the ID combination closest to the signal, while the other combination is labelled as reflection. Taking this analysis as an example, $p\pi$ is searched for, so the main component of the $B^0 \to (K^{*0} \to K^+\pi^-)\gamma$ MC is $K\pi$, while the reflection is πK.

- $hh\gamma$: For this particular case, the main and reflection components are equivalent, so both components are taken as one, as the same would happen on data, doubling the number of candidates. For instance, the $B_s^0 \to (\phi \to K^+K^-)\gamma$ true IDs of the hadrons are simply required to be kaons.

- Other: In any other case, the hadrons are only required to match one of the possible true IDs of its final state. For example, in $B^+ \to (K_1^+(1270) \to K^+\pi^-\pi^+)\gamma$ MC, the hadrons are required to be either a pion or a kaon, without splitting the sample in main and reflection components.

Matching the MC particles with their true IDs is not 100% efficient, so these efficiencies are included in the reconstruction. The efficiencies regarding the stripping, trigger and reconstruction are shown in Table 5.8, together with the whole efficiency up to this point (acceptance+trigger+reconstruction+stripping). The latter efficiency illustrates that all the $hh\gamma$ channels have similar efficiencies, independently of the generator level cuts applied, with a tendency to drop as the mass of the resonance increases. As we have explained, it is after the stripping selection when the reflection component appears, so the efficiencies at Table 5.8 for the reflections are the same as the main event ones.

Table 5.7: Selection requirements of `B2XGamma2pi` stripping line. If the cut is applied to the combination of the daughter particles, rather on the mother particle resulting from the vertex fit, (comb) is specified.

Variable	Selection
π χ^2_{track}/ndf	< 3
π track ghost prob.	< 0.4
π p_{T}	$> 300\,\text{MeV}$
π p	$> 1\,\text{GeV}$
$\min(\pi\ \chi^2_{\text{IP}})$	> 16
m_{ρ^0}	$< 7.9\,\text{GeV}$
ρ^0 $\sum \lVert p_{\text{T}} \rVert$ (comb)	$> 1.5\,\text{GeV}$
ρ^0 χ^2_{vtx}/ndf	< 10
γ p_{T}	$> 2\,\text{GeV}$
γ CL	> 0
m_{B^0}	$3.28\,\text{GeV} < m < 9\,\text{GeV}$
B^0 $\sum \lVert p_{\text{T}} \rVert$ (comb)	$> 5\,\text{GeV}$
B^0 p_{T}	$> 1\,\text{GeV}$
B^0 p	$> 5\,\text{GeV}$
B^0 χ^2_{track}/ndf	< 2.5
B^0 χ^2_{vtx}/ndf	< 9
B^0 χ^2_{IP}	< 9
$\min(B^0\ \chi^2_{\text{IP}})$	> 16
$\min(B^0\ \text{IP}_{\text{PV}})$	$> 0.1\,\text{mm}$

Table 5.8: Summary of the stripping related efficiencies of the considered decay channels. The reflection components, by definition, have the exact same efficiencies as their main counterparts. The $\Lambda_b^0 \to \Lambda^{*0}\gamma$ efficiencies are not shown, again, because the generator level efficiencies used to compute the acceptance were lost.

Decay mode	$\epsilon_{R+T+S}(\cdot 10^{-2})$	$\epsilon_{A+R+T+S}(\cdot 10^{-2})$
$B^0 \to (K^{*0} \to K^+\pi^-)\gamma$	1.73	0.361
$B^0 \to (\rho^0 \to \pi^+\pi^-)\gamma$	2.72	0.560
$B_s^0 \to (\phi \to K^+K^-)\gamma$	2.62	0.616
$\Lambda_b^0 \to (\Lambda^0(1520) \to pK^-)\gamma$	1.37	-
$\Lambda_b^0 \to (\Lambda^0(1670) \to pK^-)\gamma$	1.37	-
$\Lambda_b^0 \to (\Lambda^0(1820) \to pK^-)\gamma$	0.879	-
$\Lambda_b^0 \to (\Lambda^0(1830) \to pK^-)\gamma$	0.879	-
$B^0 \to K_2^{*0}(1430) \to K^+\pi^-\gamma$	1.77	0.367
$B^+ \to (K_1^+(1270) \to K^+\pi^-\pi^+)\gamma$	1.036	0.200
$B^+ \to (K_1^+(1400) \to K^+\pi^-\pi^+)\gamma$	0.947	0.180
$B^+ \to K_2^{*+}(1430) \to K^+\pi^-\pi^+\gamma$	0.919	0.173
$B^+ \to (\overline{D}^0 \to K^+\pi^-\pi^0)(\rho^+ \to \pi^+\pi^0)$	0.139	0.020
$\Lambda_b^0 \to pK^-\gamma$	1.87	0.315
$\Lambda_b^0 \to p\pi^-\gamma$	1.94	0.319

5.3.3 Kinematic selection

This is the first step of the offline selection, with the goal to separate the combinatorial background from signal-like events as much as possible, making use of the kinematic features of the signal decay. This kinematic selection is divided in two smaller steps: a loose preselection and a tighter multivariate selection, driven by a Boosted Decision Tree (BDT).

Offline preselection

A loose selection is applied on both data and simulation to suppress regions of the data sample widely dominated by combinatorial background, and to subtract events with unphysical values. This way, the following BDT can focus in other regions of the data where the separation between background and signal is not so clear.

In this sense, the variables used to perform the preselection on are the same used to train the BDT, except for the γ Confidence Level (CL) and the γ transverse momentum (p_{T}). The former is known to be poorly represented in MC for values very close to 1, so only a loose linear cut is applied to avoid biases. The latter cut is applied to reduce differences between 2011 and 2012 datasets. Apart from selecting signal events, other radiative decays are also selected in the process, as they share the same kinematic features. A summary with the selection and the efficiencies can be found in Table 5.9 and Table 5.11.

Table 5.9: Offline preselection requirements.

Variable	Selection
B^0 Direction Angle	> 0.9999
γ CL	> 0.8
γ p_{T} (MeV)	> 3000
$B^0 p_{\mathrm{T}}$ (MeV)	$3000 < B^0 p_{\mathrm{T}} < 30000$
B^0 Flight Distance (mm)	< 80
$m_{p\pi}$ (MeV)	< 2200
$\pi\chi^2_{\mathrm{IP}}$	< 10000
$p\mathrm{IP}_{\mathrm{PV}}$ (mm)	< 3

Kinematic BDT

After taking care of a small part of the combinatorial background, a BDT is trained using just a collection of kinematic variables. This BDT is designed to further separate combinatorial background and signal (and other radiative decays), taking both data mass sidebands as background proxy and the $\Lambda_b^0 \to p\pi^-\gamma$ simulated sample as signal proxy. The data sidebands correspond to the range $m_{p\pi}(\,\text{GeV}) \in]4.6, 5.2[\cup]6.0, 6.6[$. The BDT has been configured using TMVA [62], where the samples are split in two halves, one for training and one for testing, generating 400 trees with a maximum depth of 2. The list of variables used to train and test the BDT is presented in Table 5.10, and their distributions in signal and background in Figure 5.6.

Once the BDT has been trained, the whole dataset, together with all the MC samples being considered are processed with it. Each candidate is given a value between -1 and 1, where -1 (1) denotes a candidate to be classified as background (signal). The cut on BDT is taken as the value which maximises the signal significance, explored using:

$$FOM = \frac{\epsilon_S}{\sqrt{D}} \tag{5.5}$$

Where ϵ_S is the efficiency on the reweighted signal sample, evaluated on MC and D is the number of data candidates within the 4600-6600 MeV Λ_b^0 mass window, which by definition corresponds to the number of signal plus background candidates. Therefore, maximising this figure of merit is equivalent to maximising the signal significance $\frac{S}{\sqrt{S+B}}$. This choice is done to avoid manually counting every single peaking contribution and assuming a Branching Fraction for the signal mode.

The output of the classifier, along the figure of merit distribution, are shown in Figure 5.7. There is good match between the training and testing samples, with the Kolmogorov-Smirnov test yielding a value safely above the 0.05 threshold that would indicate overtraining. This means that the classifier behaves similarly with the training and testing samples, and that it has not learned the statistical fluctuations of the testing sample. The optimal cut has been found to be BDT response > 0.095992.

Table 5.10: Variables used for training the kinematic BDT.

#	Variable
1	B^0 Flight Distance (mm)
2	$B^0 p_{\mathrm{T}}$ (GeV)
3	$\log(1 - B^0$ Direction Angle)
4	γ_η
5	B^0 χ^2_{PV}
6	B^0 χ^2_{EV}
7	$\log(B^0 \chi^2_{\mathrm{IP_{PV}}})$
8	$\log(n^* \chi^2_{\mathrm{IP_{PV}}})$
9	$n^* p_{\mathrm{T}}$ (GeV)

The efficiency of this selection on each of the considered decay modes (Table 5.11) again shows how the radiative channels share similar kinematics.

In order to confirm the correct behaviour of the BDT, first we have checked that the variables used in the BDT are properly reproduced in the MC by comparing $\Lambda_b^0 \to pK^-\gamma$ in MC and *sWeighted* data, both selected with the selection developed in the analysis, except for the BDT and the mass vetoes, which have not been applied, and the PID selection, for which we have used the one shown in Table 5.5. Figure 5.8 shows the comparison of the BDT response between the data and the MC, showing a good agreement after the reweighting of the simulation sample. The comparison of the variables used to train the BDT can be found at section A.3, in which a small disagreement in the Λ^{*0} p_{T} variable is observed after the reweighting. However, no further action is taken as the only variable used in the event selection, and thus to calculate efficiencies, is the BDT response, which is properly reproduced.

Furthermore, we have made sure that the classifier is not producing an artificial peak around the mass of the Λ_b^0, which would be a clear sign that the BDT is learning it through the input variables. To do so, we have computed the efficiency of the optimised cut in bins of the Λ_b^0 mass, both in the data sidebands using data and in the signal region, using MC. The result, seen in Figure 5.9, shows a flat efficiency distribution for the mass sidebands, while the signal region remains nearly flat except for the bins furthest away from the Λ_b^0 mass ($\approx 5620\,\mathrm{MeV}$). These events are associated with poorly reconstructed events in the simulation, and thus tend to have a higher direction angle or a worse vertex reconstruction. With these results, we consider that the BDT does not create an artificial peak.

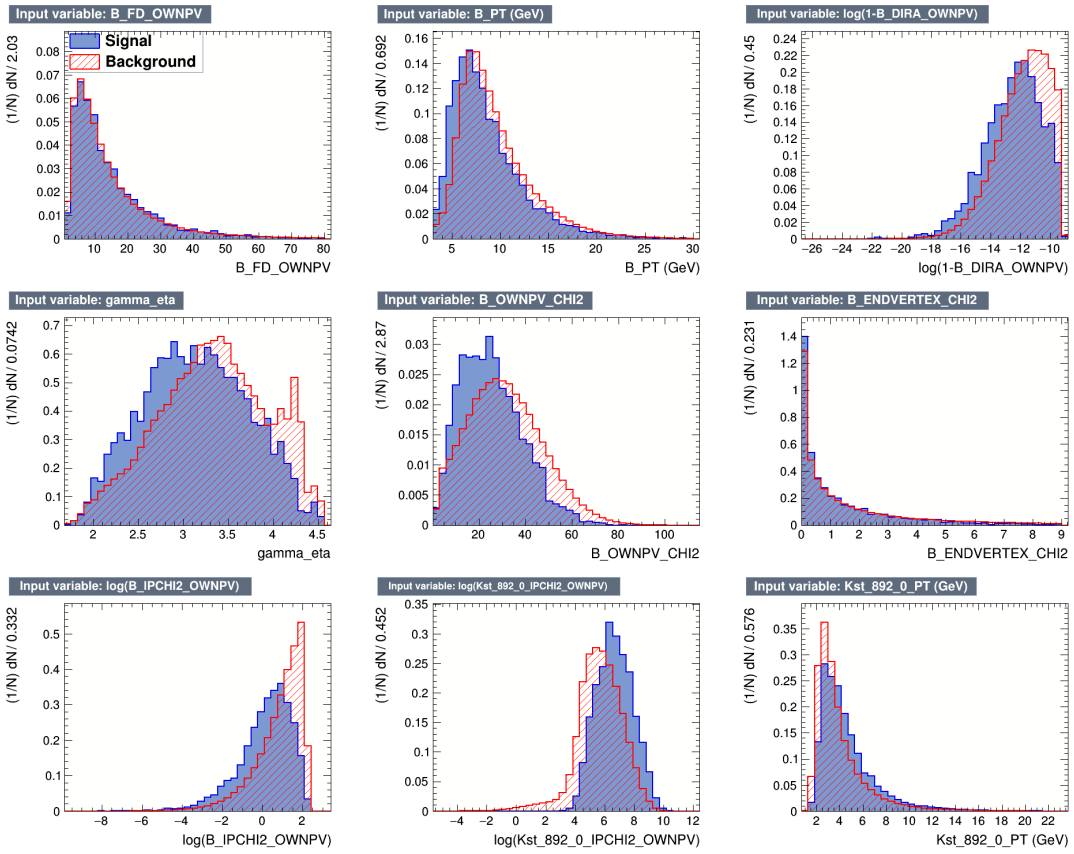

Figure 5.6: Distributions of the variables used to train the kinematic BDT, comparing signal and background proxies.

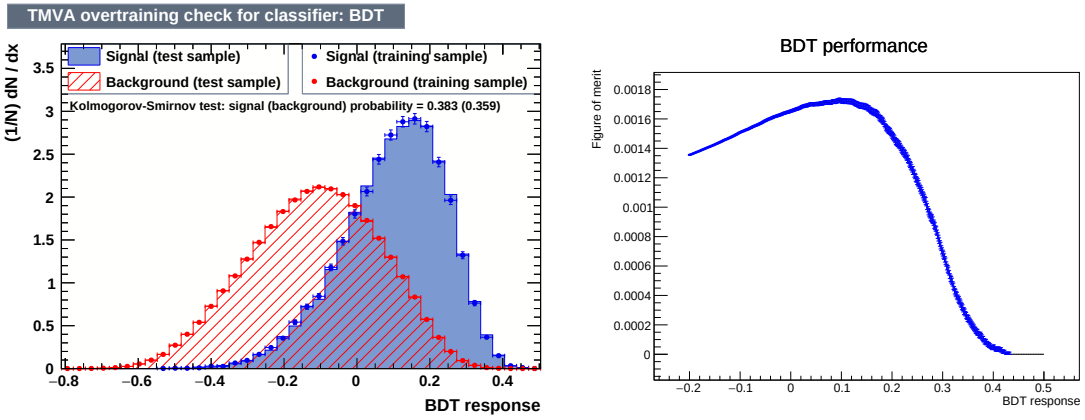

(a) (b)

Figure 5.7: Distribution of the kinematic BDT response (a) and figure of merit as a function of the minimal BDT response required (b). A Kolmogorov-Smirnov test has been performed to compare training and testing samples, showing no overtraining.

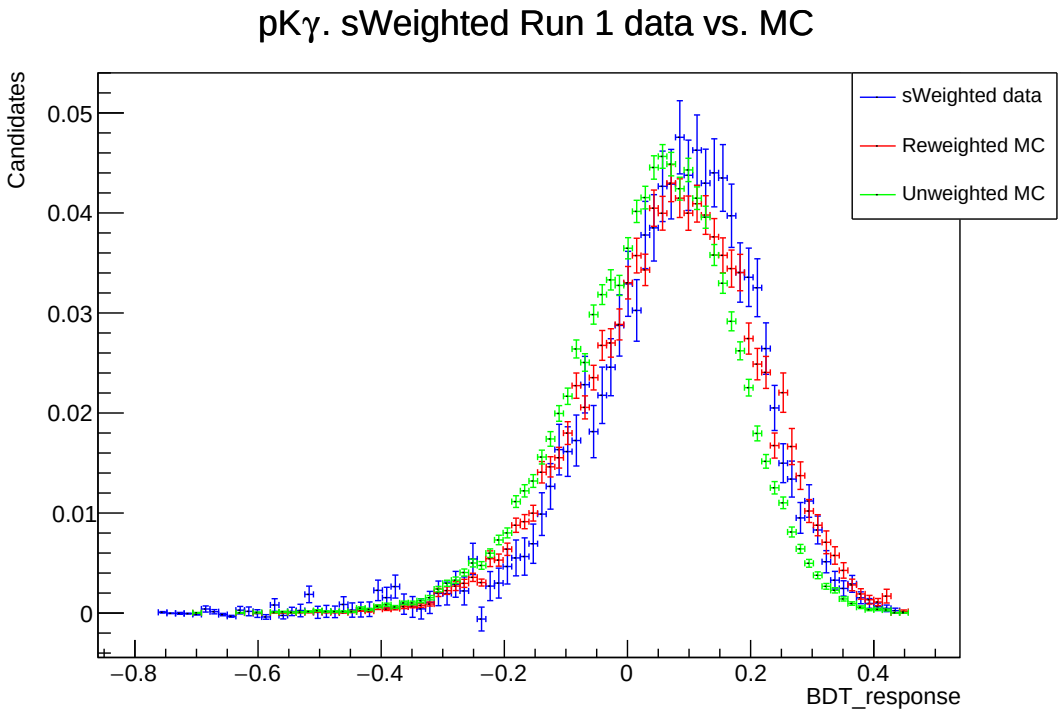

Figure 5.8: Comparison of the kinematic BDT response of the *sWeighted* $\Lambda_b^0 \to pK^-\gamma$ data (blue), unweighted (green) and reweighted (red) $\Lambda_b^0 \to pK^-\gamma$ MC.

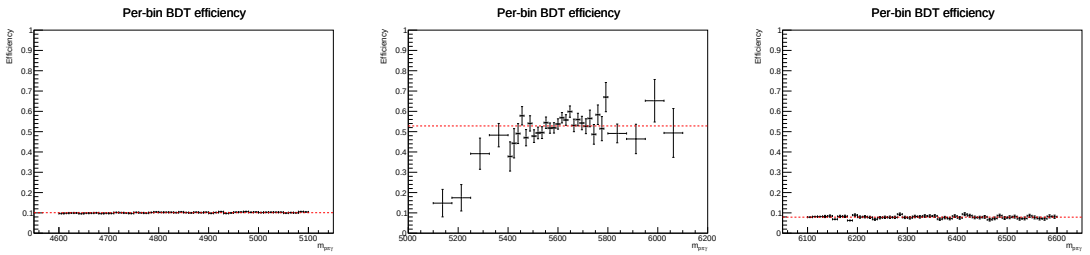

(a) (b) (c)

Figure 5.9: Efficiency of the optimised BDT cut for different bins of the Λ_b^0 mass in the low-mass sideband (a), signal region (b) and high-mass sideband (c). The red dashed line marks the average efficiency.

Table 5.11: Summary of the kinematic efficiencies of the considered decay channels.

Decay mode	ϵ_{presel}	ϵ_{BDT}
$B^0 \to K^{*0}\gamma$	0.650	0.435
$B^0 \to K^{*0}\gamma$ Ref	0.582	0.436
$B^0 \to \rho^0\gamma$	0.648	0.458
$B_s^0 \to \phi\gamma$	0.621	0.514
$\Lambda_b^0 \to \Lambda^0(1520)\gamma$	0.657	0.491
$\Lambda_b^0 \to \Lambda^0(1520)\gamma$ Ref	0.648	0.491
$\Lambda_b^0 \to \Lambda^0(1670)\gamma$	0.675	0.460
$\Lambda_b^0 \to \Lambda^0(1670)\gamma$ Ref	0.618	0.461
$\Lambda_b^0 \to \Lambda^0(1820)\gamma$	0.663	0.432
$\Lambda_b^0 \to \Lambda^0(1820)\gamma$ Ref	0.572	0.436
$\Lambda_b^0 \to \Lambda^0(1830)\gamma$	0.661	0.413
$\Lambda_b^0 \to \Lambda^0(1830)\gamma$ Ref	0.560	0.417
$B^0 \to K_2^{*0}(1430)\gamma$	0.573	0.365
$B^0 \to K_2^{*0}(1430)\gamma$ Ref	0.520	0.366
$B^+ \to K_1^+(1270)\gamma$	0.398	0.245
$B^+ \to K_1^+(1400)\gamma$	0.393	0.243
$B^+ \to K_2^{*+}(1430)\gamma$	0.385	0.243
$B^+ \to \overline{D}^0\rho^+$	0.156	0.167
$\Lambda_b^0 \to pK^-\gamma$	0.637	0.442
$\Lambda_b^0 \to pK^-\gamma$ Ref	0.570	0.444
$\Lambda_b^0 \to p\pi^-\gamma$	0.637	0.522

5.3.4 Mass vetoes

The selection up to this point is able to select decays with two hadrons and a photon in the final state, inclusively. It is necessary now to suppress peaking backgrounds over the signal mode. The first step to do so is to suppress $b \to s\gamma$ modes, namely $\Lambda_b^0 \to \Lambda^{*0}\gamma$, $B^0 \to K^{*0}\gamma$ and $B_s^0 \to \phi\gamma$, by imposing vetoes on the hh invariant mass. More vetoes are imposed in the J/ψ and D^0 masses, which contribute to the combinatorial background after being combined with a random photon.

For convenience, when talking about some dihadron mass $m_{h_1h_2}$, $h_1(h_2)$ refers to the mass hypothesis given to the first (second) hadron. For this analysis, we have chosen to look for a proton as the first hadron and a pion as the second. A detailed description of the vetoes is as follows:

- ϕ veto: $m_{KK} < 1060\,\text{MeV}$ is excluded to significantly reduce the number of $B_s^0 \to \phi\gamma$ events in data. This veto has low impact on the signal, as the ϕ makes a narrow resonance in the lower-mass extreme of the phase-space.
- K^{*0} veto: $820\,\text{MeV} < m_{K\pi} < 980\,\text{MeV}$ and $820\,\text{MeV} < m_{\pi K} < 980\,\text{MeV}$ regions are excluded. This is a considerably important veto, as it is needed to suppress the dominant $B^0 \to K^{*0}\gamma$ channel as much as possible, even at the cost of losing part of the signal.
- $K_2^{*0}(1430)$ veto: $1350\,\text{MeV} < m_{K\pi} < 1550\,\text{MeV}$ and $1350\,\text{MeV} < m_{\pi K} < 1550\,\text{MeV}$ regions are excluded. Besides $B^0 \to K^{*0}\gamma$, $B^0 \to K_2^{*0}(1430)\gamma$ happens to be an important peaking background with the same final state that needs to be suppressed.
- $D^0 \to K^+\pi^-$ veto: $1840\,\text{MeV} < m_{K\pi} < 1890\,\text{MeV}$ and $1840\,\text{MeV} < m_{\pi K} < 1890\,\text{MeV}$ regions are excluded. The D^0 is then combined with a random photon, contributing to the combinatorial background. This simple cut allows for the removal of some combinatorial background at little cost for the signal.
- $D^0 \to K^+K^-$ veto: $1850\,\text{MeV} < m_{KK} < 1890\,\text{MeV}$ is excluded. The D^0 is again suppressed, now from its decay into two kaons.
- $\Lambda^0(1520)$ veto: $1500\,\text{MeV} < m_{pK} < 1550\,\text{MeV}$ and $1500\,\text{MeV} < m_{Kp} < 1550\,\text{MeV}$ regions are excluded. The $\Lambda_b^0 \to \Lambda^{*0}\gamma$ resonances are also important peaking backgrounds that need suppression. Vetoes on the four considered Λ^{*0} are applied, which are further listed below, at the cost of losing a fraction of the signal.
- $\Lambda^0(1670)$ veto: $1640\,\text{MeV} < m_{pK} < 1700\,\text{MeV}$ and $1640\,\text{MeV} < m_{Kp} < 1700\,\text{MeV}$ regions are excluded.
- $\Lambda^0(1820)$,$\Lambda^0(1830)$ veto: $1780\,\text{MeV} < m_{pK} < 1880\,\text{MeV}$ and $1780\,\text{MeV} < m_{Kp} < 1880\,\text{MeV}$ regions are excluded.

In Figure 5.10 it is shown the dihadron mass distributions before and after applying the mass vetoes. The K^{*0}, ϕ and D^0 resonances are the ones that are more clear when looking at data. For completeness, Dalitz plots [63] have also been made to further show the effect of these vetoes, which can be seen in Figure A.1

Table 5.12: Summary of the veto efficiencies of the considered decay channels.

Decay mode	$\epsilon_{K^{*0}}$	$\epsilon_{\Lambda^{*0}}$	ϵ_{ϕ}	ϵ_{D^0}	ϵ_{Veto}
$B^0 \to K^{*0}\gamma$	0.102	0.328	0.965	0.986	0.032
$B^0 \to K^{*0}\gamma$ Ref	0.106	0.308	0.959	1	0.031
$B^0 \to \rho^0\gamma$	0.478	0.304	0.999	0.996	0.145
$B_s^0 \to \phi\gamma$	0.883	0.588	0.0002	1	0.0001
$\Lambda_b^0 \to \Lambda^0(1520)\gamma$	0.445	0.087	0.743	1	0.029
$\Lambda_b^0 \to \Lambda^0(1520)\gamma$ Ref	0.446	0.082	0.721	1	0.027
$\Lambda_b^0 \to \Lambda^0(1670)\gamma$	0.628	0.148	0.986	0.995	0.091
$\Lambda_b^0 \to \Lambda^0(1670)\gamma$ Ref	0.658	0.140	0.985	0.995	0.090
$\Lambda_b^0 \to \Lambda^0(1820)\gamma$	0.472	0.233	0.980	0.980	0.106
$\Lambda_b^0 \to \Lambda^0(1820)\gamma$ Ref	0.524	0.219	0.978	0.993	0.111
$\Lambda_b^0 \to \Lambda^0(1830)\gamma$	0.456	0.237	0.993	0.978	0.105
$\Lambda_b^0 \to \Lambda^0(1830)\gamma$ Ref	0.498	0.217	0.992	0.983	0.105
$B^0 \to K_2^{*0}(1430)\gamma$	0.179	0.741	0.999	0.845	0.112
$B^0 \to K_2^{*0}(1430)\gamma$ Ref	0.166	0.665	0.999	0.902	0.099
$B^+ \to K_1^{+}(1270)\gamma$	0.345	0.340	0.883	0.985	0.102
$B^+ \to K_1^{+}(1400)\gamma$	0.259	0.372	0.901	1	0.087
$B^+ \to K_2^{*+}(1430)\gamma$	0.195	0.376	0.954	0.992	0.069
$B^+ \to \overline{D}^0\rho^+$	0.338	0.846	1	0.955	0.273
$\Lambda_b^0 \to pK^-\gamma$	0.492	0.411	0.953	0.887	0.171
$\Lambda_b^0 \to pK^-\gamma$ Ref	0.500	0.365	0.943	0.924	0.159
$\Lambda_b^0 \to p\pi^-\gamma$	0.469	0.444	0.963	0.912	0.183

and Figure A.2. As with the kinematic BDT, the efficiency of the vetoes has been computed in bins of the Λ_b^0 mass to check that they do not create an artificial peak. As it can be seen in Figure 5.11, the vetoes do not present this issue.

Finally, Table 5.12 includes a summary detailing the efficiency of each of the vetoes. To make the table more readable, the efficiencies have been grouped into similar resonances

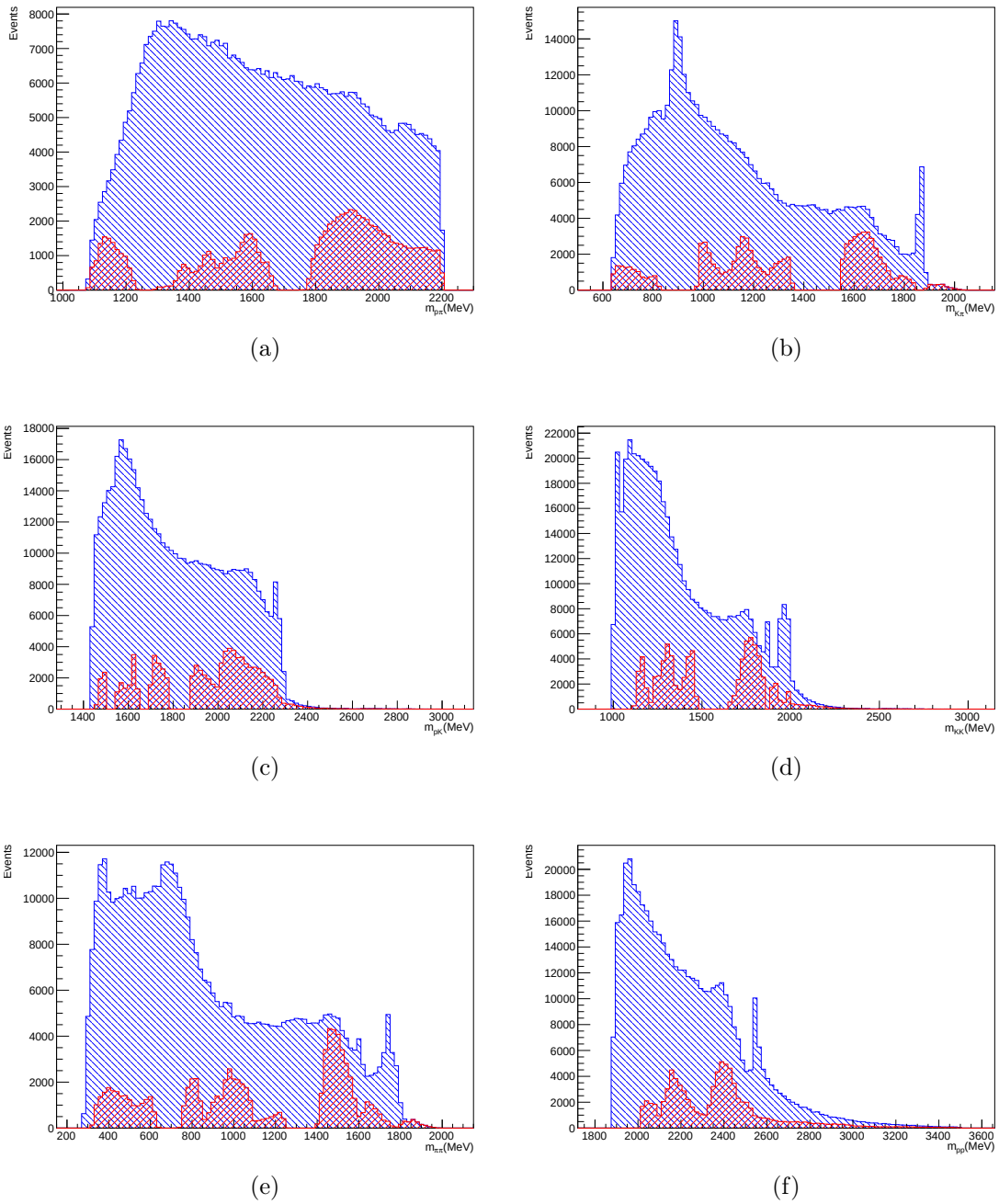

Figure 5.10: Data distributions before (blue) and after (red) applying the mass vetoes of the dihadron mass reconstructed as $p\pi$ (a), $K\pi$ (b), pK (c), KK (d), $\pi\pi$ (e), pp (f).

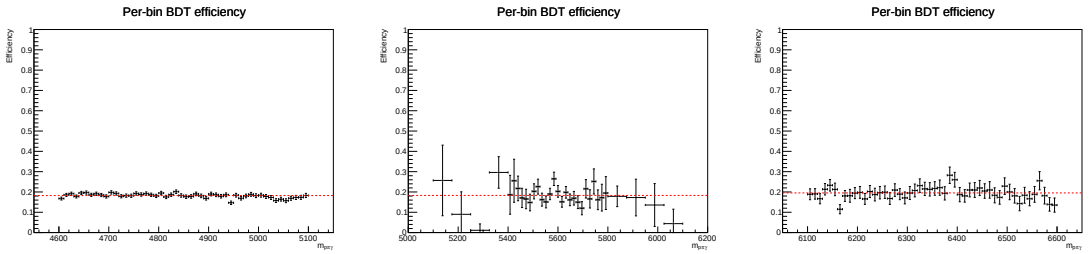

(a) (b) (c)

Figure 5.11: Efficiency of the vetoes for different bins of the Λ_b^0 mass in the low-mass sideband Figure 5.11a, signal region Figure 5.11b and high-mass sideband Figure 5.11c. The red dashed line marks the average efficiency.

5.3.5 Particle identification criteria

The goal of this section is to further suppress the peaking background contributions by imposing (PID) requirements on the final particles of the decay, particularly on the charged hadrons. A data-driven approach is used to overcome the misrepresentation of the PID-related variables on simulation. The PIDCalib package [64] provided by URANIA [65] is used to evaluate the efficiencies of the PID selection. The package includes large calibration samples of protons, kaons and pions, which have been selected from $D^{*+} \to (D^0 \to K^-\pi^+)\pi^+$, $\Lambda \to p\pi^-$ and $\Lambda_b^0 \to \Lambda_c^+\pi$ decays without using any PID information. It assumes that the efficiency of a given PID selection is a function exclusively of three variables: pseudorapidity(η), momentum (P) and the number of tracks (nTracks), thus assigning an efficiency to each bin. The latter variable is known to be poorly represented in simulation, so the total efficiency is just averaged over all the nTracks bins, at the cost of introducing a small systematic uncertainty.

After assigning an efficiency to each (η, P) bin, the different simulation samples are processed, assigning to each candidate the efficiency of the bin in which they fall in. The probability to pass a certain PID selection for each decay mode is then the average of the efficiencies assigned to every candidate (weighted average in case of the reweighted samples). Furthermore, as this selection does not eliminate any MC events, but rather assign a probability to pass it, this same efficiency can be interpreted as an event weight, which will be used in the different mass fits to catch any differences in the shape of the distributions caused by the PID selection.

The variables used to identify the charged hadrons are called ProbNN. These variables are built using multivariate techniques by combining tracking and PID information from all LHCb sub-systems. They result in a probability value for each mass hypothesis, from which we are interested in the proton, pion and kaon probabilities. In order to reduce the peaking background contributions as much as possible, cuts are applied on a combination of these variables, rather than on each variable independently, as the discrimination power may be maximal for one of such combinations. This possibility is examined by testing several combinations (Table 5.13), all of which provide a number between 0 and 1. The closer it is to 1,

Table 5.13: Combinations of PID variables tested. The proton selection is as showed, while for the pion selection one must swap p↔pi.

#	Combination
1	$ProbNNp > x$ AND $ProbNNk < y$ AND $ProbNNpi < z$
2	$ProbNNp(1 - ProbNNk)(1 - ProbNNpi) > x_p$
3	$(ProbNNp + (1 - ProbNNk) + (1 - ProbNNpi))/3 > x_p$
4	$(ProbNNp^2 + (1 - ProbNNk)^2 + (1 - ProbNNpi)^2)/3 > x_p$

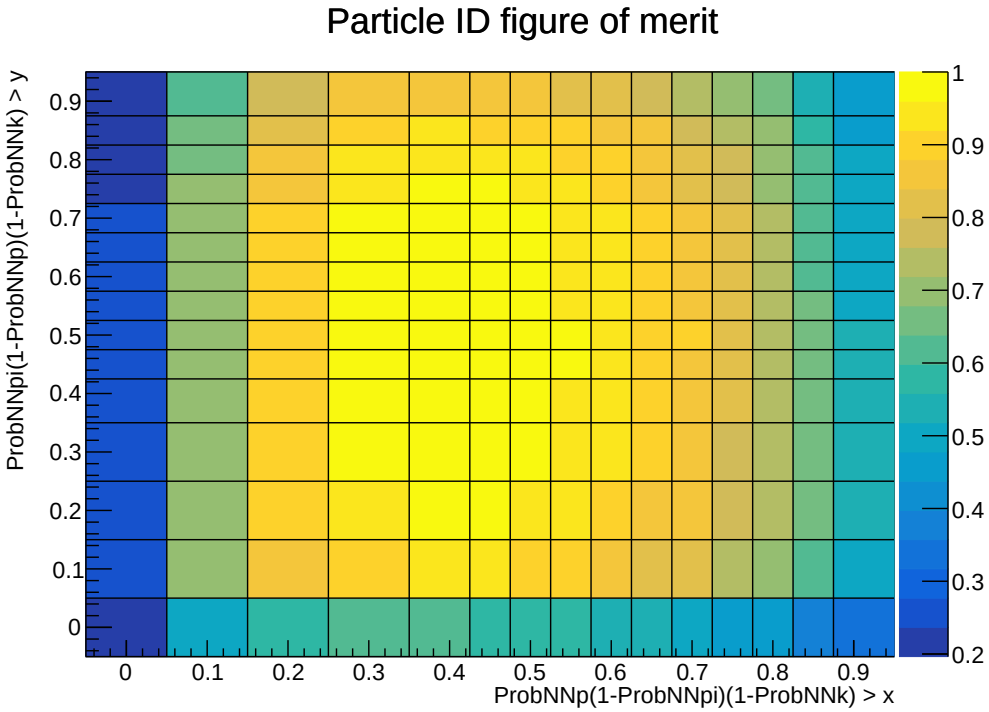

Figure 5.12: Distribution of the signal significance for the proton cut (X axis) against the pion cut (Y axis)

the higher the probability of that particle to be a proton or a pion, as one requests. The best combination is determined to be the one composed by the products of ProbNN's (option 2), followed by the naive linear cuts (option 1). Options 3 and 4 result in a weaker discriminant power than the linear cuts.

The condition imposed on the PID is such that the signal significance from Equation 5.5 is maximised. Again, using the number of data candidates already takes care of counting all the possible types of background, thus avoiding the need to calculate the expected yield of each cross-feed background contribution. 15×15 PID combinations are tested, as it is seen in Figure 5.12, where the conditions that maximise the FOM have been found to be $ProbNNp(1 - ProbNNk)(1 - ProbNNpi) > 0.4$ AND $ProbNNpi(1 - ProbNNk)(1 - ProbNNp) > 0.5$.

The efficiencies in Table 5.14 show the following hierarchy: the signal mode has the highest PID efficiency, as it is the most favoured by the selection; $B^0 \to K^{*0}\gamma$ and

Table 5.14: Summary of the PID efficiencies of the considered decay channels.

Decay mode	$\epsilon_{PID}(\cdot 10^{-2})$	$\epsilon_{PID}(\bar{p}_1\pi_2)(\cdot 10^{-2})$	$\epsilon_{PID}(p_1\bar{\pi}_2)(\cdot 10^{-2})$
$B^0 \to K^{*0}\gamma$	0.4	90.3	0.05
$B^0 \to K^{*0}\gamma$ Ref	0.006	3.8	0.1
$B^0 \to \rho^0\gamma$	0.15	89.9	0.02
$B_s^0 \to \phi\gamma$	0.01	2.6	0.5
$\Lambda_b^0 \to \Lambda^0(1520)\gamma$	2.0	1.0	66.3
$\Lambda_b^0 \to \Lambda^0(1520)\gamma$ Ref	0.008	1.7	0.4
$\Lambda_b^0 \to \Lambda^0(1670)\gamma$	1.8	1.0	61.8
$\Lambda_b^0 \to \Lambda^0(1670)\gamma$ Ref	0.01	2.9	0.4
$\Lambda_b^0 \to \Lambda^0(1820)\gamma$	2.2	1.3	54.9
$\Lambda_b^0 \to \Lambda^0(1820)\gamma$ Ref	0.02	3.6	0.4
$\Lambda_b^0 \to \Lambda^0(1830)\gamma$	1.6	1.0	55.4
$\Lambda_b^0 \to \Lambda^0(1830)\gamma$ Ref	0.02	3.9	0.4
$B^0 \to K_2^{*0}(1430)\gamma$	0.4	89.1	0.05
$B^0 \to K_2^{*0}(1430)\gamma$ Ref	0.005	3.3	0.2
$B^+ \to K_1^+(1270)\gamma$	0.4	89.5	0.05
$B^+ \to K_1^+(1400)\gamma$	0.4	90.0	0.04
$B^+ \to K_2^{*+}(1430)\gamma$	0.4	89.5	0.05
$B^+ \to \bar{D}^0\rho^+$	0.5	89.6	0.06
$\Lambda_b^0 \to pK^-\gamma$	2.0	1.4	53.5
$\Lambda_b^0 \to pK^-\gamma$ Ref	0.02	4.5	0.5
$\Lambda_b^0 \to p\pi^-\gamma$	56.1	35.3	5.1

$\Lambda_b^0 \to \Lambda^{*0}\gamma$-like decays follow, with efficiencies at the order of 1%, as only one of the two PID requirements favour them; the rest of the studied modes have even lower efficiencies, as they contain two ID misidentifications. It is important to remark here that the efficiencies of the reflections (the reconstruction possibility with the highest number of miss-identified particles with respect to the signal) are always one or two orders of magnitude smaller than their main counterparts, proving that our initial choice is correct.

In addition to the PID efficiencies of the selection for the signal channel, we present in Table 5.14 the efficiencies of the PID selections used to complete the simultaneous fit, in which either the $B^0 \to K^{*0}\gamma$ or the $\Lambda_b^0 \to \Lambda^{*0}\gamma$ events are enhanced. These cuts span from the original PID selection but the requirement is inverted, i.e. we require either that the first hadron is not a proton or that the second is not a pion (indicated by a bar). This way one can relate the original efficiency that selects protons and pions ($\epsilon(p_1\pi_2)$) to these inverted PID selections ($\epsilon(\bar{p}_1\pi_2)$, $\epsilon(p_1\bar{\pi}_2)$) using Bayes' theorem:

$$\epsilon(\bar{p}_1\pi_2) = \epsilon(\bar{p}_1|\pi_2)\epsilon(\pi_2) = (1 - \epsilon(p_1|\pi_2))\epsilon(\pi_2) = \epsilon(\pi_2) - \epsilon(p_1\pi_2) \tag{5.6}$$

$$\epsilon(p_1\bar{\pi}_2) = \epsilon(\bar{\pi}_2|p_1)\epsilon(p_1) = (1 - \epsilon(\pi_2|p_1))\epsilon(p_1) = \epsilon(p_1) - \epsilon(p_1\pi_2) \tag{5.7}$$

5.4 Signal and background shapes

After defining the selection, it is necessary to extract the mass shapes of the different decay modes which will be used in the simultaneous fit. This is done through maximum likelihood fit of MC samples, since the data does not provide enough statistics to properly define the details of each decay mode. The simultaneous fit, which is further described in section 5.6, includes a fit to three mass variables:

- $p\pi^-\ \gamma$ mass: The PID selection is the default one to search for the signal decay $\Lambda_b^0 \to p\pi^-\gamma$
- $K^+\pi^-\ \gamma$ mass: The PID selection has the cut on the proton inverted, thus enhancing decays like $B^0 \to K^{*0}\gamma$.
- $pK^-\ \gamma$ mass: The PID selection has the cut on the pion inverted, thus enhancing the yield of the normalisation channel $\Lambda_b^0 \to pK^-\gamma$.

5.4.1 $p\pi^-\ \gamma$ mass

The $p\pi^-\ \gamma$ mass variable is used to search for the signal mode and it is modelled with the following contributions:

- $B^0 \to K^+\pi^-\gamma$: modelled with a probability density function (pdf) composed by a Crystal-Ball distribution, where the other tail is an exponential (Equation 5.8). The sample is composed by merging the $B^0 \to K^{*0}\gamma$ and $B^0 \to K_2^{*0}(1430)\gamma$ MCs, normalised to the same equivalent luminosity (Equation 5.10). The resulting fit can be seen in Figure 5.13a.
- $\Lambda_b^0 \to pK^-\gamma$: modelled with a pdf composed by a gaussian core and two exponential tails (Equation 5.9). The result of the fit is shown in Figure 5.13b.
- $\Lambda_b^0 \to p\pi^-\gamma$: modelled with a Crystal-Ball with an exponential tail (Equation 5.8). Figure 5.13c shows the result of the fit.
- $B^0 \to K^+\pi^-\gamma$ Ref: modelled with a pdf composed by a Crystal-Ball with an exponential tail (Equation 5.8). The sample is composed by merging the $B^0 \to K^{*0}\gamma$ Ref and $B^0 \to K_2^{*0}(1430)\gamma$ Ref MCs and the resulting fit is in Figure 5.13d.
- $\Lambda_b^0 \to pK^-\gamma$ Ref: modelled with a pdf composed by a Crystal-Ball with two exponential tails (Equation 5.9). The fit obtained is shown in Figure 5.13e

The Crystal-Ball distribution, where the other tail is an exponential is defined as:

$$f_{CBExp}(x;\mu,\sigma,\alpha_L,\alpha_R,n) = N \begin{cases} A_L\left(B_L - \frac{x-\mu}{\sigma}\right)^{-n_L}, & \frac{x-\mu}{\sigma} \leq -\alpha_L \\ e^{-\frac{(x-\mu)^2}{2\sigma^2}}, & -\alpha_L < \frac{x-\mu}{\sigma} \leq -\alpha_R \\ e^{A_R\frac{x-\mu}{\sigma}+B_R}, & \frac{x-\mu}{\sigma} > \alpha_R \end{cases} \quad (5.8)$$

Where N is a normalisation constant and A_L, A_R, B_L, B_R are such that the distribution and its first derivative are continuous. This distribution has 1 less degree of

freedom than the double-sided Crystal-Ball, and it is useful when the power of one of the tails becomes large. On the other hand, if both tails decay exponentially, the distribution is defined as:

$$f_{DoubleGaussExp}(x;\mu,\sigma,\alpha_L,\alpha_R) = N \begin{cases} e^{A_L \frac{x-\mu}{\sigma}+B_L}, & \frac{x-\mu}{\sigma} < -\alpha_L \\ e^{-\frac{(x-\mu)^2}{2\sigma^2}}, & -\alpha_L < \frac{x-\mu}{\sigma} \leq -\alpha_R \\ e^{A_R \frac{x-\mu}{\sigma}+B_R}, & \frac{x-\mu}{\sigma} > \alpha_R \end{cases} \tag{5.9}$$

Where N is a normalisation constant and A_L, A_R, B_L, B_R are such that the distribution and its first derivative are continuous. This distribution has 2 less degrees of freedom than the double-sided Crystal-Ball, and it is useful when the power of both tails becomes large.

On the other hand, we have employed the concept of equivalent luminosity to merge different MC samples. This is used to compensate for the different number of events generated for each sample, differences in the Branching Fractions and in the hadronization factors. Effectively, this applies a common weight to all the events within a certain sample, which is defined as:

$$W_X = \frac{N^{gen}_{B^0 \to K^{*0}\gamma}}{N^{gen}_X} \frac{\mathcal{B}(X)}{\mathcal{B}(B^0 \to K^{*0}\gamma)} \frac{f_{X_{mother}}}{f_{B^0}} \tag{5.10}$$

Notice that it defaults to 1 in the case of the $B^0 \to K^{*0}\gamma$, which is taken as reference.

The results of the MC $p\pi^-$ γ mass fits are shown in Table 5.15, along the uncertainties obtained from inverting the Hessian matrix. The results are shown in Figure 5.13, where it can be seen that the distributions are able to describe the MC samples.

Table 5.15: Results of the different fits of the $p\pi\ \gamma$ mass in MC.

MC sample	Parameter	Value
$B^0 \to K^+\pi^-\gamma$	μ(MeV)	5467 ± 6
	σ(MeV)	112 ± 6
	α_L	2.0 ± 0.27
	n	3.9 ± 2.9
	α_R	0.87 ± 0.08
$\Lambda_b^0 \to pK^-\gamma$	μ(MeV)	5490 ± 8
	σ(MeV)	103 ± 13
	α_L	1.2 ± 0.3
	α_R	1.3 ± 0.3
$\Lambda_b^0 \to p\pi^-\gamma$	μ(MeV)	5596 ± 6
	σ(MeV)	93 ± 5
	α_L	3.2 ± 0.5
	n	0.3 ± 0.6
	α_R	1.8 ± 0.6
$B^0 \to K^+\pi^-\gamma$ Ref	μ(MeV)	5574 ± 16
	σ(MeV)	152 ± 13
	α_L	2.6 ± 0.9
	n	1 ± 3
	α_R	0.92 ± 0.16
$\Lambda_b^0 \to pK^-\gamma$ Ref	μ(MeV)	5530 ± 30
	σ(MeV)	190 ± 90
	α_L	1.3 ± 1.3
	α_R	1.3 ± 0.9

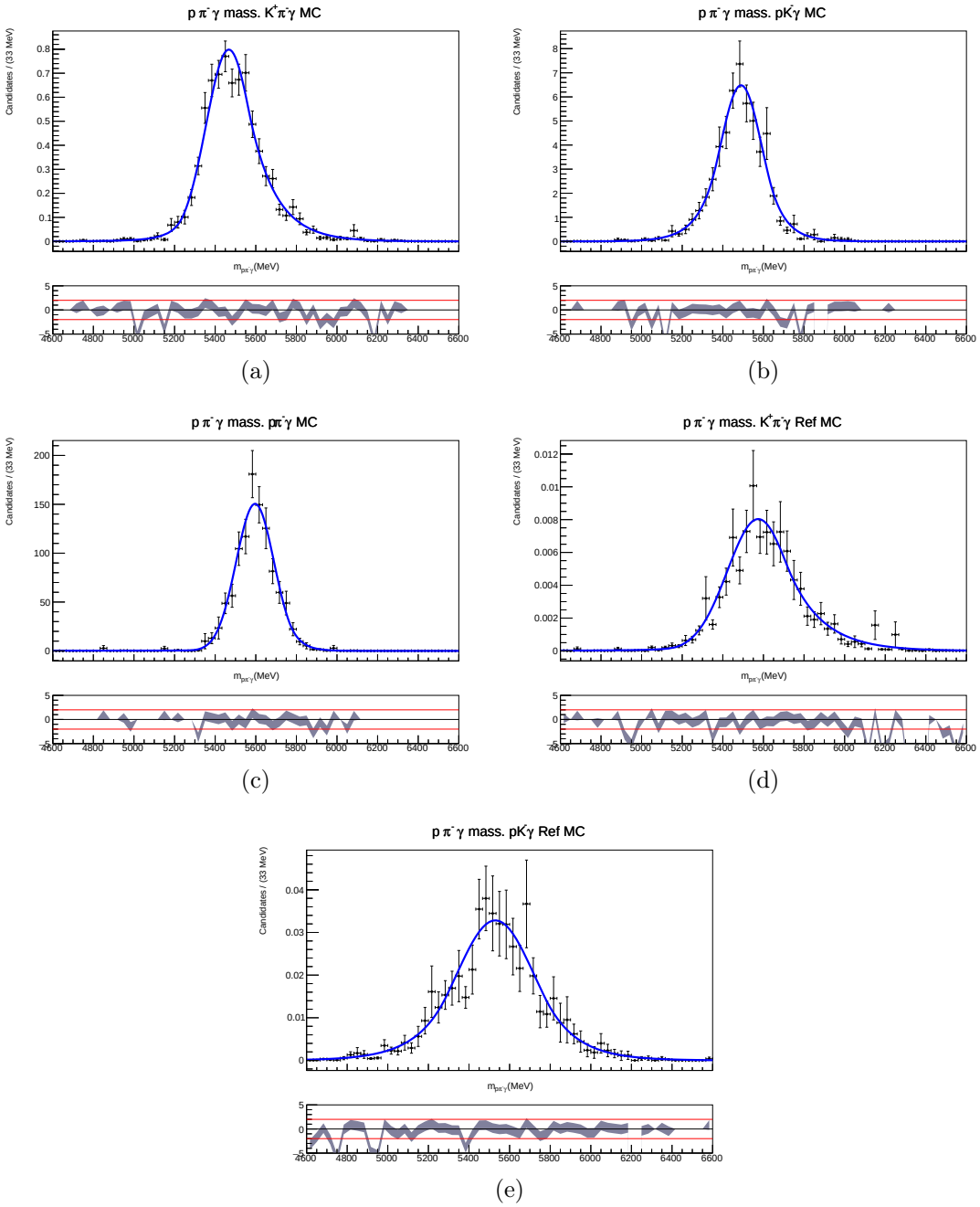

Figure 5.13: Fits to the $p\pi$ γ mass to MC samples of Figure 5.13a: $B^0 \to K^{*0}\gamma$ and $B^0 \to K_2^{*0}(1430)\gamma$, Figure 5.13b: $\Lambda_b^0 \to pK^-\gamma$, Figure 5.13c: $\Lambda_b^0 \to p\pi^-\gamma$, Figure 5.13d: $B^0 \to K^{*0}\gamma$ Ref and $B^0 \to K_2^{*0}(1430)\gamma$ Ref, Figure 5.13e: $\Lambda_b^0 \to pK^-\gamma$ Ref.

5.4.2 $K^+\pi^-$ γ mass

The $K^+\pi^-$ γ mass variable is modelled with the following contributions:

- $B^0 \to K^+\pi^-\gamma$: modelled with a pdf composed by a Crystal-Ball distribution with an exponential tail (Equation 5.8). The sample is composed by merging the $B^0 \to K^{*0}\gamma$ and $B^0 \to K_2^{*0}(1430)\gamma$ MCs, and the result of the fit is shown in Figure 5.14a.
- $\Lambda_b^0 \to pK^-\gamma$: modelled by a gaussian core with two exponential tails (Equation 5.9). Figure 5.14b shows the result of the fit.
- $\Lambda_b^0 \to p\pi^-\gamma$: modelled by a gaussian core with two exponential tails (Equation 5.9). The result of the fit can be seen in Figure 5.14c.
- $B^0 \to K^+\pi^-\gamma$ Ref: modelled with a pdf composed by a Crystal-Ball with an exponential tail (Equation 5.8). The sample is composed by merging the $B^0 \to K^{*0}\gamma$ Ref and $B^0 \to K_2^{*0}(1430)\gamma$ Ref MCs, and the resulting fit can be seen in Figure 5.14d.
- $\Lambda_b^0 \to pK^-\gamma$ Ref: modelled with a pdf composed by a Crystal-Ball with an exponential tail (Equation 5.8). The result of the fit is in Figure 5.14e
- $B^+ \to K^+\pi^-\pi^+\gamma$: modelled with a pdf made from convoluting an ARGUS (Equation 5.11) with a gaussian distribution (Equation 5.12). The sample is composed by merging the simulation samples of $B^+ \to K_1^+(1270)\gamma$, $B^+ \to K_1^+(1400)\gamma$ and $B^+ \to K_2^{*+}(1430)\gamma$. The resulting fit is shown in Figure 5.14f.

The ARGUS distribution has two parameters: c and m_0 and is defined as:

$$f_{ARGUS}(x; c, m_0) = N \begin{cases} x\sqrt{1 - \frac{x^2}{m_0^2}}\, e^{c\left(1 - \frac{x^2}{m_0^2}\right)}, & x \leq m_0 \\ 0, & x > m_0 \end{cases} \tag{5.11}$$

While its convolution with a gaussian adds a third parameter, σ, and reads:

$$f_{ARGUSGauss}(x; c, m_0, \sigma) = f_{ARGUS}(x; c, m_0) * f_{Gauss}(x; 0, \sigma) \tag{5.12}$$

The results of the MC $K^+\pi^-$ γ mass fits are shown in Table 5.16, along the uncertainties obtained from inverting the Hessian matrix. The results are shown in Figure 5.14, where it can be seen that the distributions are able to describe the MC samples.

Table 5.16: Results of the different fits of the $K\pi$ γ mass in MC.

MC sample	Parameter	Value
$B^0 \to K^+\pi^-\gamma$	μ(MeV)	5258 ± 2
	σ(MeV)	86 ± 2
	α_L	2.64 ± 0.15
	n	0.4 ± 0.2
	α_R	1.18 ± 0.07
$\Lambda_b^0 \to pK^-\gamma$	μ(MeV)	5286 ± 10
	σ(MeV)	123 ± 12
	α_L	0.82 ± 0.15
	α_R	1.5 ± 0.2
$\Lambda_b^0 \to p\pi^-\gamma$	μ(MeV)	5435 ± 12
	σ(MeV)	112 ± 12
	α_L	0.70 ± 0.12
	α_R	2.2 ± 1.2
$B^0 \to K^+\pi^-\gamma$ Ref	μ(MeV)	5309 ± 4
	σ(MeV)	112 ± 3
	α_L	2.3 ± 0.2
	n	1.0 ± 0.7
	α_R	1.48 ± 0.12
$\Lambda_b^0 \to pK^-\gamma$ Ref	μ(MeV)	5260 ± 14
	σ(MeV)	143 ± 21
	α_L	0.8 ± 0.4
	n	6 ± 19
	α_R	1.6 ± 0.6
$B^+ \to K^+\pi^-\pi^+\gamma$	m_0(MeV)	5100 ± 12
	c	-10.7 ± 1.4

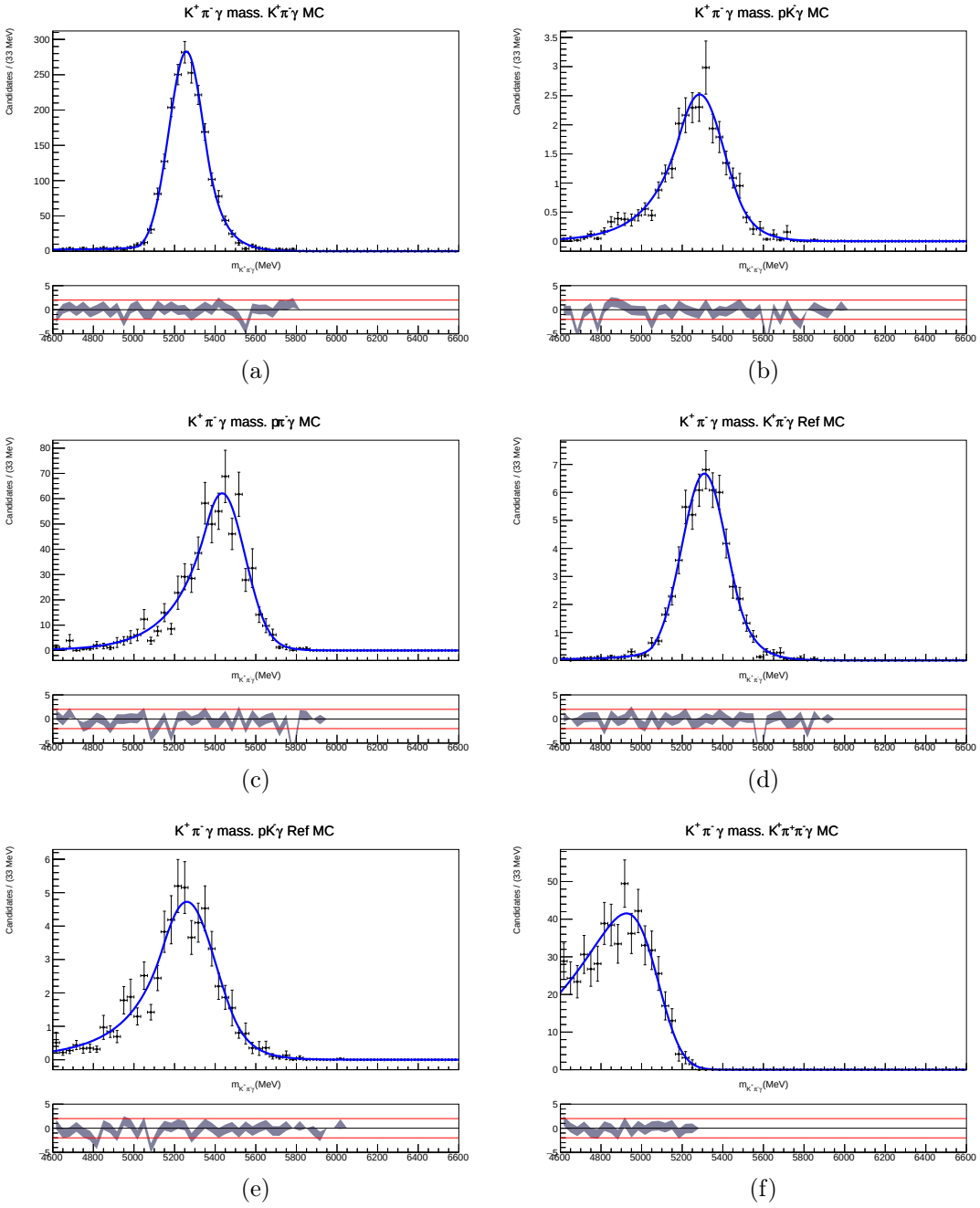

(a) (b) (c) (d) (e) (f)

Figure 5.14: Fits to the $K\pi$ γ mass to MC samples of Figure 5.14a: $B^0 \to K^{*0}\gamma$ and $B^0 \to K_2^{*0}(1430)\gamma$, Figure 5.14b: $\Lambda_b^0 \to pK^-\gamma$, Figure 5.14c: $\Lambda_b^0 \to p\pi^-\gamma$, Figure 5.14d: $B^0 \to K^{*0}\gamma$ Ref and $B^0 \to K_2^{*0}(1430)\gamma$ Ref, Figure 5.14e: $\Lambda_b^0 \to pK^-\gamma$ Ref, Figure 5.14f: $B^+ \to K_1^+(1270)\gamma$, $B^+ \to K_1^+(1400)\gamma$ and $B^+ \to K_2^{*+}(1430)\gamma$.

5.4.3 $pK^-\ \gamma$ mass

The $pK^-\ \gamma$ mass variable is modelled with the following contributions:

- $B^0 \to K^+\pi^-\gamma$: modelled with a pdf composed by a Crystal-Ball distribution with an exponential tail (Equation 5.8). The sample is composed by merging the $B^0 \to K^{*0}\gamma$ and $B^0 \to K_2^{*0}(1430)\gamma$ MCs and the resulting fit is shown in Figure 5.15a.
- $\Lambda_b^0 \to pK^-\gamma$: modelled with a pdf composed by a Crystal-Ball distribution with an exponential tail (Equation 5.8). The result of the fit can be seen in Figure 5.15b
- $\Lambda_b^0 \to p\pi^-\gamma$: modelled with a Crystal-Ball with an exponential tail (Equation 5.8). The resulting fit is shown in Figure 5.15c.
- $B^0 \to K^+\pi^-\gamma$ Ref: modelled with a pdf composed by a gaussian core and two exponential tails (Equation 5.9). The sample is composed by merging the $B^0 \to K^{*0}\gamma$ Ref and $B^0 \to K_2^{*0}(1430)\gamma$ Ref MCs and the result of the fit can be seen in Figure 5.15d.
- $\Lambda_b^0 \to pK^-\gamma$ Ref: modelled with a pdf composed by a gaussian core with two exponential tails (Equation 5.9). The resulting fit can be seen in Figure 5.15e.

The results of each fit to $pK^-\ \gamma$ mass can be found in Table 5.17, along the uncertainties obtained from inverting the Hessian matrix. The graphical representation of the fits are all shown in Figure 5.15, where it can be seen that the distributions are able to describe the MC samples.

Table 5.17: Results of the different fits of the pK γ mass in MC.

MC sample	Parameter	Value
$B^0 \to K^+\pi^-\gamma$	μ(MeV)	5590 ± 3
	σ(MeV)	128 ± 8
	α_L	2.8 ± 0.7
	n	0.9 ± 1.6
	α_R	0.91 ± 0.07
$\Lambda_b^0 \to pK^-\gamma$	μ(MeV)	5602 ± 4
	σ(MeV)	84 ± 3
	α_L	2.1 ± 0.3
	n	3 ± 3
	α_R	1.11 ± 0.09
$\Lambda_b^0 \to p\pi^-\gamma$	μ(MeV)	5740 ± 7
	σ(MeV)	101 ± 6
	α_L	3.1 ± 0.8
	n	1.0 ± 1.9
	α_R	0.95 ± 0.10
$B^0 \to K^+\pi^-\gamma$ Ref	μ(MeV)	5607 ± 14
	σ(MeV)	120 ± 16
	α_L	1.4 ± 0.3
	α_R	0.65 ± 0.13
$\Lambda_b^0 \to pK^-\gamma$ Ref	μ(MeV)	5673 ± 13
	σ(MeV)	173 ± 19
	α_L	1.5 ± 0.6
	α_R	1.3 ± 0.3

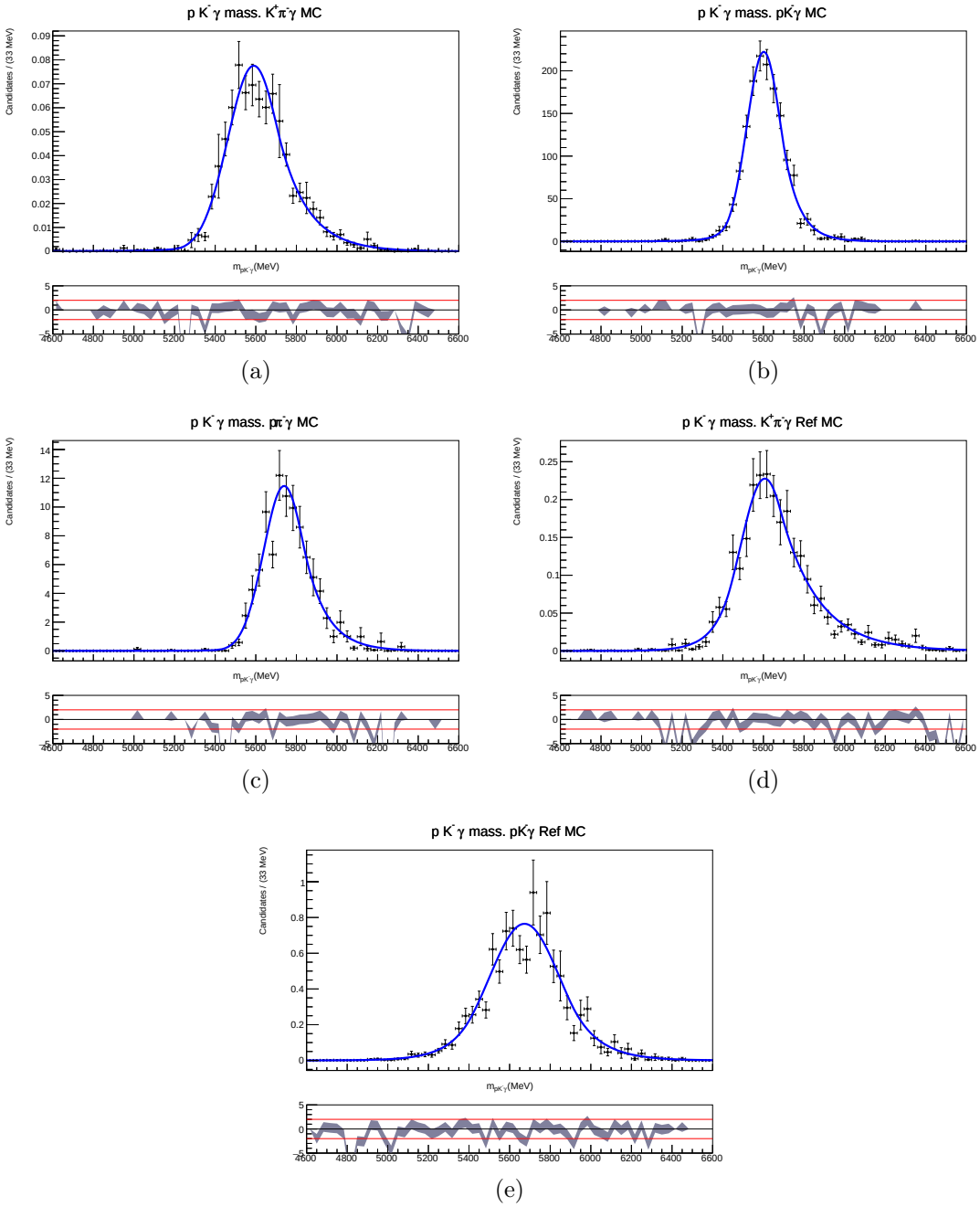

(a) (b) (c) (d) (e)

Figure 5.15: Fits to the $pK\ \gamma$ mass to MC samples of Figure 5.15a: $B^0 \to K^{*0}\gamma$ and $B^0 \to K_2^{*0}(1430)\gamma$, Figure 5.15b: $\Lambda_b^0 \to pK^-\gamma$, Figure 5.15c: $\Lambda_b^0 \to p\pi^-\gamma$, Figure 5.15d: $B^0 \to K^{*0}\gamma$ Ref and $B^0 \to K_2^{*0}(1430)\gamma$ Ref, Figure 5.15e: $\Lambda_b^0 \to pK^-\gamma$ Ref.

5.5 Extraction of the branching ratio

The branching fraction of the signal and normalisation modes can both be related to the number of events observed through:

$$N_{\Lambda_b^0\to p\pi^-\gamma}(p\pi) = \mathcal{L}_{\rm int}\sigma(b\bar{b}X) f_{\Lambda_b^0} \mathcal{B}\big(\Lambda_b^0 \to p\pi^-\gamma\big)\epsilon_{\Lambda_b^0\to p\pi^-\gamma}(p\pi) \tag{5.13}$$

$$N_{\Lambda_b^0\to pK^-\gamma}(p\bar{\pi}) = \mathcal{L}_{\rm int}\sigma(b\bar{b}X) f_{\Lambda_b^0} \mathcal{B}\big(\Lambda_b^0 \to pK^-\gamma\big)\epsilon_{\Lambda_b^0\to pK^-\gamma}(p\bar{\pi}) \tag{5.14}$$

Where $\mathcal{L}_{\rm int}$ is the integrated luminosity of the data sample, $\sigma(b\bar{b}X)$ is the cross-section for producing b quarks in the pp collision and $f_{\Lambda_b^0}$ is the hadronization factor, which dictates the probability of the b quark to hadronise into a Λ_b^0. The selections used to retrieve the number of $\Lambda_b^0 \to p\pi^-\gamma$ and $\Lambda_b^0 \to pK^-\gamma$ events are slightly different, only differing in the PID criteria, which is indicated by either $(p\pi)$ or $(p\bar{\pi})$, respectively. Dividing Equation 5.13 by Equation 5.14 and rearranging the terms results in the expression for the branching ratio:

$$\frac{\mathcal{B}(\Lambda_b^0 \to p\pi^-\gamma)}{\mathcal{B}(\Lambda_b^0 \to pK^-\gamma)} = \frac{N_{\Lambda_b^0\to p\pi^-\gamma}(p_1\pi_2)}{N_{\Lambda_b^0\to pK^-\gamma}(p_1\bar{\pi}_2)} \frac{\epsilon_{\Lambda_b^0\to pK^-\gamma}(p_1\bar{\pi}_2)}{\epsilon_{\Lambda_b^0\to p\pi^-\gamma}(p_1\pi_2)} \tag{5.15}$$

This way, the luminosity and the cross-section are cancelled out because the data used is the same for both decay modes, while the poorly-known hadronization fractions also vanish due to both decays having the same mother particle, a Λ_b^0. In the same sense, the ratio of branching fractions also allows for the cancellation of some systematic uncertainties. For instance, discrepancies between data and MC of the kinematics of the Λ_b^0 are suppressed, since they will affect both modes equally.

Equation 5.15 also reflects the two main inputs needed for the search. The first comes from fitting the data to retrieve the number of signal and normalisation events observed. Hence, it carries both an statistic and a systematic uncertainty. On the other hand, the ratio of efficiencies is determined using the MC samples, as well as some control data samples, so by definition it only carries systematic uncertainties, the study of which is done in section 5.7. For completeness, the total ratio of efficiencies is defined as:

$$\frac{\epsilon_{\Lambda_b^0\to pK^-\gamma}(p\bar{\pi})}{\epsilon_{\Lambda_b^0\to p\pi^-\gamma}(p\pi)} = \frac{\epsilon_{A+R+T+S}\epsilon_{presel}\epsilon_{BDT}\epsilon_{Veto}\epsilon_{PID}(p_1\bar{\pi}_2)(\Lambda_b^0 \to pK^-\gamma)}{\epsilon_{A+R+T+S}\epsilon_{presel}\epsilon_{BDT}\epsilon_{Veto}\epsilon_{PID}(p_1\pi_2)(\Lambda_b^0 \to p\pi^-\gamma)} = 0.74 \pm 0.06 \tag{5.16}$$

Where the quoted uncertainty includes all the systematic effects introduced in section 5.7 and each individual efficiency has already been shown in their respective sections: $\epsilon_{A+R+T+S}$ in subsection 5.3.2, ϵ_{presel} and ϵ_{BDT} in subsection 5.3.3, ϵ_{Veto} in subsection 5.3.4 and ϵ_{PID} in subsection 5.3.5. The huge similarity between the two efficiencies once again shows how similar the kinematics and the topology of these two decay modes are, with few tools available to disentangle them: PID and mass vetoes.

5.6 Simultaneous mass fit

With the ratio of efficiencies being computed with Equation 5.16, we are left with the number of $\Lambda_b^0 \to p\pi^-\gamma$ and $\Lambda_b^0 \to pK^-\gamma$ events to compute the Branching Ratio. These numbers are extracted from a simultaneous unbinned maximum likelihood fit to three mass variables from the data: $m_{p\pi^-}$, $m_{K^+\pi^-}$ and m_{pK^-}, where each data sample has been obtained using its corresponding PID selection, as described in subsection 5.3.5.

Finally, many of the parameters in the fit have been determined and fixed from fits to MC, which are described in section 5.4, mainly related to the shape and tail features of the different physical contributions. On the other hand, the yields of the three main peaking components ($\Lambda_b^0 \to p\pi^-\gamma$, $B^0 \to K^+\pi^-\gamma$, and $\Lambda_b^0 \to pK^-\gamma$) have been left free to vary in the fit, but their contamination in the other mass windows is gaussian-constrained to the required efficiencies.

In the $p\pi^-\gamma$ mass window, the PDF is defined as follows:

- $B^0 \to K^+\pi^-\gamma$: All parameters are fixed to the values found in MC, while the yield is left free to vary.
- $\Lambda_b^0 \to pK^-\gamma$: All parameters are fixed from MC, with the yield left free in the simultaneous fit.
- $\Lambda_b^0 \to p\pi^-\gamma$: The mean ($\mu$) and the yield are left free, with the width tied to the $\Lambda_b^0 \to pK^-\gamma$ width in the $pK^-\gamma$ mass window. The other parameters are fixed from MC.
- $B^0 \to K^+\pi^-\gamma$ Ref: All parameters are fixed from MC, and the yield is Gaussian-constrained to the $B^0 \to K^+\pi^-\gamma$ yield, where the mean and width of the constraint is obtained from the efficiency and its uncertainty.
- $\Lambda_b^0 \to pK^-\gamma$ Ref: All parameters are fixed from MC, while its yield is Gaussian-constrained to the $\Lambda_b^0 \to pK^-\gamma$ yield.
- Combinatorial: Modelled with an exponential function, which is completely free to vary in the fit.

In the $K^+\pi^-\gamma$ mass window the parameters are:

- $B^0 \to K^+\pi^-\gamma$: The tail parameters remain fixed from MC, while its mean and width (σ) are left free. Its yield is Gaussian-constrained to the yield in the $p\pi^-\gamma$ mass window.
- $\Lambda_b^0 \to pK^-\gamma$: All parameters are fixed from MC, while its yield is Gaussian-constrained to its yield in the $p\pi^-\gamma$ mass.
- $\Lambda_b^0 \to p\pi^-\gamma$: All parameters are fixed from MC, with its yield being Gaussian-constrained to its yield in the $p\pi^-\gamma$ mass.
- $B^0 \to K^+\pi^-\gamma$ Ref: All parameters fixed from MC, while the yield is Gaussian-constrained to its $p\pi^-\gamma$ mass counterpart.

- $\Lambda_b^0 \to pK^-\gamma$ Ref: All the parameters are fixed from MC, with its yield Gaussian-constrained to its $p\pi^-\gamma$ mass counterpart.
- $B^+ \to K^+\pi^-\pi^+\gamma$: The parameters of the PDF are fixed from MC, while the yield is left free to vary.
- Combinatorial 1: modelled with a straight line with its slope and yield left free to vary in the fit.
- $B^+ \to \overline{D}^0\rho^+$: This contribution is modelled with an exponential function, with its parameter and yield left free to vary.

Finally, in the $pK^-\gamma$ mass window we have:

- $B^0 \to K^+\pi^-\gamma$: The parameters of the PDF are fixed from MC, while the yield is gaussian-constrained to its $p\pi^-\gamma$ counterpart.
- $\Lambda_b^0 \to pK^-\gamma$: The tail parameters are fixed from MC, with the mean and width being left free in the simultaneous fit. The yield is gaussian-constrained to its $p\pi^-\gamma$ counterpart.
- $\Lambda_b^0 \to p\pi^-\gamma$: All parameters are fixed from MC, with the yield Gaussian-constrained to its $p\pi^-\gamma$ counterpart.
- $B^0 \to K^+\pi^-\gamma$ Ref: All parameters are fixed from MC, with the yield Gaussian-constrained to its $p\pi^-\gamma$ counterpart.
- $\Lambda_b^0 \to pK^-\gamma$ Ref: All the parameters are fixed from MC, with the yield being Gaussian-constrained to its $p\pi^-\gamma$ counterpart.
- Combinatorial: modelled with a an exponential function with its parameter and yield left free to vary in the fit.

All in all, the fit contains 17 free parameters, from which 3 correspond to the yields of the main peaking contributions, 6 correspond to the 3 combinatorials (their parameter and the yield); 2 to the yield and parameter of the $B^+ \to \overline{D}^0\rho^+$ component; 1 to the yield of the $B^+ \to K^+\pi^-\pi^+\gamma$ partially reconstructed decay and 5 to the mean and width of the gaussian of the dominant peak, with the exception of the signal width which is bound to the width of the $\Lambda_b^0 \to pK^-\gamma$ contribution in the $pK^-\gamma$ mass window. In addition, the 12 yields of the other non-dominant peaking backgrounds are not fully determined through the efficiencies, but gaussian-constrained to allow fluctuations within the uncertainty.

The final values of the free parameters, along all the yields, are shown in Table 5.18. The result confirms that there is an important cross-feed contamination coming from $B^0 \to K^+\pi^-\gamma$ and $\Lambda_b^0 \to pK^-\gamma$ decays into the $p\pi^-\ \gamma$ mass. It also shows that the reflected samples are more suppressed when going into the $p\pi^-\ \gamma$ due to the PID selection.

Table 5.18: Results of the simultaneous fit on Run I data. Only free or gaussian-constrained parameters are shown.

Variable	Parameter	Value
$p\pi\ \gamma$ mass	$\mu_{p\pi\gamma}(\,\mathrm{MeV})$	5620 ± 22
	$\tau_{Comb}(\cdot 10^{-3}\,\mathrm{MeV}^{-1})$	-0.91 ± 0.10
	N_{Comb}	344 ± 20
	$\mathbf{N_{p\pi\gamma}}$	$\mathbf{30 \pm 9}$
	$N_{K\pi\gamma}$	4.7 ± 1.7
	$N_{pK\gamma}$	13.8 ± 2.6
	$N_{K\pi\gamma Ref}$	0.06 ± 0.2
	$N_{pK\gamma Ref}$	0.1 ± 0.3
$K\pi\ \gamma$ mass	$\mu_{K\pi\gamma}(\,\mathrm{MeV})$	5261 ± 5
	$\sigma_{K\pi\gamma}(\,\mathrm{MeV})$	84 ± 5
	$\tau_{B^+\to\bar{D}^0\rho^+}(\cdot 10^{-3}\,\mathrm{MeV}^{-1})$	-4.2 ± 0.7
	$Slope_{Comb}(\cdot 10^{-4}\,\mathrm{MeV}^{-2})$	-1.41 ± 0.02
	$N_{B^+\to\bar{D}^0\rho^+}$	4300 ± 250
	N_{Comb}	3400 ± 600
	$N_{p\pi\gamma}$	19 ± 6
	$N_{K\pi\gamma}$	1300 ± 900
	$N_{pK\gamma}$	10 ± 4
	$N_{K\pi\gamma Ref}$	40 ± 24
	$N_{pK\gamma Ref}$	27 ± 9
$pK\ \gamma$ mass	$\mu_{pK\gamma}(\,\mathrm{MeV})$	5596 ± 5
	$\sigma_{pK\gamma}(\,\mathrm{MeV})$	67 ± 4
	$\tau_{Comb}(\cdot 10^{-3}\,\mathrm{MeV}^{-1})$	-1.49 ± 0.09
	N_{Comb}	650 ± 30
	$N_{p\pi\gamma}$	2.8 ± 1.0
	$N_{K\pi\gamma}$	0.6 ± 0.7
	$\mathbf{N_{pK\gamma}}$	$\mathbf{407 \pm 24}$
	$N_{K\pi\gamma Ref}$	1.6 ± 1.5
	$N_{pK\gamma Ref}$	2.6 ± 1.7

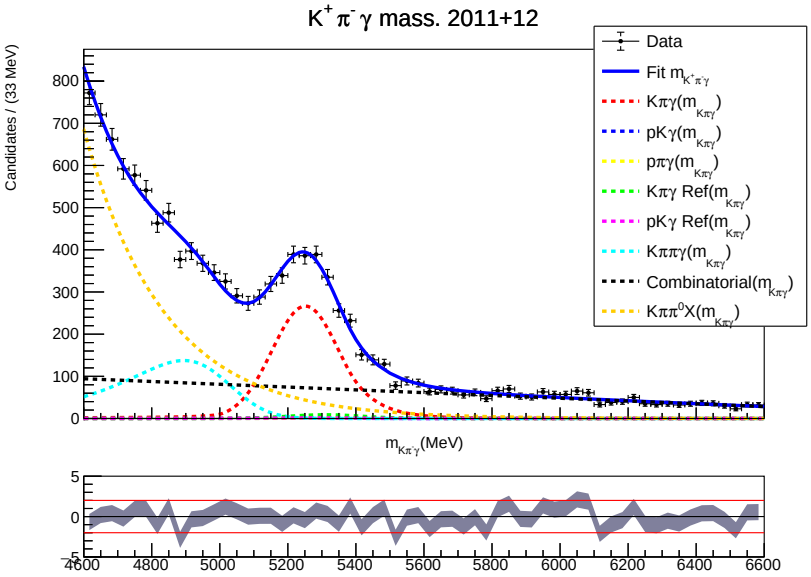

(a)

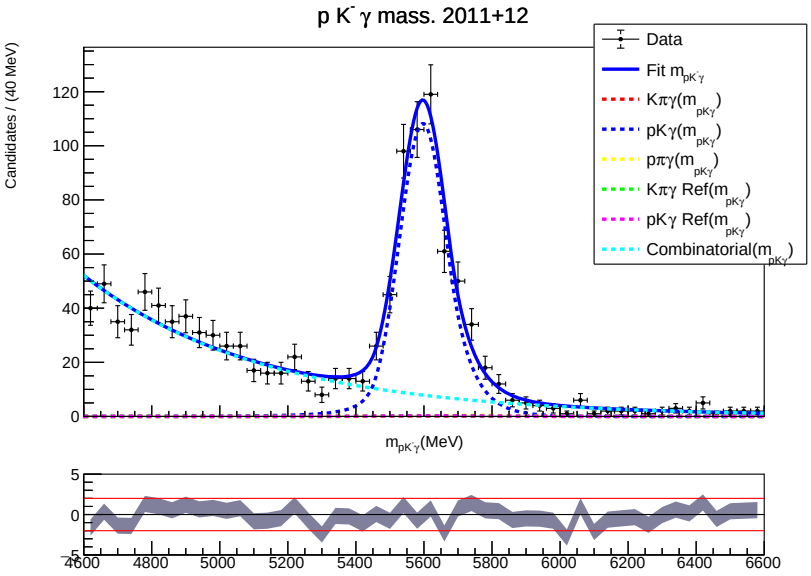

(b)

Figure 5.16: Result of the simultaneous fit on Run I data. Figure 5.16a shows the $K^+\pi^-\gamma$ mass slice and Figure 5.16b shows the $pK^-\gamma$.

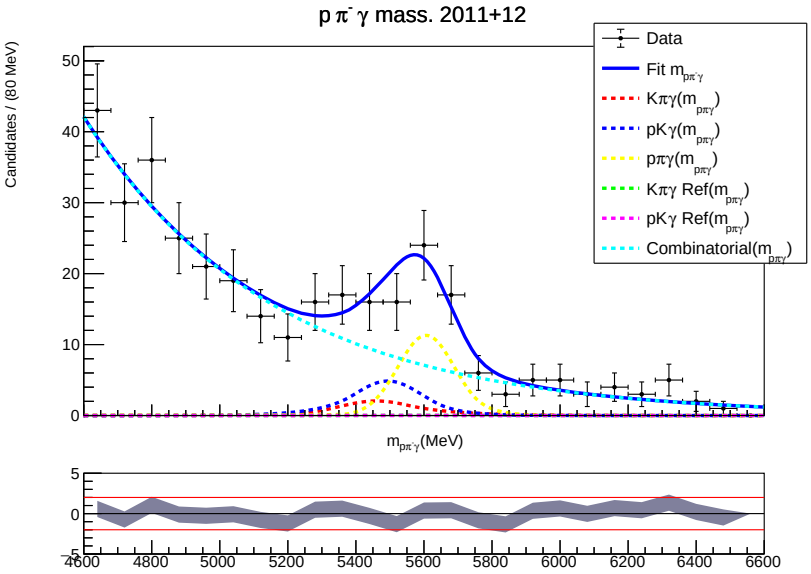

(c)

Figure 5.16: (Cont.) Result of the simultaneous fit on Run I data. Figure 5.16c shows the $p\pi^-\ \gamma$ mass fit.

5.7 Systematic uncertainties

The systematic uncertainties that affect the measurement of the branching ratio are discussed in this section. Mainly, these are related to the measurement of the efficiencies, although we also explore changes in the measured yields when the fit is slightly modified.

5.7.1 Control of the MC peaking background shapes

It is known that the MC does not exactly reproduce the mass shapes of the different decays, which raises a concern on the sensitivity of the simultaneous fit to the shapes of the peaking backgrounds, mainly their means and widths, which directly affect on how much the signal and peaking background distributions overlap. For example, if their means were actually higher, the signal yield would drop, along with the branching ratio.

In order to tackle this problem, we first focus on the position of the peaking backgrounds. For that, we obtain the mean of the $\Lambda_b^0 \to pK^-\gamma$ and $B^0 \to K^+\pi^-\gamma$ masses in the $p\pi^-\gamma$ mass window from data, for which we remove part of the vetoes and invert the PID cuts from Table 5.19 to get a clearer peak. The newly obtained values for the means are compared to the MC ones, and the simultaneous fit is repeated twice, once by rising and another by lowering them according to their difference between data and MC. This probes the sensitivity of the signal yield to a shift in the mean

The simultaneous fits preformed follow exactly the same structure described in section 5.6, with the only exception that the means of the $\Lambda_b^0 \to pK^-\gamma$ and

Table 5.19: Changes in the selection to fit the miss-ID background peaks using $p\pi^-\gamma$ mass hypothesis. The masses are expressed in MeV.

Original selection	$K^+\pi^-\ \gamma$	$pK^-\ \gamma$
$m_{K^+\pi^-} < 820$ OR $m_{K^+\pi^-} > 980$ $m_{\pi^+K^-} < 820$ OR $m_{\pi^+K^-} > 980$ $m_{K^+\pi^-} < 1350$ OR $m_{K^+\pi^-} > 1550$ $m_{\pi^+K^-} < 1350$ OR $m_{\pi^+K^-} > 1550$	$820 < m_{K^+\pi^-} < 980$ OR $1350 < m_{K^+\pi^-} < 1550$	Unchanged
$m_{pK^-} < 1500$ OR $m_{pK^-} > 1550$ $m_{K^+p} < 1500$ OR $m_{K^+p} > 1550$ $m_{pK^-} < 1640$ OR $m_{pK^-} > 1700$ $m_{K^+p} < 1640$ OR $m_{K^+p} > 1700$ $m_{pK^-} < 1780$ OR $m_{pK^-} > 1880$ $m_{K^+p} < 1780$ OR $m_{K^+p} > 1880$	Unchanged	All
$p > 0.3$ $\pi > 0.5$	$p < 0.3$ Unchanged	Unchanged $\pi < 0.5$

$B^0 \to K^+\pi^-\gamma$ in the $p\pi^-\gamma$ mass window are now being shifted, according to new fits to data. For simplicity, these new fits are not done simultaneously, although they keep the same components used in the simultaneous fit, with the exclusion of the peaking backgrounds.

In order to perform these new simplified fits to the data, we need to do new fits to some MC samples as well to account for changes in the mass shapes coming from the removal of the mass vetoes. The results of these fits to MC of the $p\pi^-\ \gamma$ mass variable are shown in Figure 5.17, with the fits to data being in Figure 5.18. The values of the parameters resulting from the fit are shown in Table 5.20. The key point here is the differences between the means (μ) of the MCs and the corresponding data, which provide an estimation of the differences between both. These differences are then used to repeat the simultaneous fit twice (Figure 5.19), applying a shift-up and a shift-down to the means of the $B^0 \to K^+\pi^-\gamma$ and $\Lambda_b^0 \to pK^-\gamma$ distributions:

$$\mu_\pm = \mu_{MC} \pm |\mu'_{data} - \mu'_{MC}| \tag{5.17}$$

Where μ' are the means obtained from the fits using the cuts shown in Table 5.19.

Each simultaneous fit then provides two new values of the signal yield (and the normalisation yield, but it is a second-order effect), $N^\pm_{p\pi^-\gamma}$, from which we compute the systematic uncertainty:

$$\delta_R(N_{p\pi^-\gamma}) = \frac{\left|N^+_{p\pi^-\gamma} - N^-_{p\pi^-\gamma}\right|}{N^+_{p\pi^-\gamma} + N^-_{p\pi^-\gamma}} \tag{5.18}$$

Which results in $\delta_R(N_{p\pi^-\gamma}) = 3.0\%$.

After studying the effect of the mean, we focus on the impact of the width of the peaking backgrounds. For this task the process is much simpler, for which

Table 5.20: Results of the different fits of the $p\pi^-$ γ mass in MC and data, using the modified cut selection introduced in Table 5.19.

Sample	Parameter	Value
$B^0 \to K^+\pi^-\gamma$ MC	$\mu(\,\mathrm{MeV})$	5455.6 ± 1.1
	$\sigma(\,\mathrm{MeV})$	103.4 ± 1.0
	α_L	2.66 ± 0.09
	n	1.1 ± 0.2
	α_R	0.877 ± 0.015
$B^+ \to K^+\pi^-\pi^+\gamma$ MC	$\mu(\,\mathrm{MeV})$	5121 ± 17
	$\sigma(\,\mathrm{MeV})$	158 ± 22
	α_L	0.36 ± 0.07
	α_R	1.10 ± 0.19
$K\pi$ γ data	$\mu(B^0 \to K^+\pi^-\gamma)(\,\mathrm{MeV})$	5449 ± 2
	$\sigma(B^0 \to K^+\pi^-\gamma)(\,\mathrm{MeV})$	102 ± 2
	$N(B^0 \to K^+\pi^-\gamma)$	6860 ± 120
	$\tau(Comb)(\cdot 10^{-3}\,\mathrm{MeV}^{-1})$	-1.66 ± 0.02
	$N(Comb)$	13900 ± 200
	$N(B^+ \to K^+\pi^-\pi^+\gamma)$	1030 ± 190
$\Lambda_b^0 \to pK^-\gamma$ MC	$\mu(\,\mathrm{MeV})$	5501 ± 2
	$\sigma(\,\mathrm{MeV})$	96 ± 2
	α_L	1.18 ± 0.07
	n_L	11 ± 3
	α_R	1.69 ± 0.15
	n_R	7 ± 3
pK γ data	$\mu(\Lambda_b^0 \to pK^-\gamma)(\,\mathrm{MeV})$	5518 ± 4
	$\sigma(\Lambda_b^0 \to pK^-\gamma)(\,\mathrm{MeV})$	92 ± 4
	$N(\Lambda_b^0 \to pK^-\gamma)$	1140 ± 40
	$\tau(Comb)(\cdot 10^{-3}\,\mathrm{MeV}^{-1})$	-1.55 ± 0.08
	$N(Comb)$	960 ± 40

we repeat the simultaneous fit first by increasing and then by decreasing the value of the width of the peaking backgrounds in the $p\pi\gamma$ mass, by an amount three times the uncertainty measured in the MC. This number is taken not only to take into account the uncertainty of the measurement in simulation, but also to account for incompatibilities between data and simulation. The results of these two new simultaneous fits on the $p\pi\gamma$ mass are shown in Figure 5.20, which show just a minor effect on the signal yield as for Equation 5.18, with $\delta_R^{\sigma}(N_{p\pi\gamma}) = 0.41\%$.

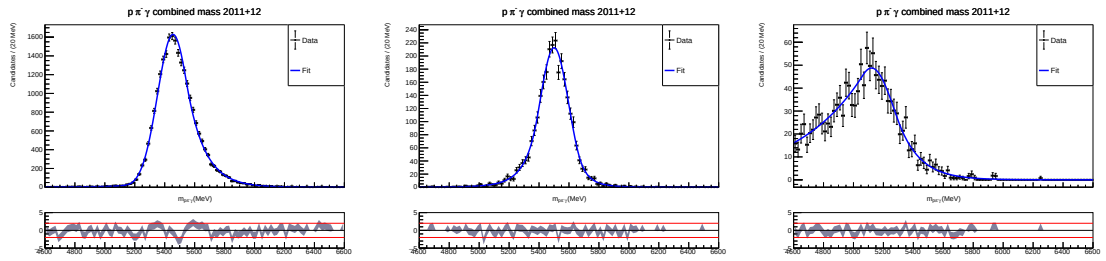

(a) (b) (c)

Figure 5.17: Fits to the $p\pi^-$ γ mass to MC samples of Figure 5.17a: $B^0 \to K^{*0}\gamma$ and $B^0 \to K_2^{*0}(1430)\gamma$, Figure 5.17b: $\Lambda_b^0 \to pK^-\gamma$, Figure 5.17c: $B^+ \to (K_1^+(1270) \to K^+\pi^-\pi^+)\gamma$, $B^+ \to (K_1^+(1400) \to K^+\pi^-\pi^+)\gamma$ and $B^+ \to K_2^{*+}(1430) \to K^+\pi^-\pi^+\gamma$.

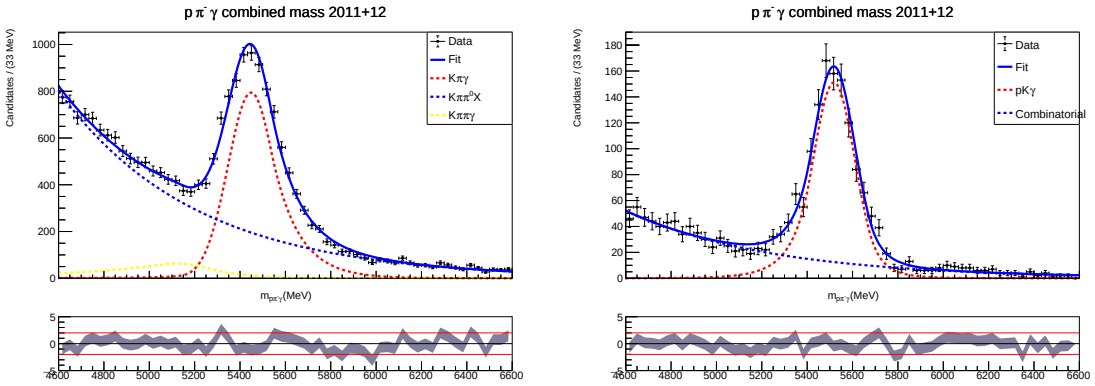

(a) (b)

Figure 5.18: Fits to the $p\pi^-$ γ mass to data samples using the modified cuts from Table 5.19: $K^+\pi^-$ γ, Figure 5.18a and pK^- γ modification, Figure 5.18b.

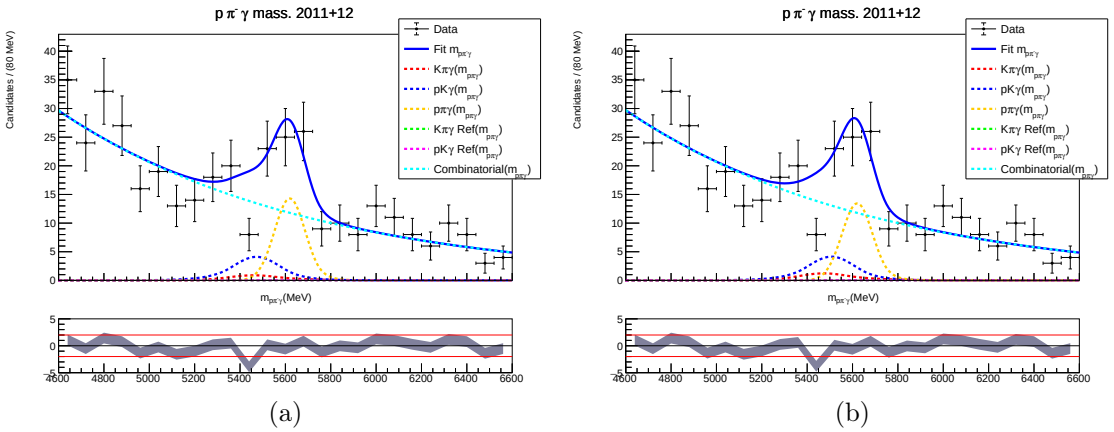

(a) (b)

Figure 5.19: Result of the simultaneous fit shifting the peaking backgrounds to the left Figure 5.19a and to the right Figure 5.19b. Only the $p\pi^-$ γ mass variable is shown, as the changes in the other projections are negligible.

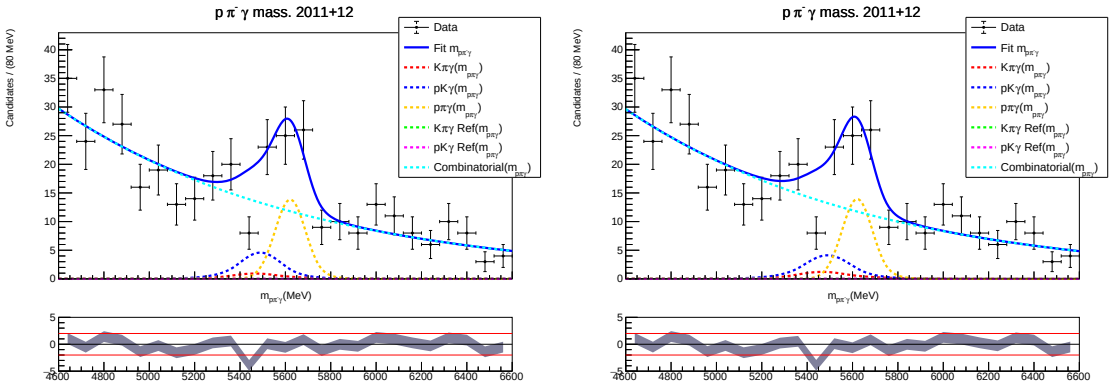

(a) (b)

Figure 5.20: Result of the simultaneous fit decreasing the peaking backgrounds width Figure 5.20a and increasing them Figure 5.20b. Only the $p\pi$ γ mass variable is shown, as the changes in the other projections are negligible.

5.7.2 Alternative reweighting

It is discussed in section 5.2 the reweighting applied on the signal and normalisation MC samples. The aim is to represent in a more accurate way the dihadron mass distributions, since the original samples reproduce the decay of a Λ_b^0 into $p\pi^-$ γ or pK^- γ, respectively, according to a phase space model. This discrepancy results in the dihadron masses to widely populate high mass values, around 3-5 GeV, while the n^* and Λ^{*0} resonances have masses around 1-2 GeV.

In this section we use a different binning scheme for both the signal and normalisation simulation samples. For the signal sample, 15 equally populated bins for the $p\pi$ mass are used instead of 25, and 30 equally populated bins for the Λ_b^0 p_{T} instead of 100. The normalisation sample is reweighted using 15 bins in each variable instead of 25. Using these new weights, the ratio of efficiencies in Equation 5.15 is re-evaluated, and the difference with the standard configuration is treated as a systematic uncertainty.

In Table 5.21 it is presented the difference in the ratio of efficiencies between the standard and alternative reweighting configurations, broken down in three blocks:

- FullEvt: Related to the change in efficiency of the FullEvt cut.
- Offline: Related to the change in efficiency of the offline selection: preselection, BDT selection and mass vetoes, excluding the PID.
- PID: Related to the change in efficiency of the PID selection.

We also present in Figure 5.21 and Figure 5.22 the comparison between the *sWeighted* datasets and the alternatively reweighted MC, with all the other dihadron mass combinations contained in Figure A.6 and Figure A.7, showing that the different mass variables are still properly reproduced even in this case with fewer bins.

Table 5.21: Relative uncertainties coming from the use of an alternative reweighting strategy.

$\delta_R(\epsilon_{FullEvt})(\%)$	$\delta_R(\epsilon_{Offline})(\%)$	$\delta_R(\epsilon_{PID})(\%)$	$\delta_R(Reweight)(\%)$
2.4	1.8	0.9	3.1

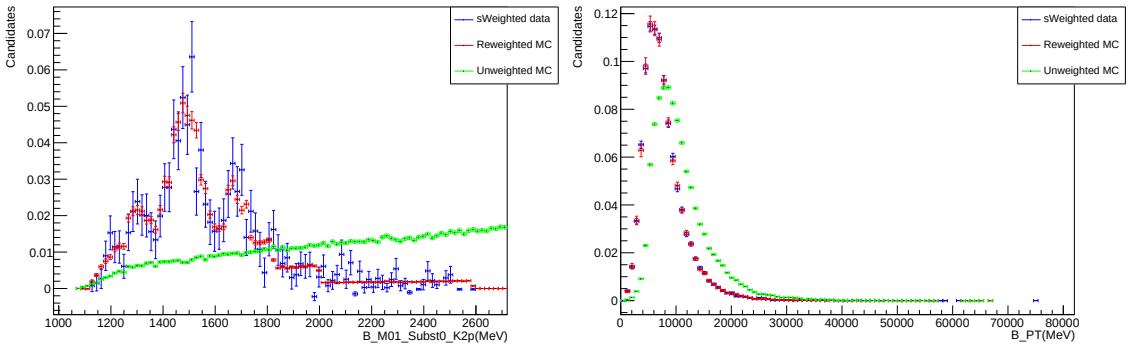

(a) (b)

Figure 5.21: Comparison of the $p\pi$ mass (a) and Λ_b^0 p_{T} (b) distributions between *sWeighted* data (blue) and the signal MC, both unweighted (green) and reweighted with fewer bins (red). *sWeighted* $\Lambda_b^0 \to p\pi^- J/\psi$ data is used in (a) and *sWeighted* $\Lambda_b^0 \to pK^- J/\psi$ data is used in (b).

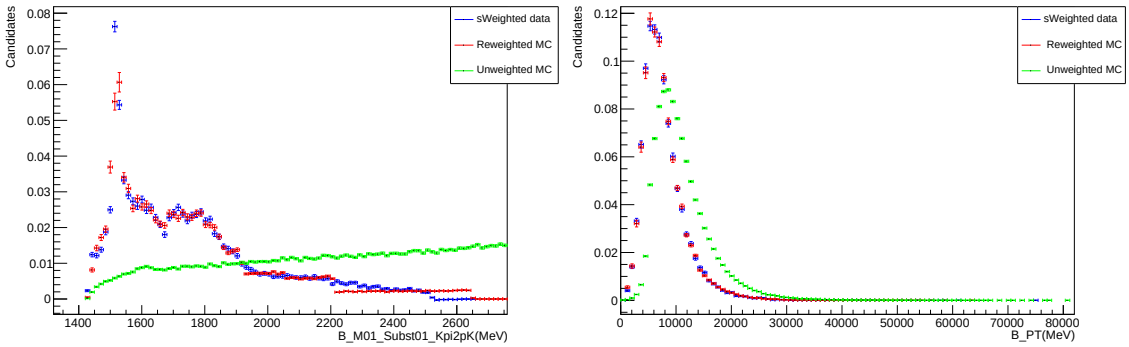

(a) (b)

Figure 5.22: Comparison of the pK mass (a) and Λ_b^0 p_{T} (b) distributions between *sWeighted* $\Lambda_b^0 \to p\pi^- J/\psi$ data (blue) and the signal MC, both unweighted (green) and reweighted with fewer bins (red).

5.7.3 Finite sample size

Another important source of systematic uncertainty arises from the fact that the samples used to compute the different efficiencies have a finite size. This uncertainty is obtained from the binomial distribution, where the probability of an event to pass a certain selection is the efficiency:

$$\delta(\epsilon) = \sqrt{\frac{\epsilon(1-\epsilon)}{N_0}} \tag{5.19}$$

Where N_0 is the total number of events in the sample, before the selection. This expression can be generalised if the sample is weighted, which is the case for the $\Lambda_b^0 \to p\pi^-\gamma$ and $\Lambda_b^0 \to pK^-\gamma$ samples:

$$\delta(\epsilon) = \sqrt{\epsilon(1-\epsilon)\frac{\sum_{i=1}^{N} w_i^2}{\left(\sum_{i=1}^{N} w_i\right)^2}} \tag{5.20}$$

Therefore, the larger the sample size, the smaller the uncertainty associated. This results in the latest efficiencies to have a larger error, as the samples have already been filtered in the previous selection steps. This is the way the systematic uncertainties have been computed for all the quoted efficiencies, with the exception of the PID efficiency, that has been treated in a special way.

As it has been noted in subsection 5.3.5, the PID efficiency is not directly computed with the simulated PID variables, but some calibration data samples containing the relevant particles are used instead. Therefore, to obtain the systematic uncertainty associated, we compute the PID efficiency 3 times. In each iteration, a different portion of the calibration data sample is used to compute the efficiency per bin of p_{T} and η, thus providing 3 independent measurements of the PID efficiency, ϵ_{PID_i}, with their respective uncertainty, obtained with Equation 5.20. The final measure of the PID efficiency is then the result of averaging the 3 efficiencies obtained:

$$\epsilon_{PID} = \frac{1}{3}\sum_{i=1}^{3} \epsilon_{PID_i} \tag{5.21}$$

Since the uncertainty of each measurement almost only depends on the MC, which is always the same, the first source of uncertainty for the PID comes from the MC and follows Equation 5.20:

$$\delta_1(\epsilon_{PID}) = \delta(\epsilon_{PID}) \tag{5.22}$$

A second uncertainty can be obtained using the Standard Error of the Mean (SEM), to take into account the finite size of the calibration data used to evaluate the PID efficiencies in bins of p_{T} and η:

$$\delta_2(\epsilon_{PID}) = \frac{\sigma}{\sqrt{3}} = \sqrt{\frac{\sum_{i=1}^{3}(\epsilon_{PID_i} - \epsilon_{PID})^2}{3(3-1)}} \tag{5.23}$$

Table 5.22: Relative uncertainties, in percentage, for the different efficiencies reported. The total uncertainties are the quadratic sum of their components.

Decay mode	Gen	FullEvt	R+T+S	Offline	PID	Total (%)
$\Lambda_b^0 \to p\pi^-\gamma$	0.6	0.5	0.2	4.2	4.4	5.2
$\Lambda_b^0 \to pK^-\gamma$	0.11	0.6	0.17	3.4	2.8	3.9
Total	0.6	0.8	0.3	5.4	5.2	7.6

The final PID uncertainty is therefore the quadratic sum of these two:

$$\delta(\epsilon_{PID}) = \sqrt{\delta_1^2(\epsilon_{PID}) + \delta_2^2(\epsilon_{PID})} \tag{5.24}$$

This way, one captures both the uncertainty from having a finite size MC sample and a finite size also in the calibration sample. The summary for all these uncertainties related to the sample size is shown in Table 5.22.

5.7.4 Differences between 2011 and 2012

The 2011 and 2012 data samples have been treated together, taking 2012 simulation samples as reference to compute the relevant efficiencies. Despite both years being similar, two main differences exist: first, the centre-of-mass energy in 2011 was 7 GeV, while it was raised to 8 GeV in 2012, which would mean that more energetic particles are present in the latter year. Secondly, the L0 trigger configuration changed between years, with the `L0Photon` and `L0Electron` γ p_{T} threshold being set at ∼2500 MeV for 2011 and at ∼2720 MeV for 2012. These thresholds correspond to the TCK (Trigger Configuration key) with which the most luminosity was recorded in each year, with finer tuning present between different TCKs of the same year. A TCK is a unique 32-bit value which labels the sequence of algorithms and cuts used in the HLT configuration. A γ p_{T} cut of 3000 MeV has been applied at the offline preselection stage Table 5.9 to minimise these differences.

In order to assess how differences affect the calculation of the BR, the nominal value, obtained with 2012 simulation samples, is compared with a value obtained using 2011 and 2012 efficiencies separately. Measuring 2011 and 2012 efficiencies separately, the BR now reads:

$$\left.\frac{\mathcal{B}(\Lambda_b^0 \to p\pi^-\gamma)}{\mathcal{B}(\Lambda_b^0 \to pK^-\gamma)}\right|_{2011\neq2012} = \frac{N_{p\pi\gamma}}{N_{pK\gamma}} \frac{\mathcal{L}_{2011}\sigma_{2011}\epsilon^{2011}_{\Lambda_b^0\to pK^-\gamma}(p\bar{\pi}) + \mathcal{L}_{2012}\sigma_{2012}\epsilon^{2012}_{\Lambda_b^0\to pK^-\gamma}(p\bar{\pi})}{\mathcal{L}_{2011}\sigma_{2011}\epsilon^{2011}_{\Lambda_b^0\to p\pi^-\gamma} + \mathcal{L}_{2012}\sigma_{2012}\epsilon^{2012}_{\Lambda_b^0\to p\pi^-\gamma}(p\pi)} \tag{5.25}$$

Where $\mathcal{L}$ and σ are the luminosities and $b\bar{b}$ cross-sections for each year, respectively. Notice that in the case the efficiencies for 2011 and 2012 are equal, we recover Equation 5.15. Now, since $\mathcal{L}_{2012} \approx 2\mathcal{L}_{2011}$ and assuming $\sigma_{2011} = \sigma_{2012}$, which is safe to do because the cross-section in 2012 is actually higher, the systematic uncertainty related to differences between 2011 and 2012 can be written as:

Table 5.23: 2011 simulation samples used in the evaluation of the systematic uncertainty associated to differences between 2011 and 2012. The amount of candidates corresponds to the number of entries in the ntuple, this is, the number of events accepted by the `B2XGamma2pi` stripping line, times the multiplicity.

Decay mode	Event type	Reco	EvtGen	Candidates
$\Lambda_b^0 \to pK^-\gamma$	15102215	`Reco14c`	`Sim09i`− `ReDecay01`	637888
$\Lambda_b^0 \to p\pi^-\gamma$	15102250	`Reco14c`	`Sim09k`− `ReDecay01`	1838550

$$
\begin{aligned}
\delta_R(2011 \neq 2012) &\equiv \left| 1 - \left. \frac{\mathcal{B}(\Lambda_b^0 \to p\pi^-\gamma)}{\mathcal{B}(\Lambda_b^0 \to pK^-\gamma)} \right|_{2011\neq 2012} \left(\frac{\mathcal{B}(\Lambda_b^0 \to p\pi^-\gamma)}{\mathcal{B}(\Lambda_b^0 \to pK^-\gamma)} \right)^{-1} \right| \\
&= \left| 1 - \frac{\epsilon^{2011}_{\Lambda_b^0 \to pK^-\gamma}(p\bar{\pi}) + 2\epsilon^{2012}_{\Lambda_b^0 \to pK^-\gamma}(p\bar{\pi})}{\epsilon^{2011}_{\Lambda_b^0 \to p\pi^-\gamma}(p\pi) + 2\epsilon^{2012}_{\Lambda_b^0 \to p\pi^-\gamma}(p\pi)} \left(\frac{\epsilon^{2012}_{\Lambda_b^0 \to pK^-\gamma}(p\bar{\pi})}{\epsilon^{2012}_{\Lambda_b^0 \to p\pi^-\gamma}(p\pi)} \right)^{-1} \right| \\
&= \left| 1 - \frac{\epsilon^{2012}_{\Lambda_b^0 \to p\pi^-\gamma}(p\pi)}{\epsilon^{2011}_{\Lambda_b^0 \to p\pi^-\gamma}(p\pi)} \frac{\epsilon^{2011}_{\Lambda_b^0 \to pK^-\gamma}(p\bar{\pi})}{\epsilon^{2012}_{\Lambda_b^0 \to pK^-\gamma}(p\bar{\pi})} \right| \left(1 + 2\frac{\epsilon^{2012}_{\Lambda_b^0 \to p\pi^-\gamma}(p\pi)}{\epsilon^{2011}_{\Lambda_b^0 \to p\pi^-\gamma}(p\pi)} \right)^{-1}
\end{aligned}
\tag{5.26}
$$

The MC samples used to evaluate the 2011 efficiency of the normalisation mode are described in Table 5.23. The event types of the 2011 and 2012 versions of $\Lambda_b^0 \to pK^-\gamma$ MC are different, with the 2011 version rejecting events with a pK mass above 3150 MeV at generator level. However, this difference is taken care of with the offline preselection due to the effectively tighter cut applied on the $p\pi$ mass of 2200 MeV. An overall systematic uncertainty of 1.3% is assessed, mainly due to the differences in the kinematics between 2011 and 2012 that affect the evaluation of the offline selection efficiencies.

5.7.5 Systematic uncertainty summary

For completion, a summary of all the systematic uncertainties is presented in Table 5.24. The main source of systematic uncertainty comes from the finite sample size of the simulation, which is used to evaluate the efficiencies. We see a smaller sensitivity to the reweighting scheme, the position of the background peaks and the differences between 2011 and 2012, but it is important to measure how much they affect the result as they could have had a greater impact on the result. The uncertainties obtained, however, are well below the statistical uncertainty of the measurement, which is dominated by the low signal yield that can be extracted from the data.

Table 5.24: List of systematic relative uncertainties. The total uncertainty is the quadratic sum of all the sources.

Source	$\delta_R(\%)$
Peaking backgrounds shifts	3.0
Peaking backgrounds widths	0.4
Alternative reweighting	3.1
Sample size: Generator level	0.6
Sample size: Full event cut	0.8
Sample size: Reco+Trigger+Strip	0.3
Sample size: Offline	5.4
Sample size: PID	5.2
2011-2012 differences	1.3
Total	8.8

5.8 Results

The measurement of the branching ratio is presented here. First, from the result of the simultaneous fit in Table 5.18 we extract that we have found 30 $\Lambda_b^0 \to p\pi^-\gamma$ events and 407 $\Lambda_b^0 \to pK^-\gamma$ events (no uncertainties quoted). These numbers, combined with the ratio of efficiencies found in Equation 5.16 provide the branching ratio according to Equation 5.15:

$$\frac{\mathcal{B}(\mathbf{\Lambda_b^0 \to p\pi^-\gamma})}{\mathcal{B}(\mathbf{\Lambda_b^0 \to pK^-\gamma})} = [\mathbf{5.5 \pm 1.7 \pm 0.5}]\% \tag{5.27}$$

Where the first error is statistic, as it arises from the simultaneous fit to the data, and the second is systematic. This number is at the edge of a first observation of baryonic $b \to d\gamma$ decays in LHCb, and it is compatible within 1σ with the ratio of the CKM matrix elements $\left|\frac{V_{td}}{V_{ts}}\right|^2 = [4.7 \pm 0.3]\%$, which dictates the value of this branching ratio at first order.

The value of the $\Lambda_b^0 \to p\pi^-\gamma$ branching fraction cannot be yet extracted until a measurement of the one of $\Lambda_b^0 \to pK^-\gamma$ is performed, which is already under study in the LHCb collaboration. This could have also been achieved using $B^0 \to K^{*0}\gamma$ as the normalisation mode, but it would give rise to other sources of systematic uncertainties due to having different mother particles.

In any case, the result is dominated by the high statistical uncertainty, which is caused by the tight selection used to be able to separate $B^0 \to K^{*0}\gamma$ and $\Lambda_b^0 \to pK^-\gamma$ decays from the signal mode. In addition, having a photon as one of the decay products worsens the problem, as it is reconstructed with a much poorer resolution than tracked particles, for instance, a muon-antimuon pair. Therefore, adding Run 2 data to the analysis should reduce the overall uncertainty, since the systematic uncertainty is still four times smaller.

6 Conclusions

This thesis has presented my work in the LHCb experiment, which includes a search of a world's first near evidence of a baryonic $b \to d\gamma$ process, $\Lambda_b^0 \to p\pi^-\gamma$, and the first steps towards an inclusive radiative trigger in Run 3. This inclusive trigger has allowed for a wide variety of radiative decays to be studied in Run 2 and aims to play a key role in Run 3 as it will be able to keep selecting radiative decays without the need to develop a selection for every single decay topology.

The upgrade of the LHCb detector pushes the limit of both the hardware and software equipment. In the hardware side, most of the electronics will be replaced and improved once the Run 3 data-taking begins in 2022, in order to cope with the increased luminosity and frequency at which the detector will have to operate. The main challenge, which is the removal of the hardware trigger stage, means that the detector has to increase its operating frequency from 1 MHz to 40 MHz. This change also affects the software trigger stage, which needs to see its execution time reduced and be more precise on the information that is saved to disk. Such increase in performance will be provided by the implementation of GPUs, which are a powerful tool when dealing with parallelised processes, and by saving only the decay of interest instead of the whole event. The latter change in particular hurts the inclusive radiative trigger strategy that was implemented in Run 2, where either two- or three- body decays plus a photon were searched, keeping the whole underlying event to perform any other combination. In Run 3, the strategy has to be revisited in order to save only the interesting parts of the event, at the price of an increased bandwidth. We have shown that such strategy can be implemented, although it still requires finer tuning through the study of the properties of other radiative decays.

On the other hand, study of radiative decays is of importance because they are driven by FCNC, which are suppressed in the SM and are sensitive to NP effects. LHCb has been able to provide measurements of $b \to s\gamma$ and $b \to d\gamma$ processes in mesons, while only the branching fraction of $\Lambda_b^0 \to \Lambda\gamma$ has been measured up to this date using baryons. In this sense, the search for the $\Lambda_b^0 \to p\pi^-\gamma$ decay aims to continue the study of radiative decays, although it has proved to be a hard task. First, the contamination from more common FCNC processes masks the signal region, so it has to be dealt with a tighter selection and the implementation of a simultaneous mass fit to have as much control as possible over its effect. To this, the poor resolution of the reconstructed photon is added, making every main peaking background contribution to overlap.

Nevertheless, using the Run 1 data collected by LHCb has been enough to get a near evidence of the $\Lambda_b^0 \to p\pi^-\gamma$ decay, with a measurement of the Branching Ratio of:

$$\frac{\mathcal{B}(\Lambda_b^0 \to p\pi^-\gamma)}{\mathcal{B}(\Lambda_b^0 \to pK^-\gamma)} = [5.5 \pm 1.7(\text{stat.}) \pm 0.4(\text{syst.})]\,\% \tag{6.1}$$

where the first uncertainty is statistical and the second is systematic. This corresponds to a 3.2σ measurement, which shows the first evidence of this decay. The result is dominated by the statistical uncertainty, so the addition of Run 2 data will reduce its contribution. However, this addition cannot be done trivially, as there are other systematic effects playing its part in Run 2, which must be studied and accounted before being added to the analysis. As a result, it has not been possible to add Run 2 data to this thesis.

To summarise, this thesis has studied the performance and viability of an inclusive radiative trigger for Run 3 in LHCb, as well as searched for the $\Lambda_b^0 \to p\pi^-\gamma$ decay, to provide a further insight on the goodness of the predictions of the SM for FCNC processes.

A Appendix

A.1 Dalitz plots

Here we present a total of 30 Dalitz plots for each pair of dihadron masses. Figure A.1 corresponds to run I data after applying the kinematic selection (no vetoes), while Figure A.2 has the vetoes added. These allow for a better identification of the resonances and the effect of the mass vetoes on the other mass combinations.

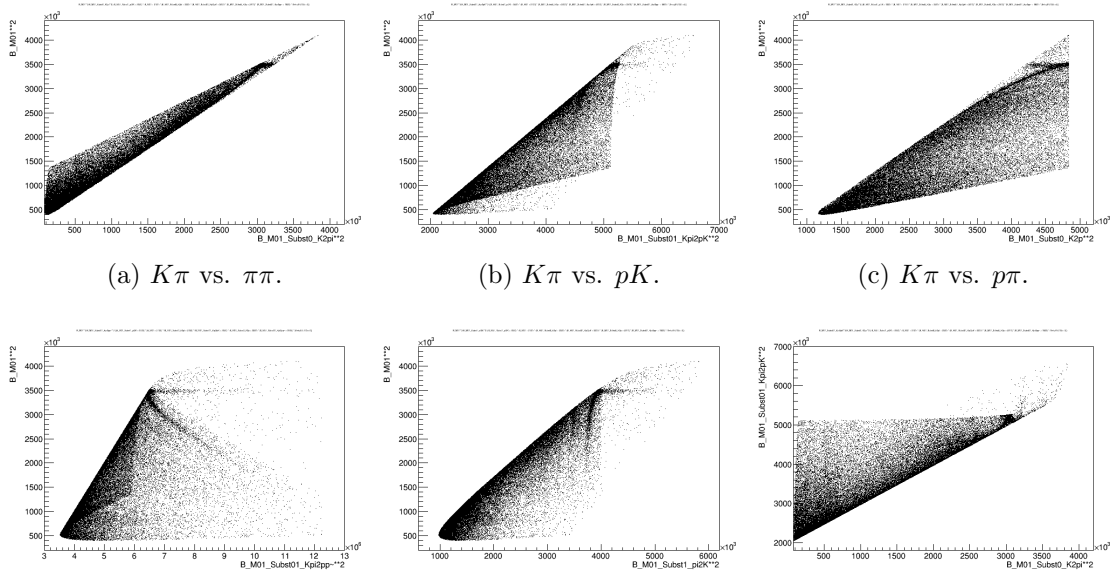

(a) $K\pi$ vs. $\pi\pi$. (b) $K\pi$ vs. pK. (c) $K\pi$ vs. $p\pi$.

(d) $K\pi$ vs. pp. (e) $K\pi$ vs. KK. (f) pK vs. $\pi\pi$.

Figure A.1: Mass correlation plots for all combinations of dihadron mass hypotheses before vetoes (y-axis vs. x-axis).

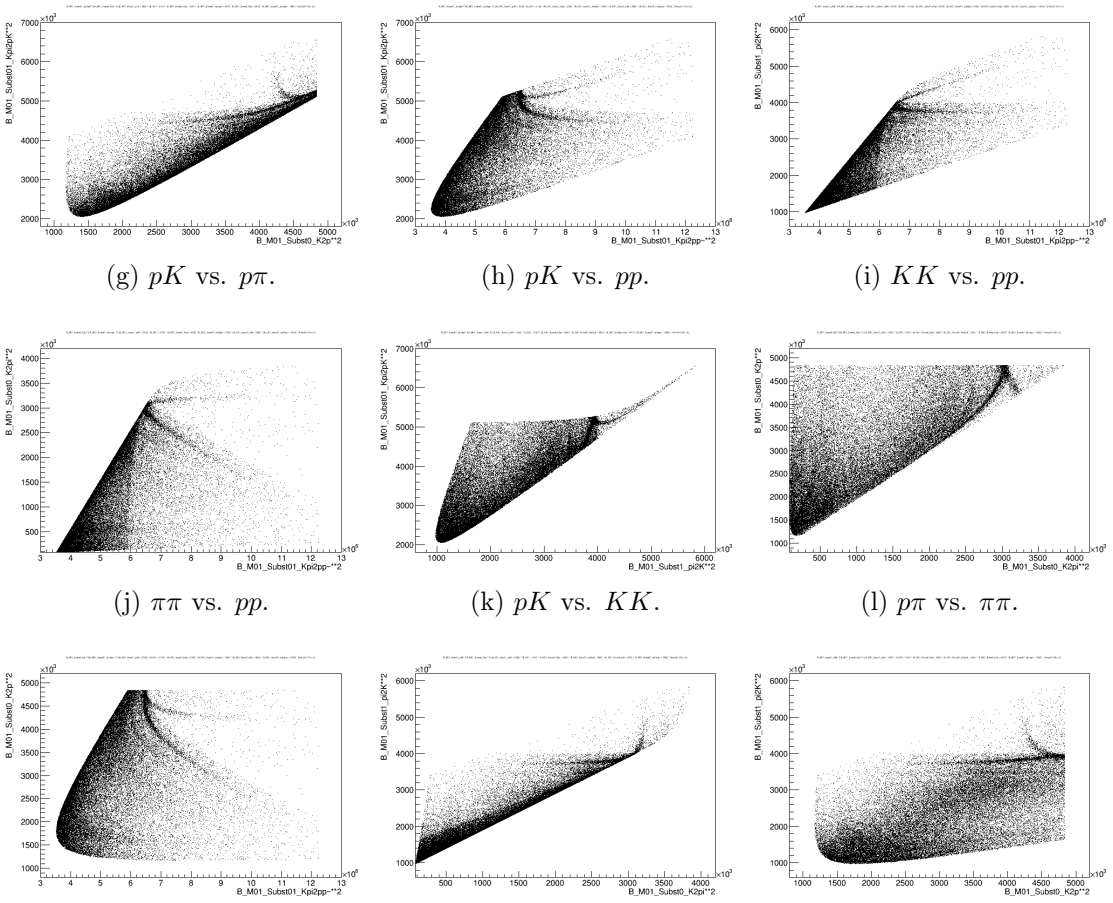

(g) pK vs. $p\pi$. (h) pK vs. pp. (i) KK vs. pp.

(j) $\pi\pi$ vs. pp. (k) pK vs. KK. (l) $p\pi$ vs. $\pi\pi$.

(m) $p\pi$ vs. pp. (n) KK vs. $\pi\pi$. (o) KK vs. $p\pi$.

Figure A.1: (Cont.) Mass correlation plots for all combinations of dihadron mass hypotheses before vetoes (y-axis vs. x-axis).

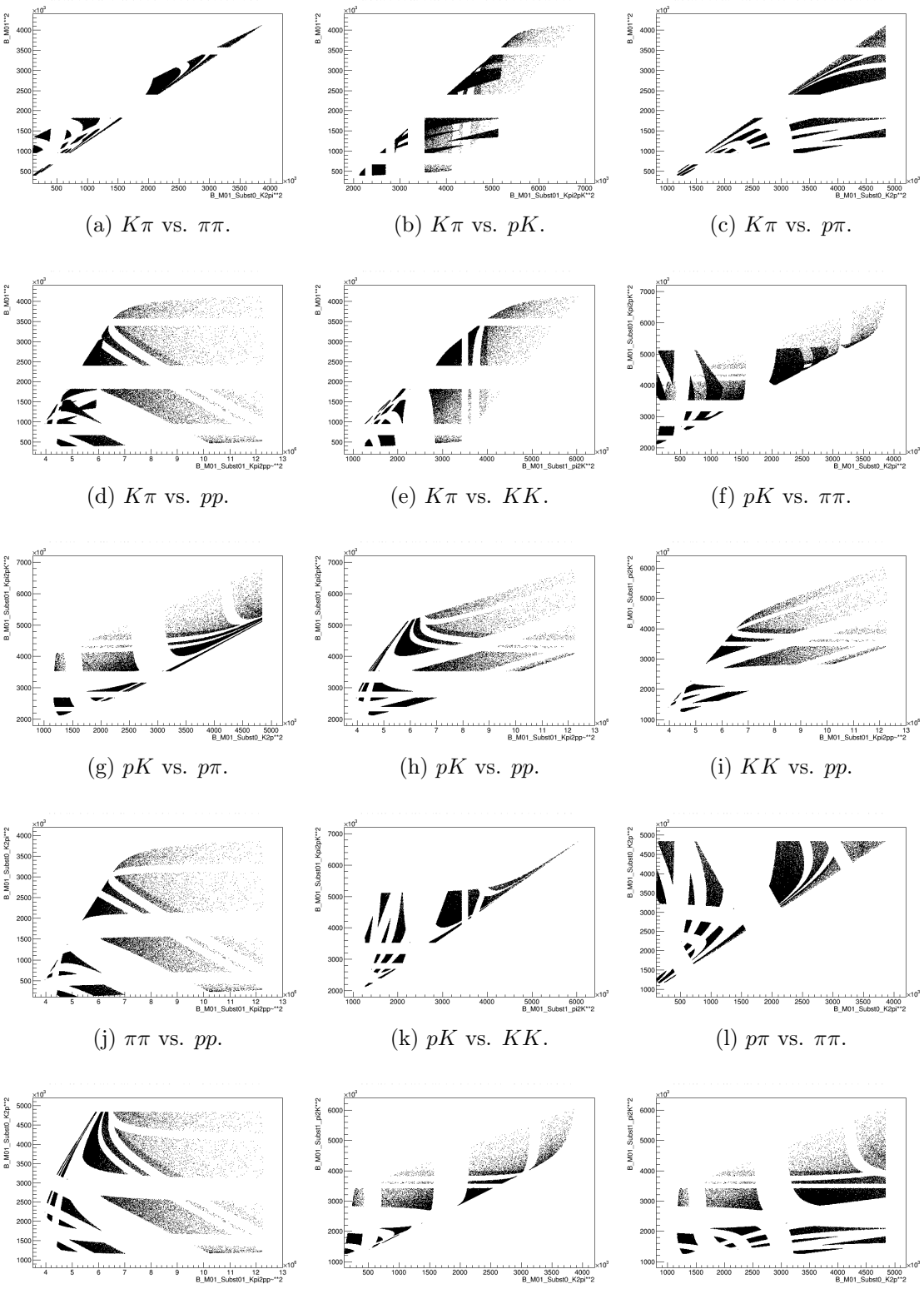

(a) $K\pi$ vs. $\pi\pi$. (b) $K\pi$ vs. pK. (c) $K\pi$ vs. $p\pi$.

(d) $K\pi$ vs. pp. (e) $K\pi$ vs. KK. (f) pK vs. $\pi\pi$.

(g) pK vs. $p\pi$. (h) pK vs. pp. (i) KK vs. pp.

(j) $\pi\pi$ vs. pp. (k) pK vs. KK. (l) $p\pi$ vs. $\pi\pi$.

(m) $p\pi$ vs. pp. (n) KK vs. $\pi\pi$. (o) KK vs. $p\pi$.

Figure A.2: Mass correlation plots for all combinations of dihadron mass hypotheses after vetoes (y-axis vs. x-axis).

A.2 Reweighted dihadron masses

The reweighting of both the signal and normalisation modes is done using the correct dihadron mass hypothesis. It is shown here the distributions of the other relevant dihadron mass hypotheses before and after the reweighting, compared with the *sWeighted* reference sample.

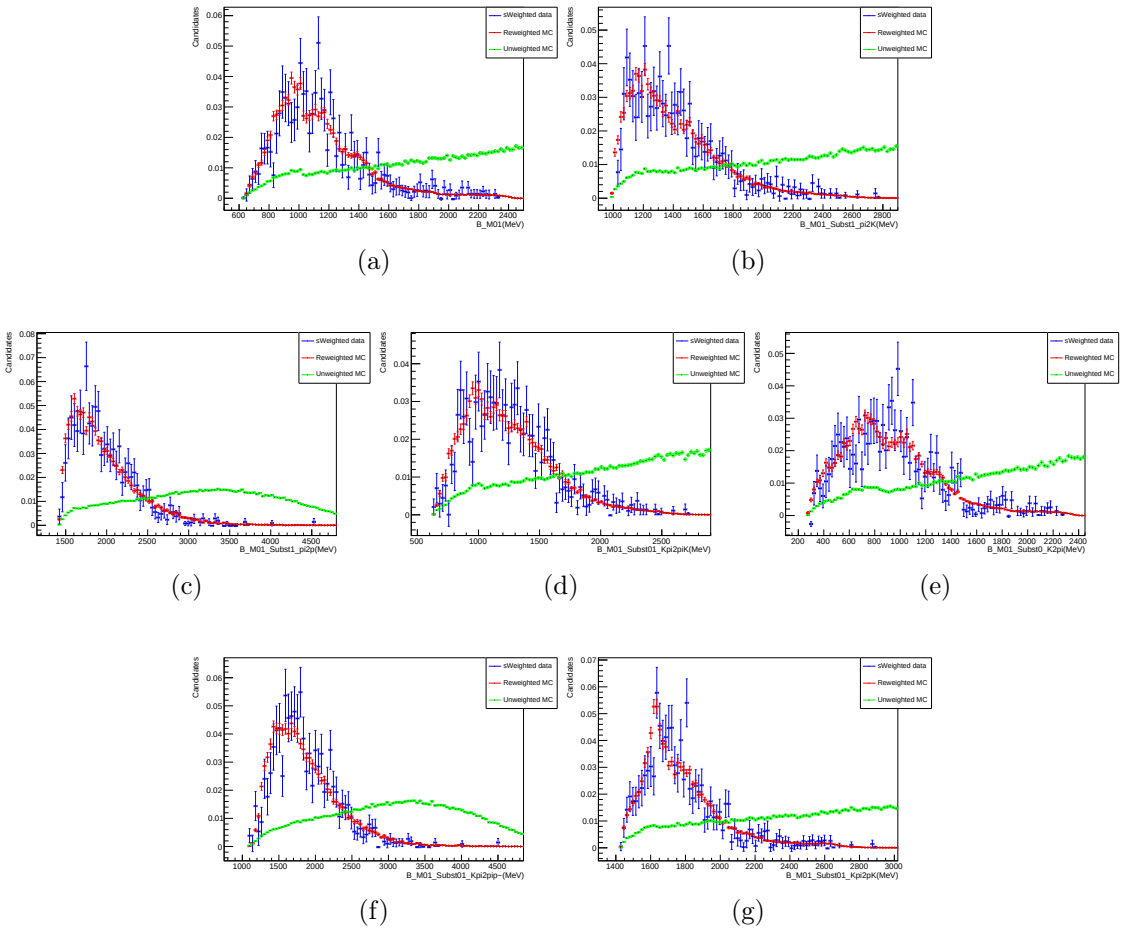

(a) (b)

(c) (d) (e)

(f) (g)

Figure A.3: Comparison of the dihadron mass distributions between *sWeighted* $\Lambda_b^0 \to p\pi^- J/\psi$ data (blue), unweighted (green) and reweighted signal MC (red). The different mass variables are: $K^+\pi^-$ (a), K^+K^- (b), $K^+\overline{p}$ (c), π^+K^- (d), $\pi^+\pi^-$ (e), $\pi^+\overline{p}$ (f), pK^- (g).

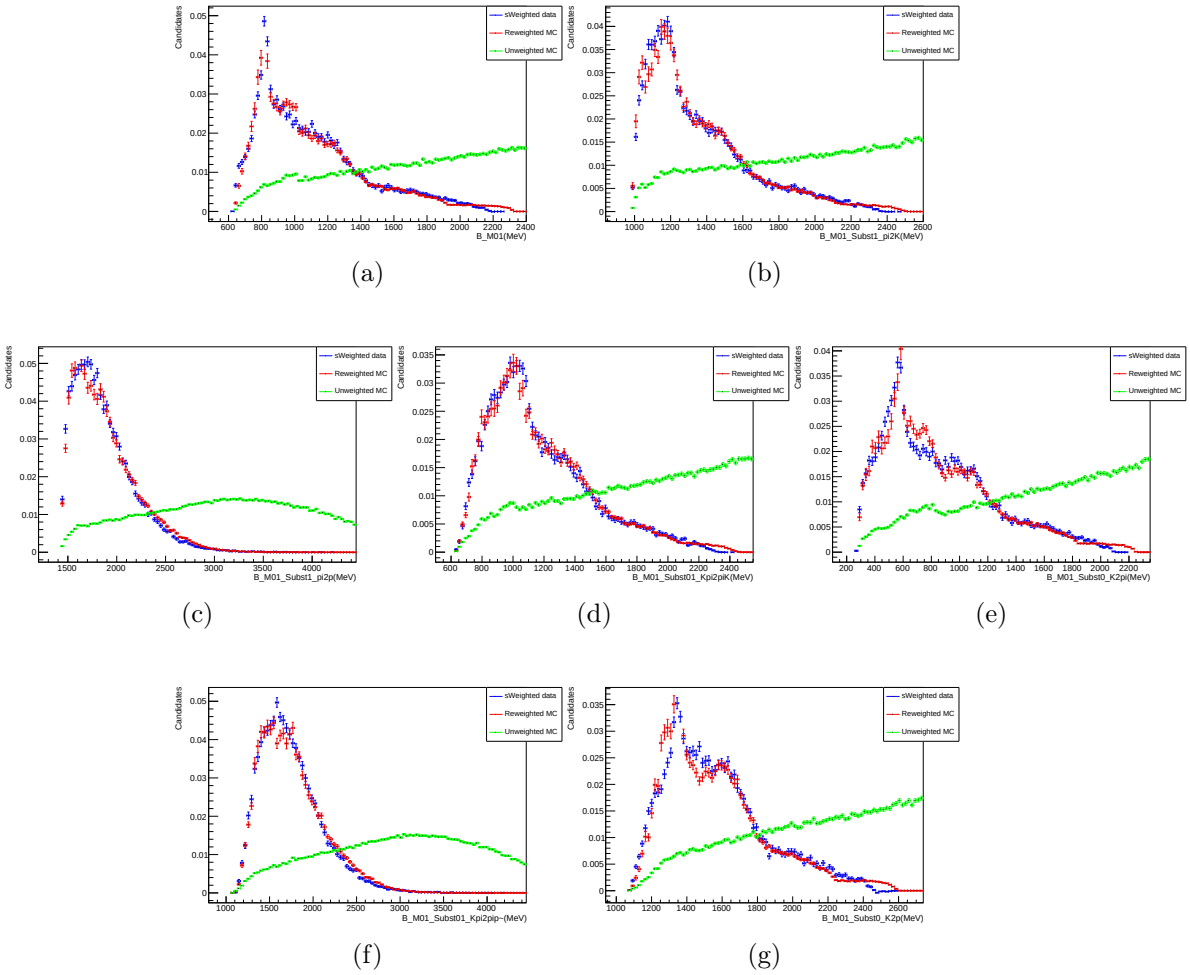

(a) (b) (c) (d) (e) (f) (g)

Figure A.4: Comparison of the dihadron mass distributions between *sWeighted* $\Lambda_b^0 \to pK^-J/\psi$ data (blue), unweighted (green) and reweighted signal MC (red). The different mass variables are: $K^+\pi^-$ (a), K^+K^- (b), $K^+\overline{p}$ (c), π^+K^- (d), $\pi^+\pi^-$ (e), $\pi^+\overline{p}$ (f), $p\pi^-$ (g).

A.3 BDT variables

Figure A.5 shows the comparison between $\Lambda_b^0 \to pK^-\gamma$ in MC and *sWeighted* data of the variables used to train the kinematic BDT.

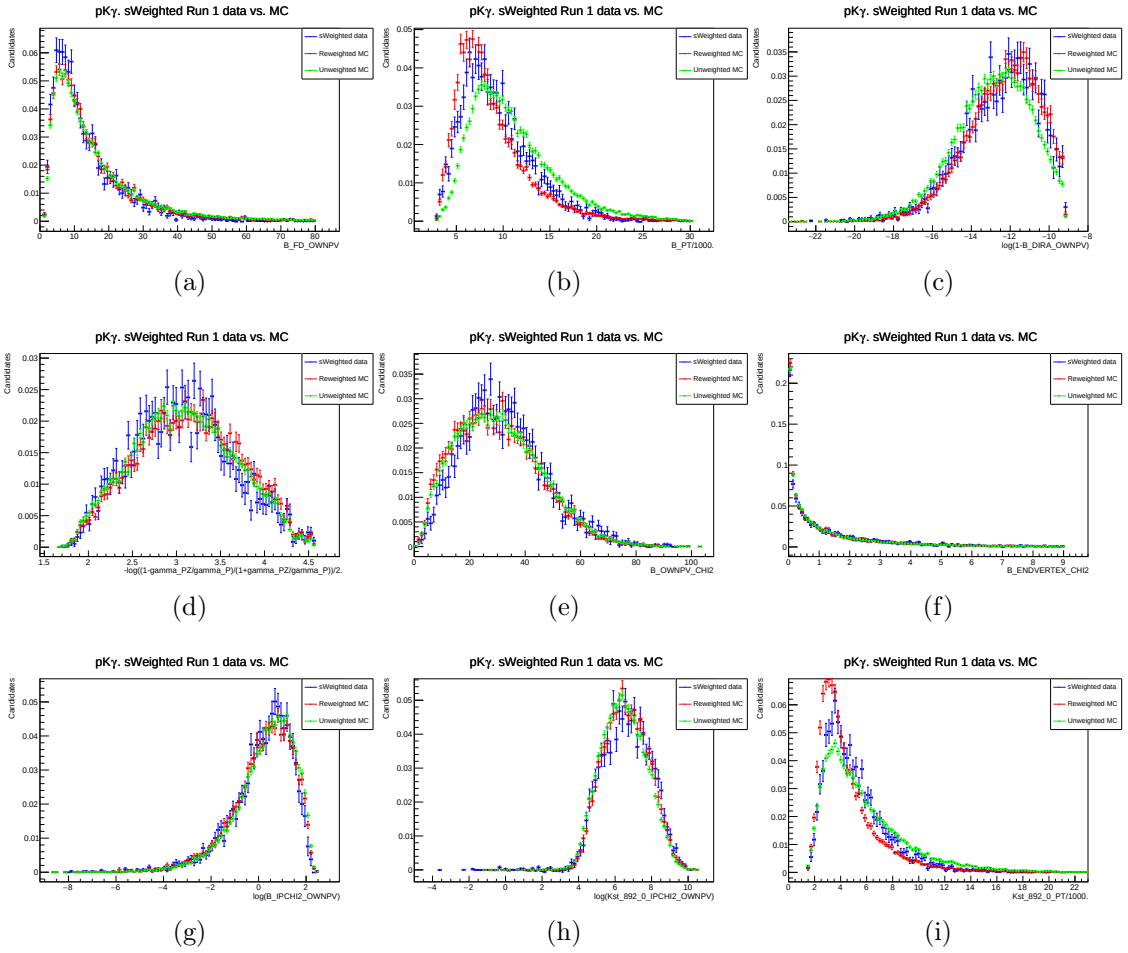

(a) (b) (c)

(d) (e) (f)

(g) (h) (i)

Figure A.5: Distribution of the BDT variables for *sWeighted* $\Lambda_b^0 \to pK^-\gamma$ data (blue), unweighted (green) and reweighted (red) $\Lambda_b^0 \to pK^-\gamma$ MC. Λ_b^0 flight distance (mm) (a), Λ_b^0 p_{T} (GeV) (b), $\log(1 - \Lambda_b^0$ Direction Angle) (c), γ_η (d), Λ_b^0 χ^2_{PV} (e), Λ_b^0 χ^2_{EV} (f), $\log(\Lambda_b^0 \chi^2_{\mathrm{IP_{PV}}})$ (g), $\log(\Lambda^{*0} \chi^2_{\mathrm{IP_{PV}}})$ (h), Λ^{*0} p_{T} (GeV) (i).

A.4 Alternatively reweighted dihadron masses

The alternative reweighting of both the signal and normalisation modes is done using the correct dihadron mass hypothesis. It is shown here the distributions of the other relevant dihadron mass hypotheses before and after the reweighting, compared with the *sWeighted* reference sample.

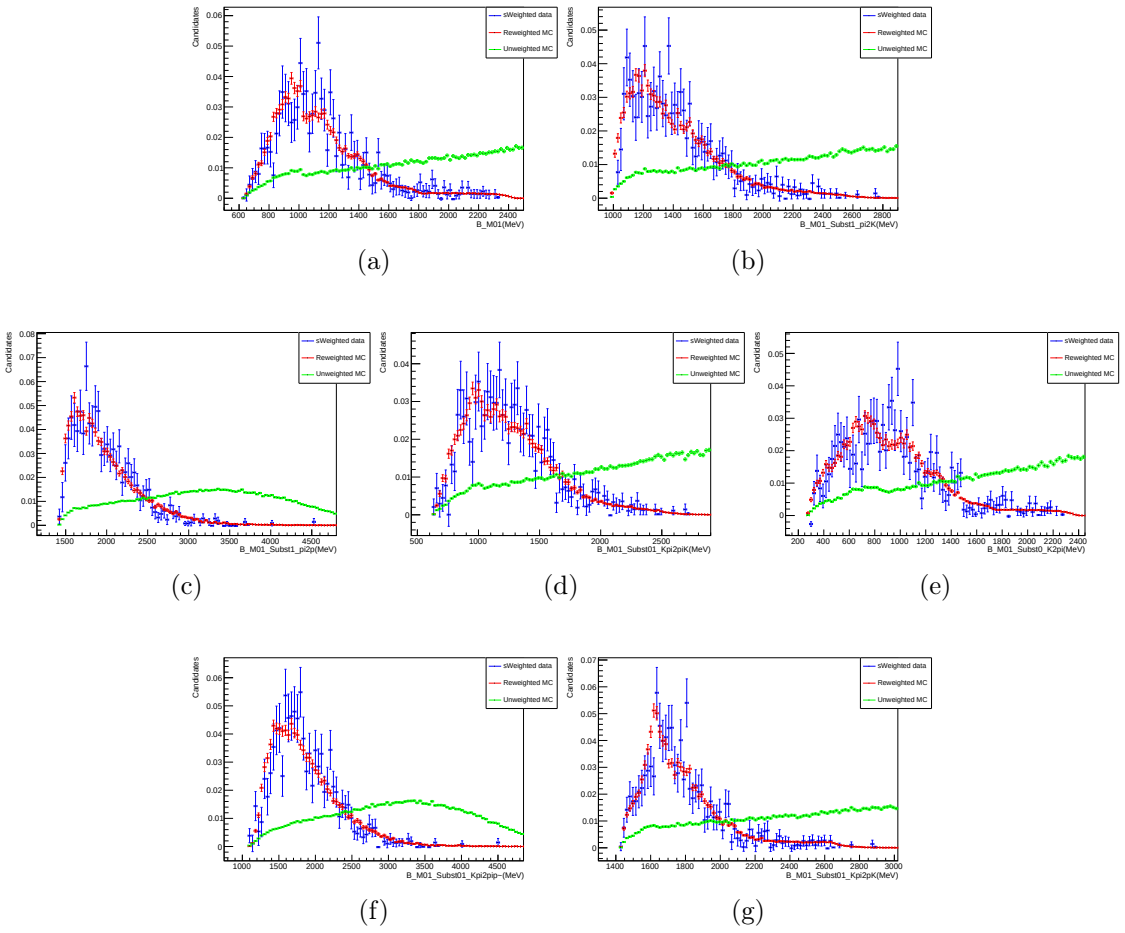

Figure A.6: Comparison of the dihadron mass distributions between *sWeighted* $\Lambda_b^0 \to p\pi^- J/\psi$ data (blue), unweighted (green) and reweighted signal MC (red), using the alternative reweighting. The different mass variables are: $K^+\pi^-$ (a), K^+K^- (b), $K^+\overline{p}$ (c), π^+K^- (d), $\pi^+\pi^-$ (e), $\pi^+\overline{p}$ (f), pK^- (g).

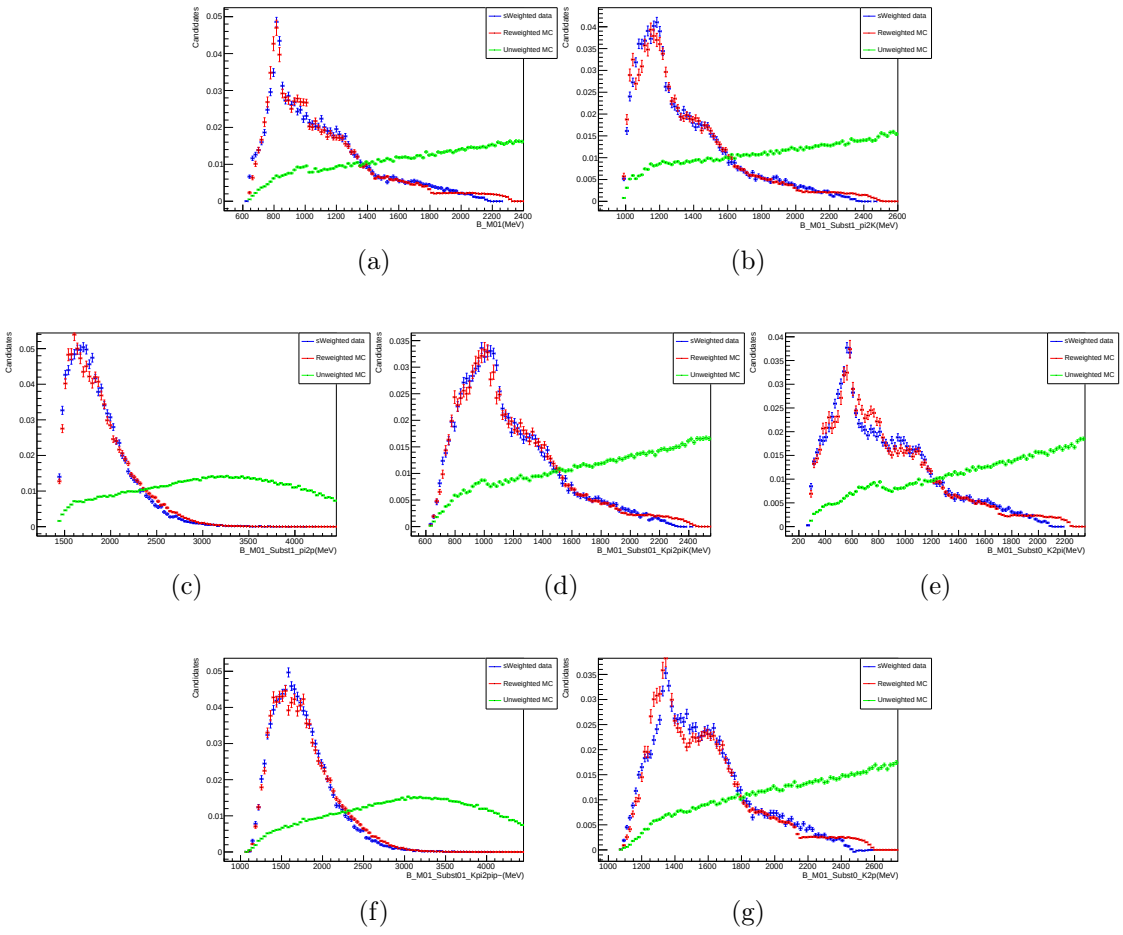

(a) (b) (c) (d) (e) (f) (g)

Figure A.7: (Cont.) Comparison of the dihadron mass distributions between *sWeighted* $\Lambda_b^0 \to pK^-J/\psi$ data (blue), unweighted (green) and reweighted normalisation MC (red), using the alternative reweighting. The different mass variables are: $K^+\pi^-$ (a), K^+K^- (b), $K^+\overline{p}$ (c), π^+K^- (d), $\pi^+\pi^-$ (e), $\pi^+\overline{p}$ (f), $p\pi^-$ (g).

Bibliography

[1] C. N. Yang and R. L. Mills, *Conservation of isotopic spin and isotopic gauge invariance*, Phys. Rev. **96** (1954) 191.

[2] A. Salam and J. C. Ward, *Weak and electromagnetic interactions*, Nuovo Cim. Ser. 10 (1959) .

[3] S. L. Glashow, *Partial-symmetries of weak interactions*, Nuclear Physics **22** (1961), no. 4 579.

[4] M. Y. Han and Y. Nambu, *Three-triplet model with double* SU(3) *symmetry*, Phys. Rev. **139** (1965) B1006.

[5] S. Weinberg, *A model of leptons*, Phys. Rev. Lett. **19** (1967) 1264.

[6] P. W. Higgs, *Broken symmetries, massless particles and gauge fields*, Physics Letters **12** (1964), no. 2 132.

[7] G. Aad *et al.*, *Observation of a new particle in the search for the standard model higgs boson with the atlas detector at the lhc*, Physics Letters B **716** (2012), no. 1 1.

[8] UA2 Collaboration, P. Bagnaia *et al.*, *Evidence for z0→e+e- at the cern pp collider*, Physics Letters B **129** (1983), no. 1 130.

[9] UA1 Collaboration, G. Arnison *et al.*, *Experimental observation of lepton pairs of invariant mass around 95 gev/c2 at the cern sps collider*, Physics Letters B **126** (1983), no. 5 398.

[10] UA2 Collaboration, M. Banner *et al.*, *Observation of single isolated electrons of high transverse momentum in events with missing transverse energy at the cern pp collider*, Physics Letters B **122** (1983), no. 5 476.

[11] UA1 Collaboration, G. Arnison *et al.*, *Experimental observation of isolated large transverse energy electrons with associated missing energy at s=540 gev*, Physics Letters B **122** (1983), no. 1 103.

[12] R. Brandelik *et al.*, *Evidence for planar events in e+e- annihilation at high energies*, Physics Letters B **86** (1979), no. 2 243.

[13] D. P. Barber *et al.*, *Discovery of three-jet events and a test of quantum chromodynamics at petra*, Phys. Rev. Lett. **43** (1979) 830.

[14] CDF Collaboration, F. Abe *et al.*, *Observation of top quark production in $\overline{p}p$ collisions with the collider detector at fermilab*, Phys. Rev. Lett. **74** (1995) 2626.

[15] D0 Collaboration, S. Abachi *et al.*, *Observation of the top quark*, Phys. Rev. Lett. **74** (1995) 2632.

[16] S. W. Herb *et al.*, *Observation of a dimuon resonance at 9.5 gev in 400-gev proton-nucleus collisions*, Phys. Rev. Lett. **39** (1977) 252.

[17] J.-E. Augustin *et al.*, *Discovery of a narrow resonance in e^+e^- annihilation*, Phys. Rev. Lett. **33** (1974) 1406.

[18] J. H. Christenson, J. W. Cronin, V. L. Fitch, and R. Turlay, *Evidence for the 2π decay of the k_2^0 meson*, Phys. Rev. Lett. **13** (1964) 138.

[19] A. D. Sakharov, *Violation of cp invariance, c asymmetry, and baryon asymmetry of the universe*, Soviet Physics Uspekhi **34** (1991) 392.

[20] N. Cabibbo, *Unitary symmetry and leptonic decays*, Phys. Rev. Lett. **10** (1963) 531.

[21] Particle Data Group, P. A. Zyla *et al.*, *Review of Particle Physics*, Progress of Theoretical and Experimental Physics **2020** (2020) , 083C01.

[22] S. Descotes-Genon, D. Ghosh, J. Matias, and M. Ramon, *Exploring new physics in the c 7-c 7' plane*, Journal of High Energy Physics **2011** (2011) .

[23] K. G. Wilson, *Non-lagrangian models of current algebra*, Phys. Rev. **179** (1969) 1499.

[24] J. M. Henn and J. C. Plefka, in *Tree-Level Techniques*, pp. 35–80, Springer Berlin Heidelberg, Berlin, Heidelberg, 2014. doi: 10.1007/978-3-642-54022-6_2.

[25] A. Ali and V. M. Braun, *Estimates of the weak annihilation contributions to the decays $b \to \rho + \gamma$ and $b \to \omega + \gamma$*, Physics Letters B **359** (1995) 223–235.

[26] A. Khodjamirian, G. Stoll, and D. Wyler, *Calculation of long-distance effects in exclusive weak radiative decays of b-mesons*, Physics Letters B **358** (1995) 129–138.

[27] V. Crede and W. Roberts, *Progress towards understanding baryon resonances*, Reports on Progress in Physics **76** (2013) 076301.

[28] LHCb Collaboration, R. Aaij *et al.*, *Observation of $j/\psi p$ resonances consistent with pentaquark states in $\Lambda_b^0 \to j/\psi K^- p$ decays*, Phys. Rev. Lett. **115** (2015) 072001.

[29] A. V. Sarantsev *et al.*, *Hyperon ii: Properties of excited hyperons*, The European Physical Journal A **55** (2019) .

[30] M. Matveev *et al.*, *Hyperon i: Partial-wave amplitudes for k-p scattering*, The European Physical Journal A **55** (2019) .

[31] L. Evans and P. Bryant, *LHC machine*, Journal of Instrumentation **3** (2008) S08001.

[32] ATLAS Collaboration, G. Aad *et al.*, *The ATLAS experiment at the CERN large hadron collider*, Journal of Instrumentation **3** (2008) S08003.

[33] CMS Collaboration, S. Chatrchyan *et al.*, *The CMS experiment at the CERN LHC*, Journal of Instrumentation **3** (2008) S08004.

[34] LHCb Collaboration, A. A. Alves *et al.*, *The LHCb detector at the LHC*, Journal of Instrumentation **3** (2008) S08005.

[35] ALICE Collaboration, K. Aamodt *et al.*, *The ALICE experiment at the CERN LHC*, Journal of Instrumentation **3** (2008) S08002.

[36] LHCb Collaboration, R. Aaij *et al.*, *LHCb Detector Performance*, Int. J. Mod. Phys. A **30** (2015), no. 07 1530022, `arXiv:1412.6352`.

[37] R. Aaij *et al.*, *Performance of the lhcb vertex locator*, Journal of Instrumentation **9** (2014) P09007–P09007.

[38] J. Gassner, M. Needham, and O. Steinkamp, *Layout and Expected Performance of the LHCb TT Station*, Tech. Rep. LHCb-2003-140, CERN, Geneva, Apr, 2004.

[39] LHCb Collaboration, S. Amato *et al.*, *LHCb magnet: Technical Design Report*, Technical design report. LHCb, CERN, Geneva, 2000.

[40] LHCb Collaboration, P. R. Barbosa-Marinho *et al.*, *LHCb outer tracker: Technical Design Report*, Technical design report. LHCb, CERN, Geneva, 2001.

[41] LHCb Collaboration, P. R. Barbosa-Marinho *et al.*, *LHCb inner tracker: Technical Design Report*, Technical design report. LHCb, CERN, Geneva, 2002. revised version number 1 submitted on 2002-11-13 14:14:34.

[42] L. Miguel Garcia, L. Henry, B. Kishor, and A. Oyanguren, *Tracking performance for long-lived particles at lhcb*, Journal of Physics: Conference Series **1525** (2020) 012095.

[43] LHCb Collaboration, S. Amato *et al.*, *LHCb RICH: Technical Design Report*, Technical design report. LHCb, CERN, Geneva, 2000.

[44] P. A. Cherenkov, *Visible luminescence of pure liquids under the influence of γ-radiation*, Dokl. Akad. Nauk SSSR **2** (1934), no. 8 451.

[45] LHCb Collaboration, S. Amato *et al.*, *LHCb calorimeters: Technical Design Report*, Technical design report. LHCb, CERN, Geneva, 2000.

[46] LHCb Collaboration, P. R. Barbosa-Marinho *et al.*, *LHCb muon system: Technical Design Report*, Technical design report. LHCb, CERN, Geneva, 2001.

[47] LHCb Collaboration, R. Quagliani, *Novel real-time alignment and calibration of LHCb detector for run II and tracking for the upgrade.*, Journal of Physics: Conference Series **762** (2016) 012046.

[48] T. Likhomanenko *et al.*, *Lhcb topological trigger reoptimization*, Journal of Physics: Conference Series **664** (2015) .

[49] V. V. Gligorov and M. Williams, *Efficient, reliable and fast high-level triggering using a bonsai boosted decision tree*, Journal of Instrumentation **8** (2013) P02013–P02013.

[50] C. Marin Benito, *Pushing the boundaries of the LHCb rare decays program: search for the $\Lambda_b \to \Lambda\gamma$ decay*, PhD thesis, University of Barcelona, Jan, 2018, CERN-THESIS-2018-401.

[51] R. Aaij *et al.*, *Allen: A high level trigger on GPUs for LHCb*, Comput. Softw. Big Sci. **4** (2020), no. 1 7, arXiv:1912.09161.

[52] S. Benson, V. Gligorov, M. A. Vesterinen, and J. M. Williams, *The LHCb turbo stream*, Journal of Physics: Conference Series **664** (2015) 082004.

[53] A. Alfonso Albero *et al.*, *Upgrade trigger selection studies*, tech. rep., CERN, Geneva, Sep, 2019.

[54] LHCb Collaboration, R. Aaij *et al.*, *First observation of the radiative decay $\Lambda_b^0 \to \Lambda\gamma$*, Phys. Rev. Lett. **123** (2019) 031801.

[55] I. Belyaev *et al.*, *Handling of the generation of primary events in Gauss, the LHCb simulation framework*, J. Phys. Conf. Ser. **331** (2011) 032047.

[56] D. J. Lange, *The EvtGen particle decay simulation package*, Nucl. Instrum. Meth. **A462** (2001) 152.

[57] D. Muller and B. G. Siddi, *Fast simulation options in LHCb from ReDecay to fully parametrised*, https://cds.cern.ch/record/2254334, Feb, 2017.

[58] LHCb collaboration, R. Aaij *et al.*, *Evidence for exotic hadron contributions to $\Lambda_b^0 \to J/\psi p\pi^-$ decays*, Phys. Rev. Lett. **117** (2016) 082003, arXiv:1606.06999.

[59] M. Pivk and F. R. Le Diberder, *sPlot: A statistical tool to unfold data distributions*, Nucl. Instrum. Meth. **A555** (2005) 356, arXiv:physics/0402083.

[60] T. Skwarnicki, *A study of the radiative cascade transitions between the Upsilon-prime and Upsilon resonances*, PhD thesis, Institute of Nuclear Physics, Krakow, 1986, DESY-F31-86-02.

[61] S. Tolk, J. Albrecht, F. Dettori, and A. Pellegrino, *Data driven trigger efficiency determination at LHCb*, tech. rep., CERN, Geneva, May, 2014.

[62] A. Hoecker *et al.*, *Tmva - toolkit for multivariate data analysis*, .

[63] R. H. Dalitz, *Cxii. on the analysis of τ-meson data and the nature of the τ-meson*, The London, Edinburgh, and Dublin Philosophical Magazine and Journal of Science **44** (1953), no. 357 1068, arXiv:https://doi.org/10.1080/14786441008520365.

[64] L. Anderlini *et al.*, *The PIDCalib package*, Tech. Rep. LHCb-PUB-2016-021. CERN-LHCb-PUB-2016-021, CERN, Geneva, Jul, 2016.

[65] Urania, https://gitlab.cern.ch/lhcb/Urania.